

STATE OF THE CLIMATE IN 2011

Special Supplement to the
Bulletin of the American Meteorological Society
Vol. 93, No. 7, July 2012



STATE OF THE CLIMATE IN 2011

Editors

Jessica Blunden

Derek S. Arndt

Associate Editors

Howard J. Diamond

Martin O. Jeffries

Ted A. Scambos

A. Johannes Dolman

Michele L. Newlin

Wassila M. Thiaw

Ryan L. Fogt

James A. Renwick

Peter W. Thorne

Margarita C. Gregg

Jacqueline A. Richter-Menge

Scott J. Weaver

Bradley D. Hall

Ahira Sánchez-Lugo

Kate M. Willett

AMERICAN METEOROLOGICAL SOCIETY

2. GLOBAL CLIMATE—K. M. Willett, A. J. Dolman, B. D. Hall, and P. W. Thorne, Eds.

a. Overview—P. W. Thorne, K. M. Willett, A. J. Dolman, and B. D. Hall

The year 2011 was dominated by La Niña and by divergent Arctic Oscillation conditions at year start (negative) and year end (positive). The La Niña that developed in mid-2010 and lasted through boreal spring 2011 was one of the strongest La Niña events in the historical instrumental record and is looking very much like a protracted La Niña episode (with typical boreal spring to fall neutral conditions) that has continued into early 2012. Typical signatures of La Niña, such as enhanced rainfall over Australia and reduced temperatures over much of the eastern Pacific, are the dominant geographical features in Plate 2.1 for the majority of climate variables considered. The divergent behavior of the Arctic Oscillation had significant impacts on boreal winter season climate at the beginning and end of the year over Northern Hemisphere mid-to-high latitude regions.

La Niña events typically lead to a reduction in near-surface and tropospheric temperatures globally, and 2011 was no exception. It was, however, still above the 1981–2010 average being between 9th and 12th warmest at the surface (since the late 19th century) and between 8th and 12th warmest in the troposphere (since 1958 for radiosonde and 1979 for satellite datasets). This followed near-record warmth in 2010 associated with the moderate El Niño present at the start of 2010, which rapidly decayed to La Niña conditions.

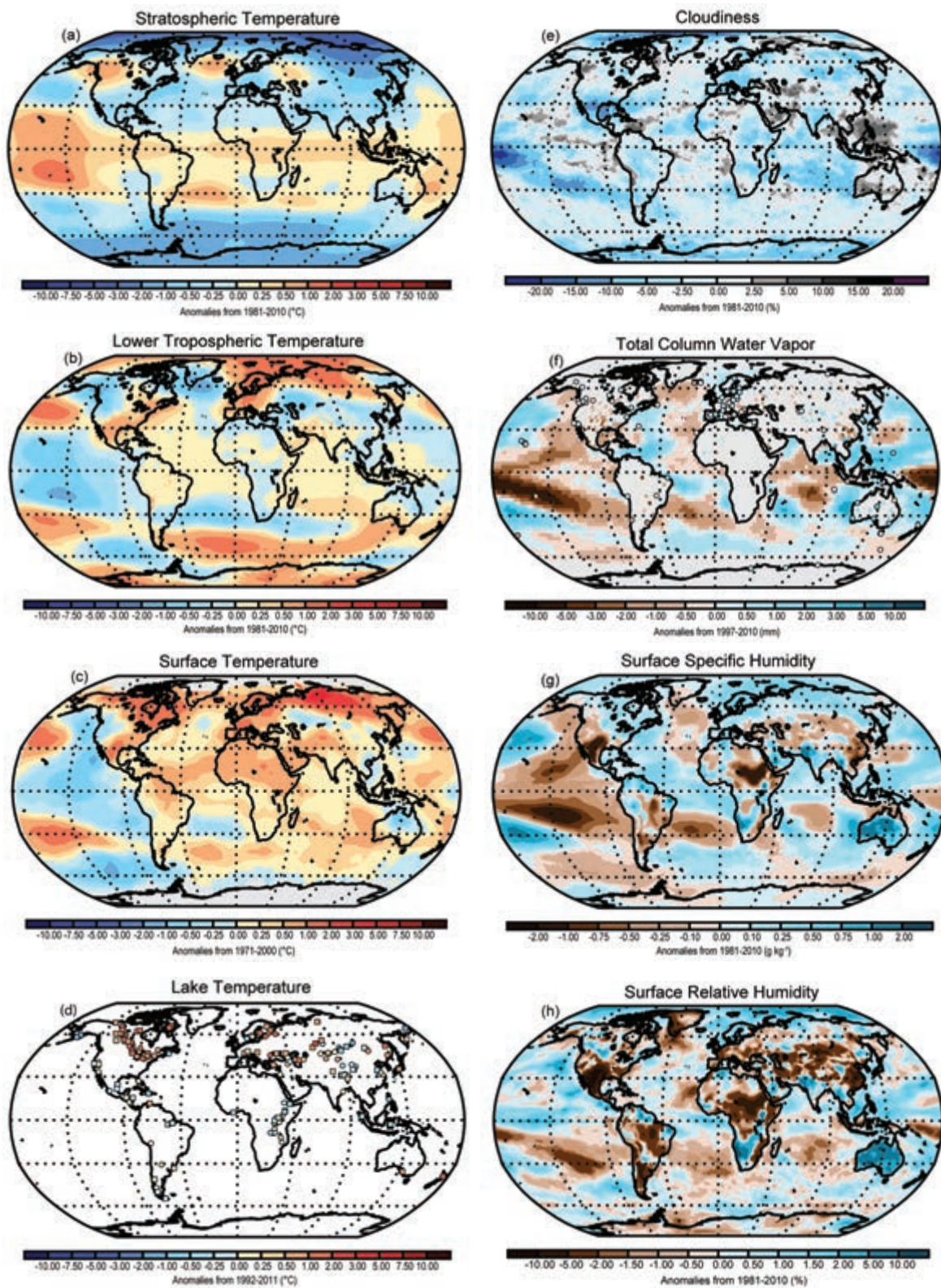
During 2011, the hydrological cycle exhibited substantial global variability. The Southern Hemisphere positive anomalies in precipitation led to significant anomalies in soil moisture and terrestrial water storage, particularly in Australia. Conversely, many Northern Hemisphere subtropical locations, most notably northern Mexico, much of the southern United States, and East Africa experienced major droughts. These hydrological cycle anomaly imprints dominate many of the atmospheric and terrestrial variables considered herein.

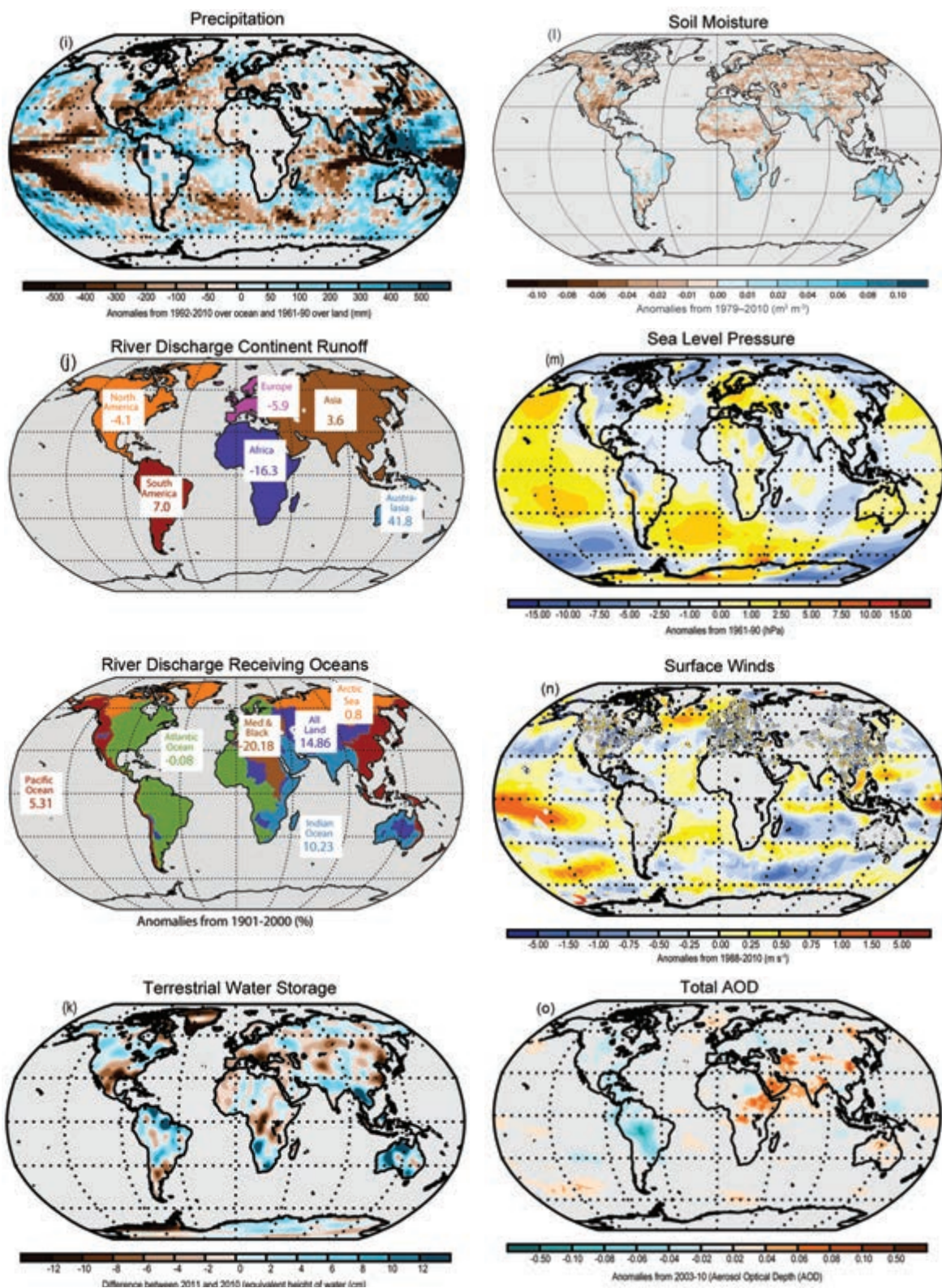
The year 2011 was especially interesting in the stratosphere. The combination of La Niña's influence on the tropical circulation and phase of the quasi-biennial oscillation were associated with a marked slowdown in the Brewer Dobson circulation. Tropical stratospheric temperatures were anomalously warm while, conversely, polar temperatures were anomalously cold. This led to large spring-time ozone reductions in polar latitudes in both hemispheres. It also had implications for transport of stratospheric water vapor.

Trace gas concentrations continued to change largely as expected, given knowledge of anthropogenic source inventories and natural sink mechanisms. Carbon dioxide concentrations exceeded 390 ppm for the first time since instrumental records began. Other greenhouse gases also continued to rise in concentration and the combined effect represented a 30% increase in radiative forcing over a 1990 baseline. Most ozone depleting substances continued to fall. Relative to peak concentrations, a fall of 33% has accrued back towards 1980 levels, when it is believed ozone depletion was not significant.

The inclusion of terrestrial indicators continues to expand and their inclusion helps to inform on the interconnectedness of the climate system. For example, despite substantially above-average rainfall over Australia, biomass burning was anomalously high over much of the country, an apparently counterintuitive finding. In fact, the rainfall anomalies promoted above-average vegetation growth, which subsequently produced above-average biomass burning during the dry season. It is only through a complete characterization of all relevant elements of the climate system that such insights can accrue. In the same vein, certain indicators cannot be updated for logistical or technological reasons in real-time, but their inclusion in delayed mode provides a valuable context.

Sidebars this year highlight: issues of data stewardship, rescue, and provenance; soil moisture; and solar transmission. Publicly available datasets used in this chapter are detailed in Appendix 2. Anomaly maps for 2011 for the majority of variables are given in Plate 2.1 and all available time series are compiled into Plate 2.2, allowing ease of comparison. In addition, an online resource contains additional figures using alternative choices of dataset at <http://dx.doi.org/10.1175/2012BAMSStateoftheClimate.3>.





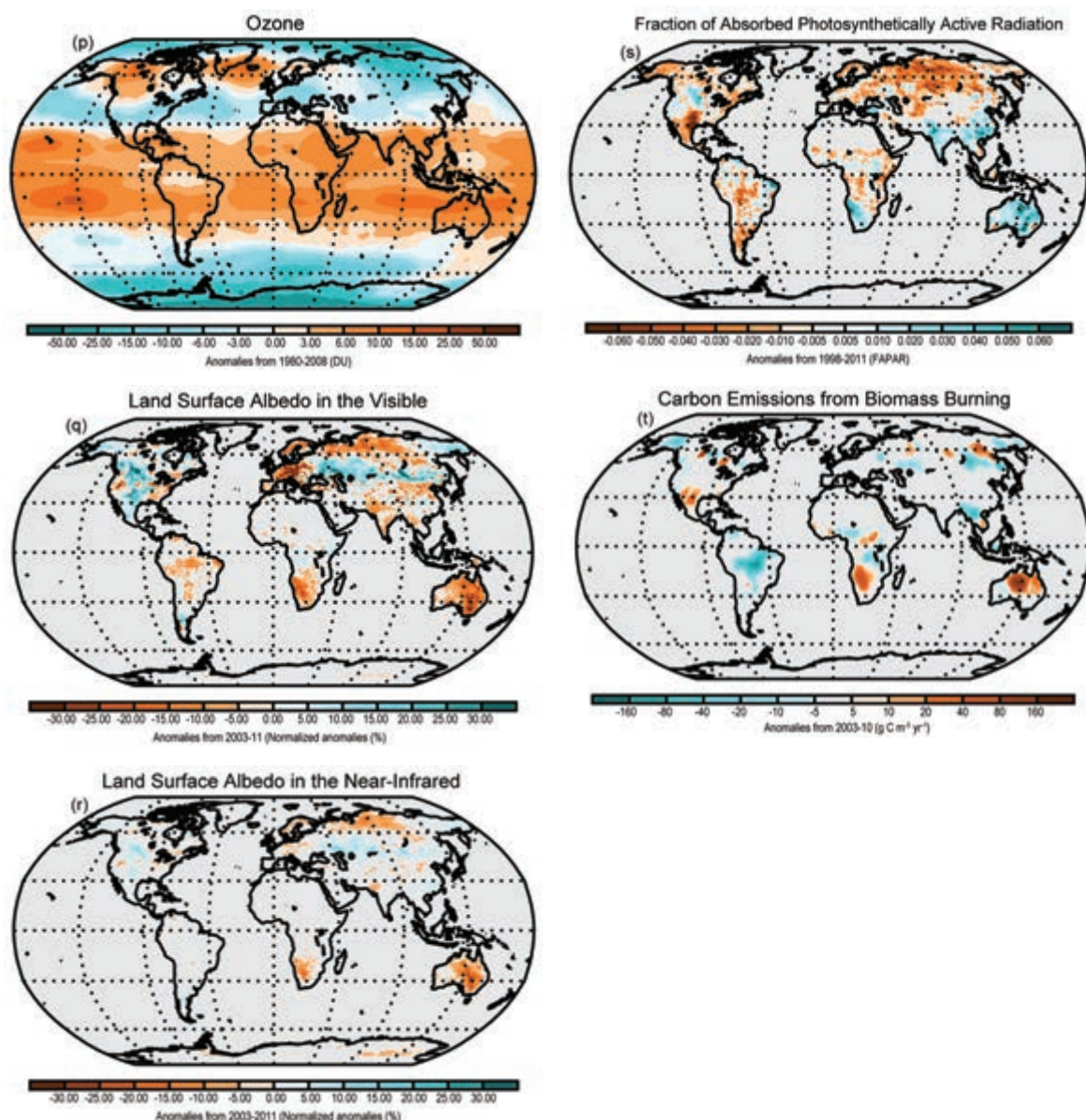


PLATE 2.1. (a) ERA-Interim 2011 anomalies of MSU Channel 4 equivalent for the lower stratospheric temperature; (b) ERA-Interim 2011 anomalies of MSU Channel 2LT equivalent for the lower tropospheric temperature; (c) NOAA-NCDC 2011 anomalies of surface temperature; (d) ARCLAKE 2011 summer season anomalies of lake surface temperature; (e) PATMOS-x 2011 anomalies of cloudiness; (f) SSMIS (Ocean) and radiosonde and ground-based GPS (circles) (Land) 2011 anomalies map of TCWV anomalies of total column water vapour; (g) ERA-Interim 2011 anomalies of surface specific humidity; (h) ERA-Interim 2011 anomalies of surface relative humidity; (i) RSS and GHCN precipitation; (j) Water Balance Model (WBM) analysis by authors showing 2011 anomalies of river discharge over continents and into oceans; (k) GRACE satellite observations of 2011 minus 2010 annual mean terrestrial water storage (the sum of groundwater, soil water, surface water, snow, and ice, as an equivalent height of water in cm); (l) WACMOS satellite observations of 2011 anomalies of soil moisture; (m) HadSLP2r 2011 anomalies of sea level pressure; (n) Satellite radiometer (ocean) and in situ (land; 1152 sites from ISD-Lite and Tim McVicar) 2011 anomalies of surface wind speed; (o) MACC reanalysis for 2011 anomalies of total aerosol optical depth; (p) GOME/SCIAMACHY/GOME2 2011 anomalies of stratospheric ozone; (q) MODIS White Sky broadband 2011 anomalies of land surface albedo from the visible spectrum; (r) MODIS White Sky broadband 2011 anomalies of land surface albedo from the near-infrared spectrum; (s) Combined SeaWiFS (NASA) and MERIS (ESA) 2011 anomalies of fraction of absorbed photosynthetically active radiation (FAPAR); (t) MACC GFAS processed MODIS observations for 2011 anomalies of biomass burning in terms of annual carbon emission per unit area.

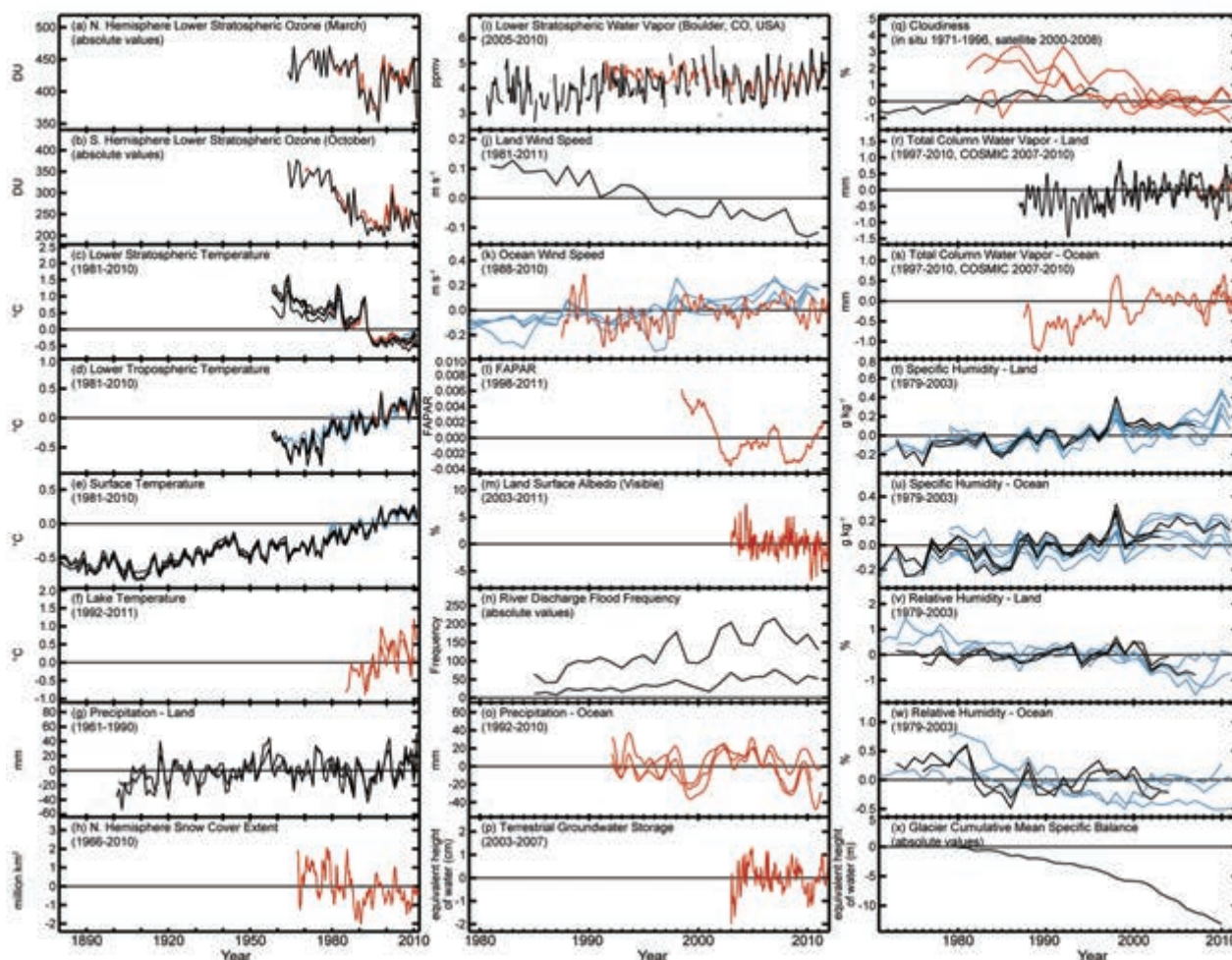


PLATE 2.2 Global (or representative) average time series for essential climate variables. Anomalies are shown relative to the base period in parentheses although original base periods may differ. Data products are colored black for in situ (IS), red for satellite (S) and blue for reanalyses (R); (a) Northern Hemisphere lower stratospheric ozone in March (IIS, 2S); (b) Southern Hemisphere lower stratospheric ozone in October (IIS, 2S); (c) Lower stratospheric temperature (4IS, 2S, 2R); (d) Lower tropospheric temperature (4IS, 2S, 4R); (e) Surface temperature (4IS, 3R); (f) Lake surface temperature (2S); (g) Precipitation over land (3IS); (h) Northern Hemisphere continental snow cover extent (IS); (i) Lower stratospheric water vapor over Boulder, Colorado (IIS, 2S); (j) Surface wind speed over land (IIS); (k) Surface wind speed over ocean (IS, 4R); (l) FAPAR (IS); (m) Land surface albedo in the visible spectrum (IS); (n) River discharge flood frequency (2IS showing two magnitudes of flood); (o) Precipitation over ocean (3S); (p) Terrestrial groundwater storage (IS); (q) Cloudiness (IIS, 5S); (r) Total column water vapor over land (2IS, IS); (s) Total column water vapor over ocean (2S); (t) Surface specific humidity over land (3IS, 5R); (u) Surface specific humidity over ocean (3IS, 5R); (v) Surface relative humidity over land (3IS, 3R); (w) Surface relative humidity over ocean (2IS, 3R); (x) Glacier cumulative mean specific balance (IIS). See relevant sections and figures for more details.

SIDEBAR 2.1: CLIMATE DATA RESCUE AND STEWARDSHIP: FILLING THE GAPS IN 21ST CENTURY NEEDS—R. ALLEN, P. BROHAN, S. LEDUC, AND K. M. WILLETT

Decisions of substantial socioeconomic importance are being made based on climate data. Ideally, this requires high spatial and temporal resolution, globally complete coverage, well-documented metadata, long temporal length, and quantified uncertainties, in addition to free access and full traceability. However, climate data are recorded by a variety of sources, sometimes without a direct interest in weather and/or climate, and do not yet meet these requirements.

The longest instrumental records are those of temperature, precipitation, and pressure. For many times and places, digitized material is available only on monthly timescales but, with concerns about the modulation of climate extremes under global warming, there is a growing need for the recovery and digitization of daily and subdaily data.

Many records remain only in paper form, scattered in repositories around the world. It is estimated that there are at least as many undigitized as there are currently digitized data (Fig. SB2.1), and that many hard copy records are rapidly deteriorating beyond recognition. A compounding issue is that in some countries historical data are seen as a potential source of revenue, and are therefore not shared openly. Thus, there are gaps in our global holdings that could, albeit with considerable effort, be filled.

The major impediments to data rescue are finance, personnel, infrastructure, and the administration to coordinate a coherent global program. Key activities center on short-term

funded regional data rescue projects. International global efforts, such as the International Environmental Data Rescue Organization (IEDRO; <http://iedro.org/>), International Atmospheric Circulation Reconstructions over the Earth Initiative (ACRE; <http://www.met-acre.org/>), and the International Surface Temperature Initiative (ISTI; <http://www.surface temperatures.org/>), have evolved from “grassroots” actions by the climate community. Such initiatives are, however, insufficiently resourced to make the needed, additional data available for research and societal applications. Recent global economic downturns have exacerbated this situation. All of this is happening among continued calls for more data in order to improve the evidence basis for climatic variability and change. Nevertheless, considerable efforts worldwide are being made to rescue, digitize, image, combine, log, and store historical weather observations for posterity, and also facilitate greater data sharing and openness. These are summarized in Fig. SB2.2 and described in more detail below.

Data rescue and digitization

Data rescue is time consuming and costly. There are archives all over the world, for example, National Meteorological Service (NMS) repositories, archives of marine and terrestrial records from colonial eras, and records held by individuals. These data need to be located, scanned, transcribed into a machine readable format, and then assimilated into appropriate, well-resourced international databases, ideally where provenance is well maintained.

ACRE is the largest current global historical terrestrial and marine weather data rescue project (Allan et al. 2011). As Fig. SB2.2 shows, the initiative has many links and collaborators around the globe. Whereas ACRE focuses on mainly pre-World War II weather data from local, regional, and international repositories from all sources, IEDRO complements ACRE by working closely with NMSs to develop their capacity to recover, image, and digitize any important surface and upper air records, especially in developing countries.

Often these records contain material of historical interest (Fig. SB2.3). ACRE has established inter/cross-disciplinary engagements between climate, social, economic, environmental, and political sciences and the humanities worldwide, i.e., Historic Weather

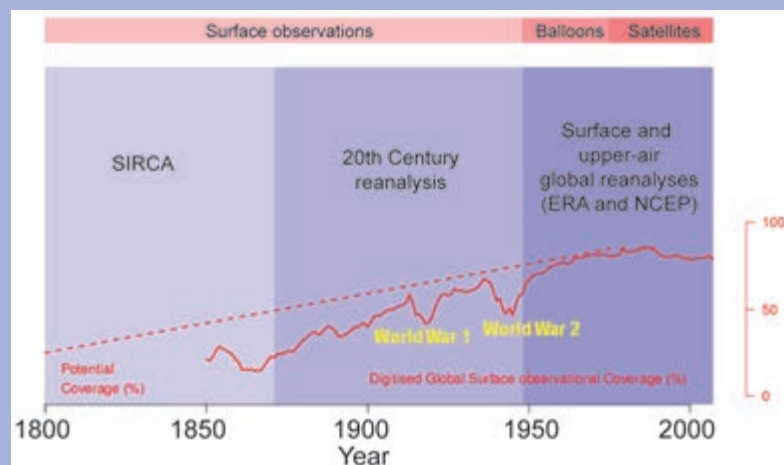


FIG. SB2.1. Digitized (solid red line) versus likely undigitized (dashed red line) data including potential available data for historical reanalyses. The blocks shaded blue through time show the range of ACRE-facilitated historical weather reanalyses in the context of contemporary international NCEP-NCAR and ECMWF reanalyses. (Source: Allan et al. 2011, Fig. 3)

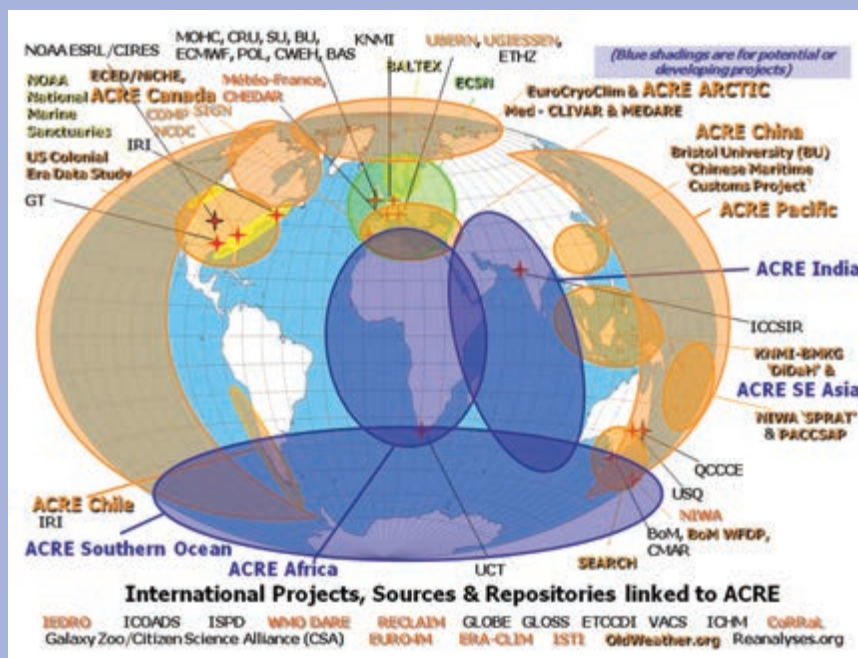


FIG. SB2.2. The full global range of collaborations, linkages, and projects involved in ACRE to date. Acronyms not defined in the text in Figs. SB2.1 and SB2.2 are defined and detailed at <http://sites.google.com/a/met-acre.org/acre/links>.

(<http://historicweather.cerch.kcl.ac.uk/node/12>) and Shipping Archives and Integrated Logbooks of Ships (SAILS) (<http://sailsproject.cerch.kcl.ac.uk/>). The combination of human interest and scientific value in the historical records has led to the successful oldWeather project (<http://oldweather.org/>), where thousands of volunteers transcribe weather and historical information in records from the UK and US national archives.

Data repositories

There are many online databanks. Often, they are regional in scope [e.g., European Climate Assessment and Dataset (ECAandD) or the Southeast Asian Climate Assessment and

Dataset (SACAandD)] or for specific variables [e.g., the International Surface Pressure Databank (ISPD)]. Most were developed and are maintained by a small number of people with limited resources. It is vital to transition such arrangements to guaranteed long-term funding through international partnerships with stable finances. Few databanks contain full traceability to data origin or measurement standards, and metadata are very sparse. To attempt true comprehensiveness and data provenance, these repositories need a framework of international effort and cooperation, combining expertise beyond climate science such as metrologists, statisticians, and software engineers. ISTI is attempting just that. It aims to be a resource for the creation of multiple climate data products by providing an open comprehensive databank with traceability and a data portal with visualization

tools for derived products (Thorne et al. 2011).

Data sharing

Having open access to all climate data is a major objective. Until worldwide data sharing becomes a reality, various international efforts from the scientific data community will continue to champion this cause. Such efforts include databanks as mentioned above, specified networks such as the Global Climate Observing System (GCOS) Surface Network (<http://gosc.org/gcos/GSN-program-overview.htm>) or international collaboration projects such as CLIMDEX (<http://www.climdex.org>). The value of truly open global climate data cannot be overstated.

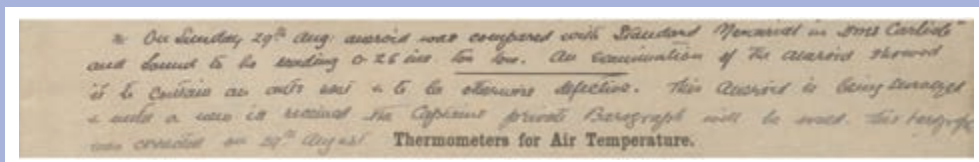


FIG. SB2.3. Human interest in a historical weather record: “On Sunday 29th Aug: aneroid was compared with standard mercurial in HMS Carlisle and found to be reading 0.26 ins. too low. An examination of the aneroid showed it to contain an ants nest and to be otherwise defective. This aneroid is being surveyed and until a new [one] is received the Captain’s private barograph will be used. This barograph was corrected on 29th August” – from the logbook of HMS Tarantula (in 1920), via <http://oldweather.org>.

b. Temperature

1) SURFACE TEMPERATURE—A. Sánchez-Lugo, J. J. Kennedy, and P. Berrisford

La Niña conditions in the tropical Pacific Ocean during much of 2011 contributed to an overall cooler year than 2010 (Fig. 2.1, see online supplemental Figs. S2.1 and S2.2 for comparison), which ranked as either warmest or second warmest year on record, according to four independent analyses with periods of records extending back to the mid-to-late 1800s [NASA-GISS, Hansen et al. 2010; HadCRUT3, Brohan et al. 2006; NOAA-NCDC, Smith et al. 2008; and, for the first time in this section, Japan Meteorological Agency (JMA), Ishihara 2006]. Nevertheless, the global surface temperature in 2011 was above the 1981–2010 base period average (Fig. 2.2a). Compared with other years in which La Niña was present (section 2e1, Fig. 2.31), 2011 was unusually warm, only matched by 2001 which featured a relatively weak La Niña episode.

2011—the coolest year since 2008—was among the top 15 years on record, ranking from 9th to 12th warmest since records began. The year was 0.09°C above the 1981–2010 average annual value in HadCRUT3, 0.11°C in the NOAA-NCDC analysis, 0.16°C in the NASA-GISS analysis, and 0.07°C in the JMA analysis. Each agency analyzes air temperatures over land and sea surface temperatures (SSTs) observed from ships and buoys separately and then merges the land and SST datasets to form a global analysis. While their methods differ, leading to minor differences in anomalies, all four analyses are in close agreement (Fig. 2.2a). The datasets show global temperatures rising gradually at a rate of between 0.71°C and 0.77°C

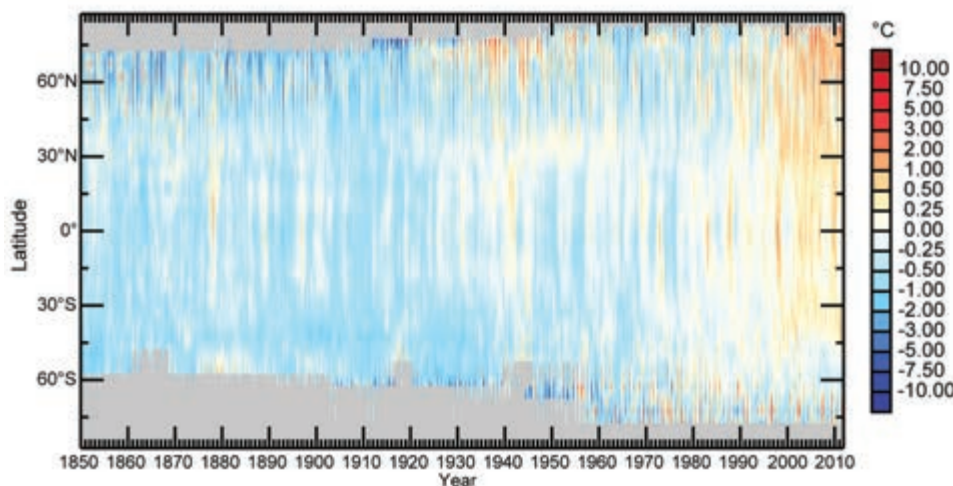


FIG. 2.1. HadCRUT3 monthly mean anomalies (°C, 1971–2000 base period) for surface temperature by latitude. Gray areas indicate regions where data are unavailable.

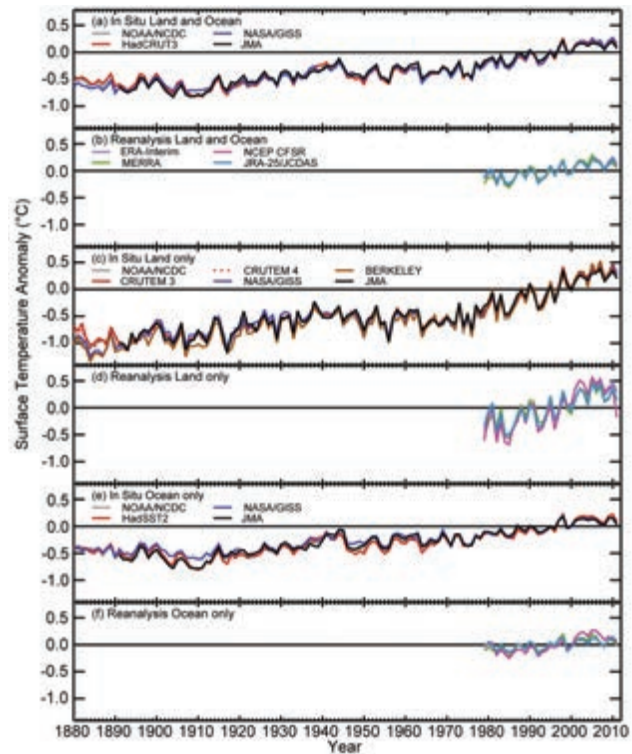


FIG. 2.2. Global average surface temperature annual anomalies (°C, 1981–2010 base period). In situ datasets for the globe: as listed in the text. In situ datasets for land only: NOAA/NCDC (see text), CRUTEM3 (see text), CRUTEM4 (Jones et al. 2012), NASA/GISS (see text), BERKELEY (Rohde et al. 2012, submitted to *J. Geophys. Res.*), and JMA (see text). In situ dataset for ocean only: NOAA/NCDC, HadSST2 (see text), NASA/GISS, and JMA. Reanalyses datasets: ERA-Interim (Dee et al. 2011a), MERRA (Rienecker et al. 2011), NCEP CFSR (Saha et al. 2010), and JRA-25/JCDAS (Onogi et al. 2007).

century⁻¹ since 1901 and between 0.14°C and 0.17°C decade⁻¹ since 1971. According to the global 2-meter temperature in the ERA-Interim reanalysis, 2011 was the ninth warmest year since records began in 1979, 0.13°C above the 1981–2010 average and the upward trend for 1979–2011 (Fig. 2.2b) was 0.12°C decade⁻¹.

Similar to the combined global land and

ocean surface temperatures, the global land-only surface temperatures and global SSTs, analyzed separately, also show increasing trends (Fig. 2.2c–f). The global average land surface temperature increased at a rate of between 0.09°C and 0.10°C decade⁻¹ since 1901 and between 0.23°C and 0.28°C decade⁻¹ since 1971, while the global average SST increased at a rate of between 0.06°C and 0.07°C decade⁻¹ since 1901 and between 0.10°C and 0.13°C decade⁻¹ since 1971.

Despite two La Niña episodes (the first strong and the second weaker), global-average SSTs remained above-average throughout the year (Figs. 2.2e–f), ranking as either 11th or 12th warmest on record. The global SST in 2011 was 0.02°C above the 1981–2010 average in the NASA-GISS analysis, 0.06°C in the NOAA-NCDC analysis, 0.09°C in the HadSST2 (Rayner et al. 2006), and 0.04°C in the JMA analysis. Annual-mean SSTs were above average across the Atlantic, Indian, and western Pacific Oceans, and below average across the eastern and equatorial Pacific Ocean, southern Atlantic Ocean, and some regions of the Southern Oceans (Plate 2.1c, see online supplemental Figs. S2.3, S2.4, and S2.5 for comparison; see also section 3b).

Unusually high temperatures affected most land areas during 2011, with the most prominent warmth across Russia (Plate 2.1c; see also section 7g1). Unusually low temperatures were observed across parts of Australia, the northwestern United States, and central and southeastern Asia (see also sections 7h2, 7b2, and 7g2, respectively). Averaged globally, the 2011 land surface temperature was 0.29°C above the 1981–2010 average in the NASA-GISS analysis, 0.25°C in the NOAA-NCDC analysis, and 0.20°C in the CRUTEM3 (Brohan et al. 2006) and JMA analysis, ranking from 5th to 10th warmest on record, depending on choice of dataset. In ERA-Interim the 2-m temperature over land was 0.30°C above the 1981–2010 average, making 2011 the eighth warmest year on record.

2) LOWER TROPOSPHERIC TEMPERATURE—J. R. Christy

Based on several sources of observational evidence, the temperature of the global lower tropospheric layer (MSU channel 2LT equivalent, surface to ~8 km) was approximately +0.15°C (0.05°C–0.20°C) above the 1981–2010 period average (Fig. 2.3). Global monthly

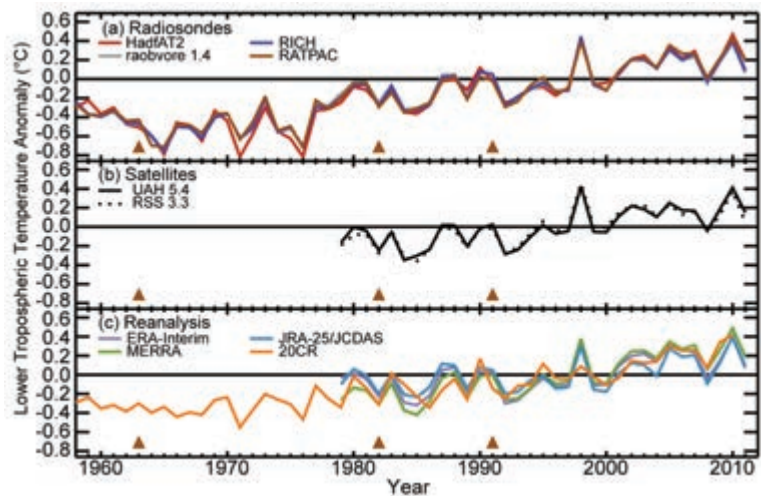


FIG. 2.3. Global average lower tropospheric temperature annual anomalies (°C; 1981–2010 base period) for the MSU channel 2LT equivalent layer. Radiosondes: HadAT2 (Thorne et al. 2005 – 465 day, 384 night stations), RATPAC (Free et al. 2005 – 85 stations), RAOBCORE (Haimberger et al. 2011, manuscript submitted to *J. Climate* – 1184 stations) and RICH (Haimberger et al. 2011, manuscript submitted to *J. Climate* – 1184 stations). Satellites: UAHv5.4 (Christy et al. 2011) and RSSv3.3 (Mears and Wentz 2009). Reanalyses: as described in Fig. 2.2 in addition to 20CR (Compo et al. 2011). Major volcanic eruptions which cause 2–3 year cooling episodes are indicated by triangles in 1963, 1982, and 1991.

tropospheric temperature anomalies reflect La Niña progression by being cooler in January–March and October–December than in the mid-year period, relative to the long-term average. Since the major global atmospheric temperature responses to these tropical ocean temperature changes are in the boreal winter, calendar-year anomalies do not capture their main impact very well. Considering the previous 33 (satellite) and 54 (radiosonde) years of records, 2011 ranked from 8th to 12th warmest, depending on the dataset examined.

New versions of some of the datasets are used. RAOBCORE and RICH radiosonde datasets have been updated. Satellite dataset RSSv3.3 has had very minor new adjustments applied to v3.2, while UAHv5.4 merely recalculated anomalies relative to 1981–2010 rather than 1979–1998 as in v5.3. HadAT and RATPAC are much the same.

Reanalysis products are also included. These assimilate all available observational data into a global forecast model that provides dynamical and thermodynamical coherency in space and time (Dee et al. 2011b). The period of record for ERA-Interim now dates back to 1979. MERRA, JRA-25/JCDAS, and 20CR are also included. Issues with incorporating new observing systems and controlling for errors are two of the factors that lead to differences among the

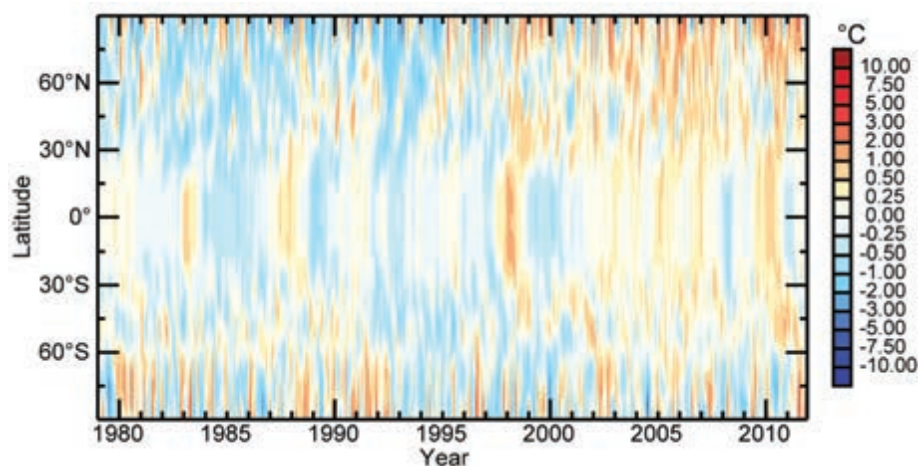


FIG. 2.4. ERA-Interim monthly mean anomalies (°C, 1981–2010 base period) of lower tropospheric temperature MSU channel 2LT equivalent by latitude.

reanalysis datasets and relative to the observation-only datasets.

The latitude cross section with time (Fig. 2.4) displays the major impacts, mainly tropical, of El Niño warming (e.g., 1998, 2010), La Niña cooling (e.g., 1989, 2011), and volcanic cooling (e.g., El Chichón in 1982, Pinatubo in 1991). Areas poleward of 30°N have experienced noticeable warming over the period.

The estimated linear trend for the entire time series (Fig. 2.3) beginning in 1958 (radiosonde era) and also beginning in 1979 (satellite era) is $+0.150 \pm 0.025$ °C decade⁻¹ where “ ± 0.025 ” represents the spread of the various datasets—an indication of error arising from different methodological choices. In terms of statistical confidence, the spread is ± 0.06 °C decade⁻¹. However, an examination of the time series indicates a somewhat stair-step evolution (not strictly linear) with what may be viewed as quasi-shifts to warmer temperatures in the late 1970s and during the large 1997/98 ENSO event. Note that the differ-

ence between the linear and stair-step approximations is not great. The spatial distribution of trends from 1979 to 2011 (Fig. 2.5) shows latitudinal symmetry between 40°N and 40°S. This broadly reflects the presence of early, strong El Niño warm events (e.g., 1983) and later La Niña cool events (e.g., 2010/11) in the cooling tropical central Pacific, with warming elsewhere.

This warming is due in part to two substantial volcanic eruptions in the first half of the 33-year record, the cooling effect of which depressed tropical tropospheric temperatures for two to three years at those times. The pattern of trends in the extratropics, however, reveal an opposing anomaly structure, with the northern regions indicating significant warming since 1979 while the southern polar areas largely experienced little warming or actual cooling.

The pattern of anomalies associated with the La Niña mode is seen in their 2011 spatial distribution (Plate 2.1b). The areas of cooler atmospheric temperatures over the Pacific Ocean, symmetric about the equator, are balanced by warmer anomalies farther poleward and eastward, then by negative anomalies poleward and eastward again. Elsewhere, in 2011, northwest North America and southern Greenland were cool while the south and east of North America was warm. In particular, the exceedingly hot and dry summer in the southern US and northern Mexico appear in the annual average. Noteworthy positive anomalies occurred from Europe to northern Asia and the North Pole, with negative anomalies in southern Asia. Somewhat similarly, in the Southern Hemisphere, positive anomalies were experienced generally around 30°S–60°S and negative anomalies toward the equator.

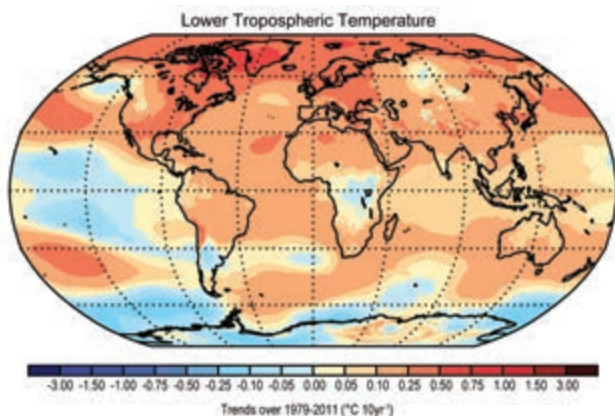


FIG. 2.5. ERA-Interim decadal trends in lower tropospheric temperature (°C 10yr⁻¹) for the MSU channel 2LT equivalent layer 1979–2011.

3) LOWER STRATOSPHERIC TEMPERATURE—C. Long and J. R. Christy

The lower stratosphere during the early months of 2011 was strongly influenced by the La Niña conditions and the phase of the quasi-biennial oscillation (QBO). The cooler tropical troposphere associated with a La Niña (section 2b2) is generally accompanied by a warmer tropical lower stratosphere. Descending

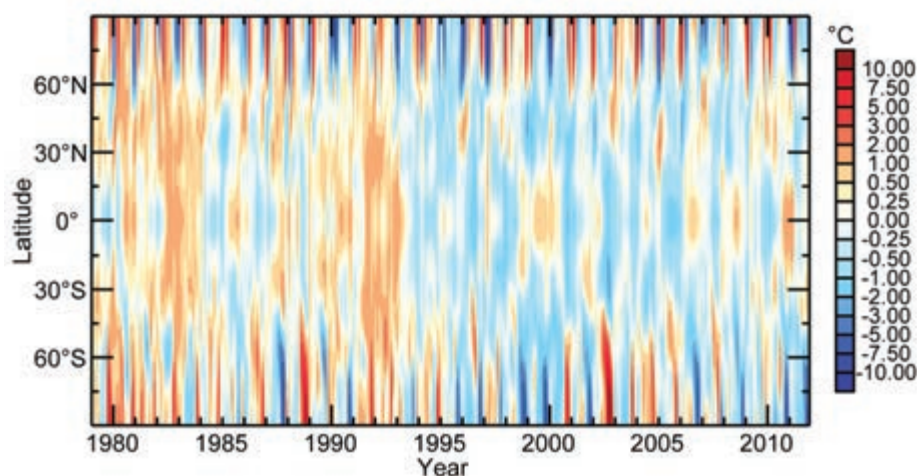


FIG. 2.6. ERA-Interim monthly mean anomalies (°C; 1981–2010 base period) of lower stratospheric temperature MSU channel 4 equivalent by latitude.

westerly winds in the tropical lower stratosphere, as in 2011, are associated with a decrease in the residual Brewer Dobson circulation, reducing transport from the tropics to the extratropics and polar latitudes (Baldwin et al. 2001). Associated with this phase of the QBO is a warmer tropical lower stratosphere and higher ozone amounts (section 2g3). In the polar regions, cooler temperatures are found with lower amounts of ozone. This pattern dominated the 2011 anomalies over the globe (Plate 2.1a), quite in contrast to 2010 (Free 2011, Plate 2.1a). Figure 2.6 shows that in the Northern Hemisphere winter months of 2010/11, cold anomalies were present in the mid-to-high latitudes, while the tropics were anomalously warm. Similarly, the Southern Hemisphere lower stratosphere polar temperatures were below normal

for most of 2011. The Northern Hemisphere winter 2010/11 was also atypical for recent years in that no midwinter warming occurred. Minimal poleward heat flux was observed during the January–February time frame, associated with colder February–March polar temperatures (see online supplemental Fig. S2.6).

The lower stratospheric global mean temperatures, as measured by the MSU channel 4 and its equivalent

channel 9 of AMSU, are shown in Fig. 2.7. They show a general downward trend from 1979 to 1996 ($-0.505^{\circ}\text{C decade}^{-1}$ and $-0.402^{\circ}\text{C decade}^{-1}$ for UAH and RSS, respectively) interrupted by the El Chichón and Mount Pinatubo volcanic eruptions. From 1996 to present, there has been very little trend ($-0.022^{\circ}\text{C decade}^{-1}$ and $-0.034^{\circ}\text{C decade}^{-1}$ for UAH and RSS, respectively). The warm tropical temperatures during December 2010–February 2011 show up in the global mean. Three of the four radiosonde datasets have a stronger cooling trend than the satellites during the period 1979–1996 ($-0.628^{\circ}\text{C decade}^{-1}$, $-0.566^{\circ}\text{C decade}^{-1}$, and $-0.714^{\circ}\text{C decade}^{-1}$ for HADAT2, RICH, and RATPAC, respectively). The exception was the RAOBCORE dataset, with a cooling trend of $-0.395^{\circ}\text{C decade}^{-1}$. In the later 2000s, the radiosonde datasets are less consistent. Their trends during 1996–2011 are $0.046^{\circ}\text{C decade}^{-1}$, $0.170^{\circ}\text{C decade}^{-1}$, $0.139^{\circ}\text{C decade}^{-1}$, and $-0.111^{\circ}\text{C decade}^{-1}$ for HADAT2, RAOBCORE, RICH, and RATPAC, respectively. The reanalyses should reproduce the lower stratospheric temperatures that the satellites observe quite well as these satellite channels are the primary source of temperature information. However, the ERA-Interim and MERRA show smaller cooling trends from 1979 to 1996 ($-0.316^{\circ}\text{C decade}^{-1}$ and $-0.397^{\circ}\text{C decade}^{-1}$) than the satellites and radiosonde datasets (see online supplemental Fig. S2.7 for trends over the globe). The two reanalyses have increasing differences in the later 2000s with the ERA-Interim showing a warming trend from 1996–present ($0.195^{\circ}\text{C decade}^{-1}$) and MERRA showing a slight cooling trend ($-0.037^{\circ}\text{C decade}^{-1}$) during this period.

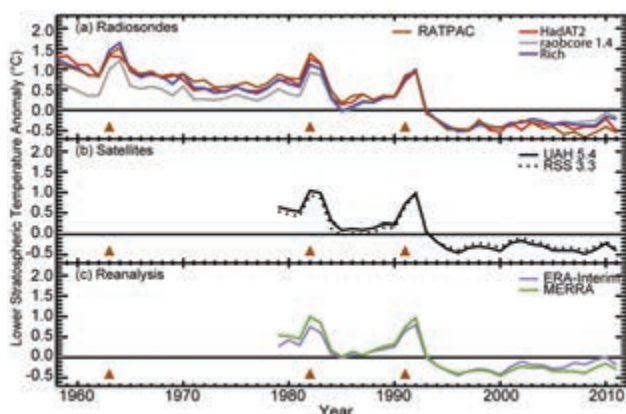


FIG. 2.7. Global average lower stratospheric temperature annual anomalies (°C; 1981–2010 base period) for the MSU channel 4 equivalent layer. Radiosondes, satellites, and reanalyses are as shown in Fig. 2.3. Major volcanic eruptions which cause 2–3 year warming episodes are indicated by triangles in 1963, 1982, and 1991.

Despite efforts to utilize the Stratospheric Sounding Unit (SSU) observations pre-1998 and then transition to AMSU-A post-1998, trend determination of the upper and mid-stratosphere is still suspect (Seidel et al. 2011). The NESDIS/STAR (L. Wang et al. 2012) evaluation of the SSU channels does offer hope that the SSU data can soon be utilized for middle and upper stratospheric monitoring. Several institutes (NESDIS, CPC, RSS) are looking into extending the SSU long-term dataset with the AMSU-A on the current POES satellites and AMSR data from NPP and JPSS satellites.

4) LAKE SURFACE TEMPERATURE—S. Hook, R. C. Wilson, S. MacCallum, and C. Merchant

In addition to the Inland Water Body Project (IWBP) satellite thermal infrared (TIR) lake product (Schneider and Hook 2010) introduced last year, the Along-track scanning radiometer Reprocessing for Climate / Lake (ARCLAKE) (MacCallum and Merchant 2012), also TIR, is included here. For the average of the 84 lakes (quasi-global) common to both datasets 2011 is cooler than 2010. There are notable differences between the two, highlighting the uncertainty due to different methodological choices.

The IWBP contains 184 lakes, with 111 lakes yielding at least 15 valid seasonal means covering 1985 to 2011. Seasonal means are constructed from summer nighttime data averaged over the warm season (see Fig. 2.8) from the Advanced Very High Resolution Radiometers (AVHRR; 1985–2009), the Along-Track Scanning Radiometers (ATSR; 1992–2011), and the Moderate Resolution Imaging Spectroradiometer (MODIS; 2010–2011) aboard the Terra satellite. For

MODIS and ATSR, skin temperatures were retrieved whereas AVHRR measurements were retrieved as bulk temperatures. To merge the datasets, the skin measurements of MODIS and ATSR were adjusted to equivalent AVHRR measurements. This maximizes data coverage and extends the satellite records, which improves trend calculation (Schneider and Hook 2010).

The ARCLAKE project covers 258 large lakes, with 164 yielding warm season average time series covering both hemispheres from 1992 to 2011 (MacCallum and Merchant 2012). It is based only on the series of three ATSRs, reprocessed with improved ARCLAKE cloud detection and physics-based surface temperature estimation. Overlaps between sensors in the series have been used to stabilize the calibration of the full time series, minimizing the potential for instrument-related artifacts in trend calculations.

Using ARCLAKE, 2011 warm season average lake temperatures were generally above average in the Northern Hemisphere, especially over Europe and northeastern North America (Plate 2.1d), agreeing with land-air and sea surface temperatures (Plate 2.1c). Cool anomalies over eastern and southeastern Asia and Alaska are also reasonably consistent. Elsewhere, the signal is more mixed and less consistent with land-air and sea temperatures, with cooling over parts of Africa and Central and South America. Global and regional average anomaly time series are presented for 84 lakes common to both datasets (Fig. 2.8). Year-to-year variability is large both within and among regions, and also between IWBP and ARCLAKE, which use different methodologies. From 2010 to 2011 IWBP shows a small warming in the

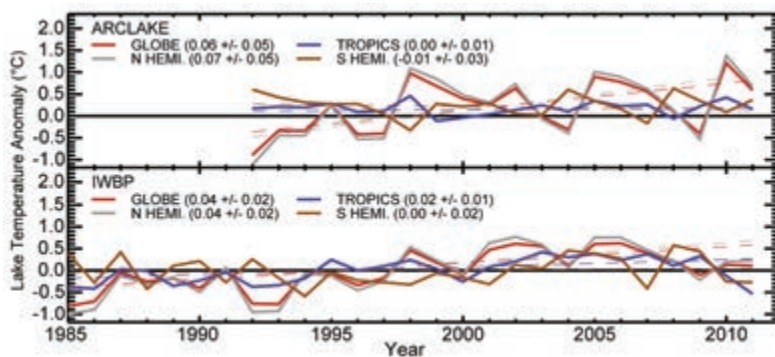


FIG. 2.8. Global and regional annual average anomalies (°C) for 84 common sites for (top) ARCLAKE (1992–2011 base period) computed from ATSR data and (bottom) IWBP (1985–2011 base period) computed from merged satellite data (AVHRR, ATSR, and MODIS). Tropical (30°S–30°N) anomalies for ARCLAKE are computed as all-year averages while IWBP tropical anomalies are computed for the dry season. The extratropical Northern and Southern Hemisphere anomalies are warm-season averages (Jul–Sep and Jan–Mar respectively).

Northern Hemisphere, cooling in the tropics, and no change in the Southern Hemisphere. ARCLAKE shows 2011 as cooler than 2010 generally, except for the Southern Hemisphere. The IWBP global mean trend is $+0.04 \pm 0.02^{\circ}\text{C yr}^{-1}$ ($p < 0.001$), likely dominated by the large number of Northern Hemispheric lakes. Weighting the three regions (northern, southern, and tropical) equally yields a global trend of $+0.02^{\circ}\text{C yr}^{-1}$. ARCLAKE trends are less certain because of the shorter time period and apparently greater interannual variability. The year-to-year variations show similar features, and all the trends are consistent within uncertainties with those

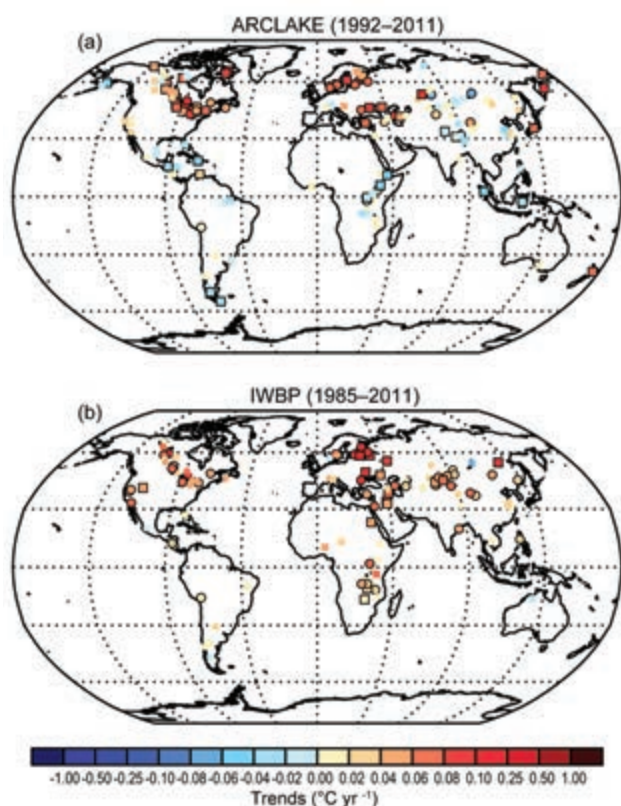


FIG. 2.9. Lake temperature trends ($^{\circ}\text{C}$) for (a) 164 lakes in ARCLAKE for 1992–2011, and (b) 111 IWBP lakes with 15 valid seasons for 1985–2011. In each plot, circles indicate lakes present in both datasets, and black borders indicate trends that are larger than the trend uncertainty.

of IWBP. Cooling from the 1991 Mount Pinatubo eruption and warming from the strong 1998 El Niño event are apparent.

The 164 lakes in the ARCLAKE dataset (Fig. 2.9a) show several spatially coherent patterns in trends (1992–2011). Trends for the African rift valley, Caribbean, and central Asian lakes are negative (0 to $-0.05^{\circ}\text{C yr}^{-1}$). In contrast, there are generally larger warming trends for lakes in North America and Europe (up to $+0.16^{\circ}\text{C yr}^{-1}$ in the case of Lake Nipigon, Canada). The 111 IWBP lakes (Fig. 2.9b) show more widespread warming, strongest in Northern Europe, where Lake Vanern, Lake Vattern, Lake Ladoga, and Lake Onega have warmed between $0.05^{\circ}\text{C yr}^{-1}$ and $0.10^{\circ}\text{C yr}^{-1}$. Trends are slightly smaller in southeastern Europe and the Middle East. Despite differing periods and methods, both ARCLAKE and IWBP are consistent in identifying relatively rapid warming in the lakes of both North America and Europe.

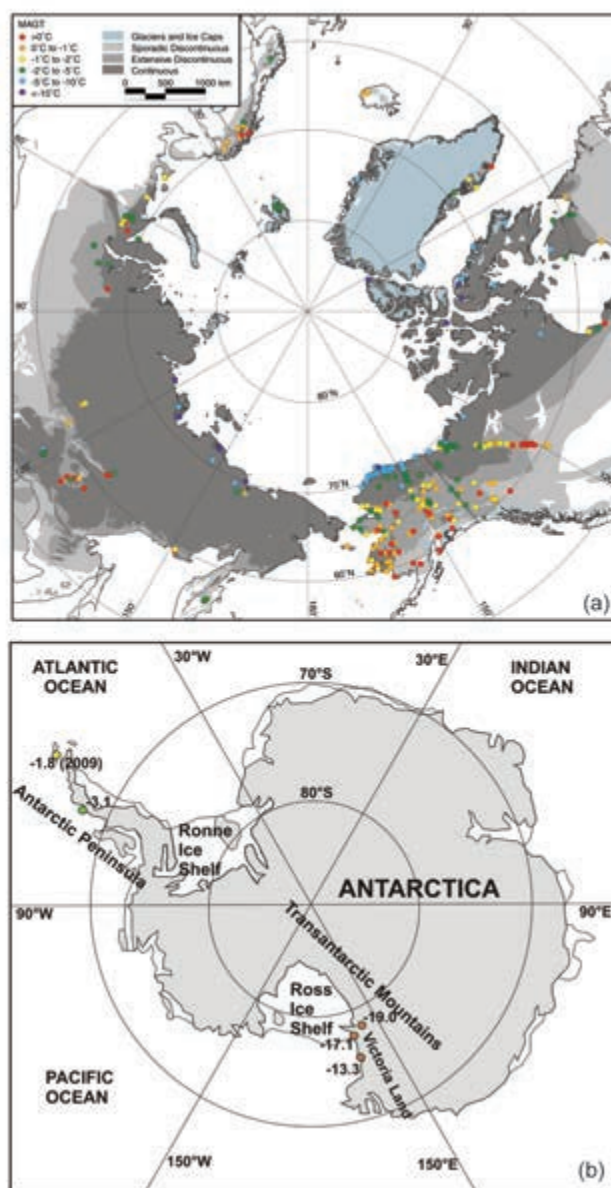


FIG. 2.10. Mean annual ground temperature (MAGT; $^{\circ}\text{C}$) for (a) the Arctic averaged over 2007–09 and (b) the Antarctic for 2010 (except King George Island, 2009). The MAGT, at the depth of zero annual amplitude, or at the nearest measurement point to it, is presented for all boreholes from which data are available. Permafrost zones after Brown et al. (1997). (Source: Romanovsky et al. 2010b)

c. Cryosphere

- 1) PERMAFROST THERMAL STATE—H. H. Christiansen, M. Guglielmin, J. Noetzli, V. Romanovsky, N. Shiklomanov, S. Smith, and L. Zhao

Permafrost temperatures are collected in the Global Terrestrial Network on Permafrost (GTN-P), and available through national databases such as the Alaskan repository at <http://www.permafrostwatch>.

org and the Norwegian repository at <http://www.ngu.no/kart/permafrost>. A Northern Hemisphere Arctic permafrost thermal snapshot (2007–09) shows significant regional differences (Fig. 2.10a). Warm ocean currents influence the climate of northern Scandinavia, Svalbard, and northwest Russia, resulting in up to 0°C permafrost temperatures in the discontinuous permafrost. In high Arctic Svalbard, the -3°C permafrost temperature is the highest in the continuous permafrost zone (Christiansen et al. 2010). In the rest of Russia and North America, permafrost temperatures vary from 0°C to -2.5°C within the discontinuous zone with colder conditions in the continuous zone; permafrost temperatures reach as low as -15°C in the high Arctic (Romanovsky et al. 2010a; Smith et al. 2010).

In Antarctica, the first ground thermal snapshot (Vieira et al. 2010) has been updated (Fig. 2.10b). In Northern Victoria Land, the active layer thickened by 1 cm year⁻¹ from 1996 to 2009 (Guglielmin and Cannone 2011), while in McMurdo Sound no clear trend was recognized from 1999 to 2007 (Adlam et al. 2010). In Northern Victoria Land, mean annual permafrost temperature increased by 0.1°C year⁻¹ between 0.3 m and 3.6 m depth despite stable air temperatures

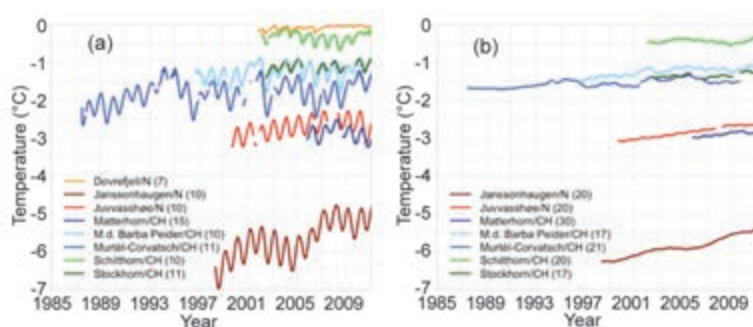


FIG. 2.11. Observed permafrost temperatures (°C) from (a) 10 m and (b) 20 m depth for selected boreholes in European mountains. Data from Swiss sites are provided by PERMOS, and for Norwegian sites by the Norwegian Meteorological Institute. (Modified from Haeberli et al. 2010, Fig. 4)

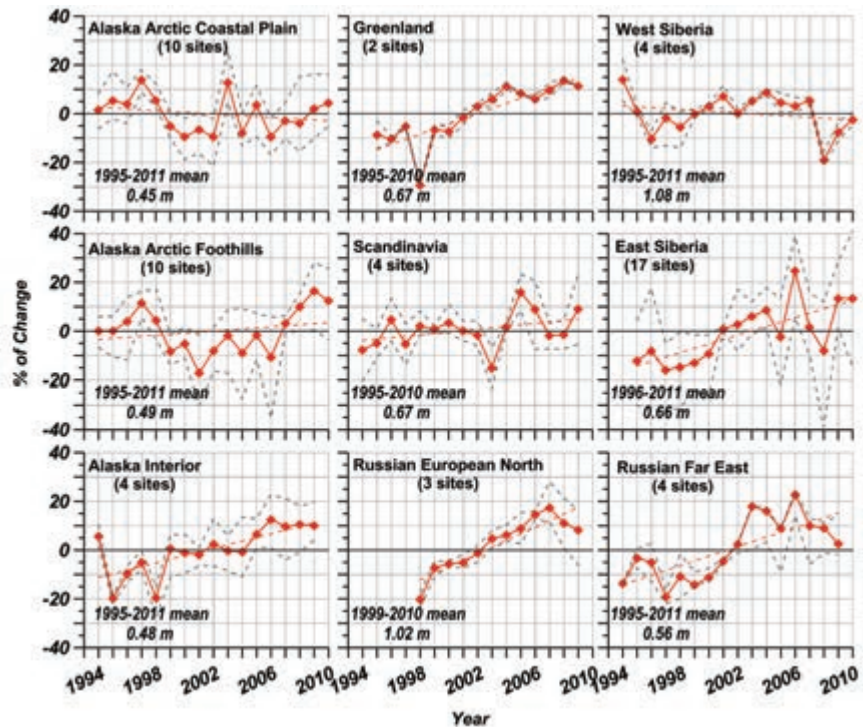


FIG. 2.12. Relative changes (anomalies from respective long-term mean values) in active layer thickness for selected Arctic Circumpolar Active Layer Monitoring (CALM) sites. Red lines represent average relative change from multiple CALM sites within the region. Dashed gray lines indicate minimum and maximum relative change. Sites with long, continuous active-layer records are used for analysis. The number of CALM sites within each region varies as indicated in parentheses.

(Guglielmin and Cannone 2011). Conversely, a reconstructed ground surface temperature history from McMurdo Sound boreholes, suggests a slight cooling from 1998 to 2003, followed by a slight warming to 2008 (Guglielmin et al. 2011).

Permafrost generally warmed across the Northern Hemisphere during the past 20 to 25 years (Romanovsky et al. 2011; Isaksen et al. 2007). Smaller warming rates are generally observed in permafrost at temperatures close to 0°C, especially if it is ice-rich, because latent heat effects dominate the ground thermal regime (see section 5g).

The permafrost in the European Alps and Scandinavian mountains is discontinuous, with mean annual ground temperature generally between 0°C and -3°C (Haeberli et al. 2010). The steep topography, heterogeneous surface characteristics, and snow cover result in high spatial variability of the ground thermal conditions. Decadal records (Fig. 2.11) for European moun-

tain permafrost show a general warming trend with smaller increases in temperature where permafrost temperatures are close to 0°C (Isaksen et al. 2007; Haeberli et al. 2010; PERMOS 2010). Permafrost temperature anomalies associated with extreme warm years (2003, 2009) are superimposed on the warming trend (PERMOS 2010; Phillips et al. 2009; Zenklusen-Mutter et al. 2010). Scandinavian trends are more pronounced (Isaksen et al. 2011). The observed trends in permafrost temperatures are consistent with changes in air temperatures, but snow cover, soil properties (including ice and moisture content), and vegetation also determine the magnitude of the changes in ground temperature (e.g., Haeberli et al. 2010; Romanovsky et al. 2010b).

In the warm permafrost of the higher altitudes of Central Asia, ground temperatures have increased by up to 0.5°C decade⁻¹ since the early 1990s, with a general increase in active layer thickness (e.g., Zhao et al. 2010).

Decadal trends in active layer thickness (ALT) vary by region (Fig. 2.12). Permafrost has disappeared in several of the Circumpolar Active Layer Monitoring

(CALM) sites. A progressive increase in ALT has been observed since the 1990s in all regions, with the exception of northern Alaska, western Canadian Arctic, and West Siberia. Smaller increases have been observed in Scandinavian sites such as Arctic Sweden and Svalbard compared to East Siberia, the Russian Far East, and Greenland. In North America, a progressive increase of ALT is observed only at sites in the Alaskan Interior, whereas ALT on the Alaskan North Slope was relatively stable over the 1995–2011 period.

2) NORTHERN HEMISPHERE CONTINENTAL SNOW COVER EXTENT—D. A. Robinson

Annual mean snow cover extent (SCE) over Northern Hemisphere (NH) lands averaged 24.7 million km² in 2011 (Fig. 2.13). This was 0.3 million km² less than the 42-year average, ranking 2011 as having the 17th least extensive cover on record (Table 2.1). This evaluation considers snow over the continents, including the Greenland ice sheet. The SCE in 2011 ranged from 48.5 million km² in January to 2.3 million km² in August. Monthly SCE is calculated at the Rutgers Global Snow Lab from daily SCE maps produced by

TABLE 2.1. Monthly and annual climatological information on Northern Hemisphere and continental snow extent between November 1966 and December 2011. Years 1968, 1969, and 1971 have 1, 5, and 3 missing months respectively, thus are not included in the annual. Ranks are from most extensive (1) to least (ranges from 42 to 46 depending on the month).

	Number of Years	Annual Mean	Std. Dev.	2011	Northern Hemisphere	Eurasia Rank	North America (inc. Greenland).
Jan	45	46.7	1.5	48.5	6	11	4
Feb	45	45.6	1.8	47.4	10	13	8
Mar	45	40.4	1.8	42.1	9	11	6
Apr	45	30.5	1.7	29.6	31	41	10
May	45	19.5	1.9	16.6	43	44	26
Jun	44	10.1	2.2	6.1	43	44	43
Jul	42	4.2	1.2	2.5	41	41	41
Aug	43	3.1	0.7	2.3	42	42	37
Sep	43	5.3	0.9	5.2	22	23	21
Oct	44	17.9	2.5	17.2	30	27	27
Nov	46	33.6	2.0	36.4	4	5	13
Dec	46	43.2	1.8	42.7	34	26	36
Ann	42	25.0	0.9	24.7	26	27	22

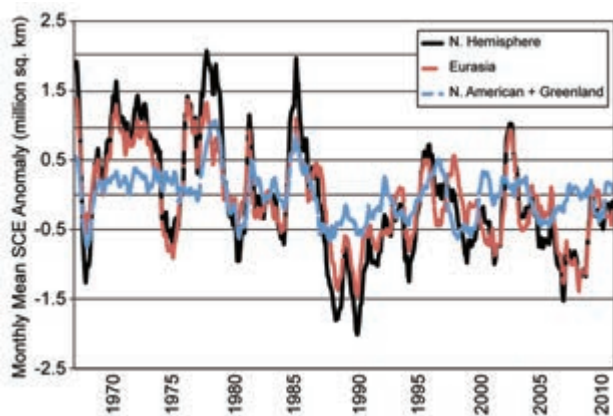


FIG. 2.13. Twelve-month running anomalies of monthly snow cover extent (million km²) over Northern Hemisphere lands (including Greenland) as a whole and Eurasia and North America separately between November 1966 and December 2011. Anomalies are calculated from NOAA snow maps. Mean hemispheric snow extent is 25.1 million km² for the full period of record. Monthly means for the period of record are used for nine missing months between 1968 and 1971 in order to create a continuous series of running means. Missing months fall between June and October, no winter months are missing.

meteorologists at the National Ice Center (a US joint NOAA, Navy, and Coast Guard facility), who rely primarily on visible satellite imagery to construct the maps. Comprehensive summaries may be viewed at the Rutgers Global Snow Lab website (<http://climate.rutgers.edu/snowcover>).

The first three months of 2011 had snow cover extents near or in the upper quartile over Eurasia (EU) and North America (NA), resulting in the sixth most extensive January SCE. Eurasian cover began a rapid retreat in April, leading to the fifth least extensive cover over this continent. Meanwhile, above-average April SCE was noted over NA, to end a very snowy season. By May, NA had caught up with EU losses, thus there was an early end to the melt season over both continents.

The 2011/12 snow season commenced in a rather average manner in September and October. Storms quickly spread snow across the NH from late October to mid-November, ranking as the fourth most extensive SCE achieved in November. The seasonal advance of snow cover slowed considerably in December, resulting in a ranking of 13th least extensive NH cover over the past 46 years.

The Arctic Oscillation (AO) was strongly negative in winter 2010/11 but strongly positive for much of late November and December 2011. This was associated with November to

April 2010/11 SCEs for the contiguous United States ranking in the top 20%, and December 2011 ranking in the lower quartile (see section 7b2 for more detail on US snow cover).

3) ALPINE GLACIERS—M. S. Pelto

The World Glacier Monitoring Service (WGMS) record of mass balance and terminus behavior (WGMS 2011) provides a global index for alpine glacier behavior. Mass balance was -766 mm in 2010, negative for the 20th consecutive year. Preliminary data for 2011 from Austria, Norway, New Zealand, and United States indicate it is highly likely that 2011 will be the 21st consecutive year of negative annual balances.

Alpine glaciers have been studied as sensitive indicators of climate for more than a century, most commonly focusing on changes in terminus position and mass balance (Oerlemans 1994). The worldwide retreat of mountain glaciers is one of the clearest signals of ongoing climate change (Haeberli et al. 2000). The retreat is a reflection of strongly negative mass balances over the last 30 years (WGMS 2011). Glacier mass balance is the difference between accumulation and ablation. The recent rapid retreat and prolonged negative balances has led to some glaciers disappearing and others fragmenting (Pelto 2010; Bhambri et al 2011; Shahgedanova et al. 2010).

The cumulative mass balance loss of the last 30 years is 13.6 m w.e. (Fig. 2.14), equivalent to cutting a 15 m thick slice off the top of the average glacier. The trend is remarkably consistent from region to region (WGMS 2011). WGMS mass balance results based on a global dataset of 30 reference glaciers with 30 years of record is not appreciably different, -13.1 m w.e. The decadal mean annual mass balance was -198 mm in the 1980s, -382 mm in the 1990s, and -740 mm for 2000–10. The declining mass balance trend during a

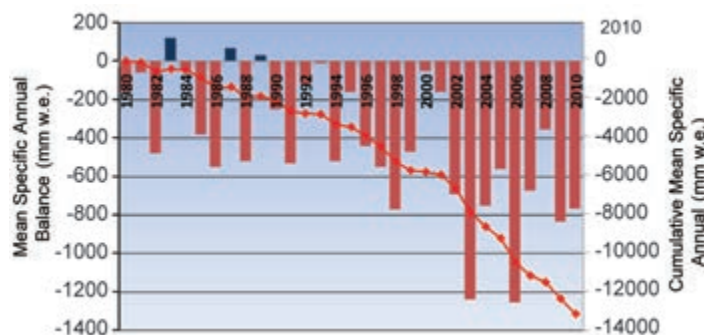


FIG. 2.14. The mean annual balance (bars, left axis) reported for all glaciers reported to the WGMS and their cumulative annual balance since 1980 (line, right axis). Units are in mm water equivalent (w.e.).

period of retreat indicates that alpine glaciers are not approaching equilibrium and retreat will continue to be the dominant terminus response.

In 2011 there was below-average winter accumulation in the Alps and significantly above-average spring and summer temperatures. This resulted in consistently strong negative balances on Austrian glaciers in 2011: Sonnblickkees, -2460 mm; Jamtalferner, -1434 mm; Kesselwandferner, -640 mm; and Hintereisferner, and -1420 mm (Fischer 2012). The Austrian Glacier Inventory examined 90 glaciers. Of these, 87 were in retreat, 3 were stationary, and average terminus change was -17 m, reflecting the continued negative mass balances of the region.

In Norway, terminus fluctuation data from 31 glaciers for 2011 indicated 27 retreating, 2 stable, and 2 advancing. The average terminus change was -17.2 m (Elverhoi 2012). The retreat rate closely matched the 2010 rates. Mass balance surveys found deficits on all Norwegian glaciers. In the North Cascades, Washington (Pelto 2011), La Niña conditions and record wet and cool conditions from March to June led to positive mass balances on all 10 glaciers examined. In southeast Alaska, 2011 snowlines were 50 m above average on Lemon Creek and Taku Glacier of the Juneau Icefield, indicative of moderate negative balances.

In New Zealand, observations on 50 glaciers found snowlines that were much higher than normal, indicating strong mass balance losses (NIWA 2011). Summer melt conditions were considerably above average.

In the high mountains of central Asia, detailed glacier mapping inventories, such as from GLIMS (Global Land Ice Measurements from Space) using ASTER, Corona, Landsat, and SPOT imagery, of thousands of glaciers indicated increased strong thinning and area loss since 2000 throughout the region except the Karakorum. In the Russian Altai, mapping of 126 glaciers indicated a 19.7% reduction in glacier area from 1952 to 2004, with a sharp increase in losses after 1997 (Shahgedanova et al. 2010). In Garhwal Himalaya, India, for 58 glaciers examined from 1990 to 2006, area loss was 6% (Bhambri et al. 2011). In the Nepal Himalaya area, loss from 1963 to 2009 was nearly 20%, (Bajracharya et al. 2011), and thickness losses increased from an average of 320 mm yr⁻¹ during 1962–2002 to 790 mm yr⁻¹ during 2002–07 in the Khumbu region, including area losses at the highest elevation on the glaciers (Bolch et al. 2011). In the Tien Shan Range, over 1700 glaciers were examined: from 1970 to 2000, glacier area decreased by 13%, and from 2000 to 2007 glacier area shrank by 4% (Narama et al.

2010). An inventory of 308 glaciers in the Nam Co Basin, Tibet, noted an increased rate of area loss for the 2001–09 period; 6% area loss (Bolch et al. 2010).

A new means of assessing global glacier volume is via GRACE (Rodell et al. 2011), which, due to its spatial resolution, is unable to resolve specific changes of individual glaciers or watersheds. In the high mountains of central Asia, GRACE imagery found mass losses of -264 mm yr⁻¹ for the 2003–09 period (Matsuo and Heki 2010). This result is in relative agreement with the other satellite image assessments, but is at odds with another more recent global assessment from GRACE that estimated Himalayan glacier losses at 10% of that found in the aforementioned examples for volume loss for the 2003–10 period (Jacob et al. 2012). At present, the detailed inventories are better validated.

d. Hydrological cycle

1) SURFACE HUMIDITY—K. M. Willett, D. Berry, and A. Simmons

There was little progress during 2011 in the development of global surface humidity products. Therefore, 2011 updates are limited to the NOCS 2.0 marine specific humidity analysis (Berry and Kent 2011) and the reanalyses. Given that ERA-Interim's (Dee et al. 2011a) earlier validation of its land surface humidity (Simmons et al. 2010) showed good behavior, this product was used to map surface humidity anomalies during 2011 (Plates 2.1g,h). ERA-Interim background 2-m humidity fields (specific and relative) were used over ocean rather than the assimilated fields due to issues of quality in the ingested humidity and temperature data from ships. Reanalysis estimates are also provided by NCEP CFSR, MERRA, and 20CR. JRA-25/JCDAS humidity fields suffered a large discontinuity due to the end of precipitable water retrieval data from microwave imagers during 2011. This is clear in the monthly means but not so apparent in the annual mean. The in situ data were quality controlled and, in the case of NOCS 2.0, bias and height corrected. Issues still remain to be resolved over the pre-1982 marine humidity data in HadCRUH (Willett et al. 2008) and Dai (Dai 2006). NOCS 2.0 provides estimates over all ice-free regions of the oceans but only those regions with high confidence were used in this assessment, predominantly the shipping lanes in the Northern Hemisphere. Confidence in the in situ data decreases post-2006 due to reducing numbers of observations and loss of call sign information in the source data (ICOADS; Woodruff et al. 2011), which removes the ability to reliably link observations to their metadata

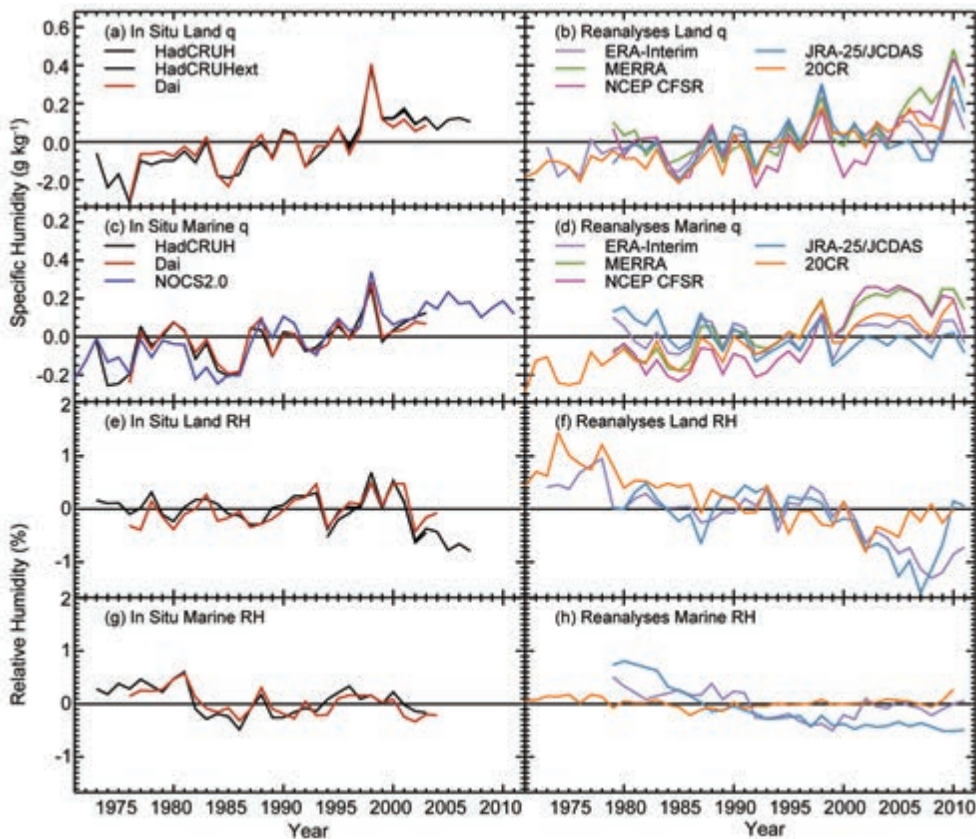


FIG. 2.15. Global average surface humidity annual anomalies (1979–2003 base period). For the in situ datasets 2 m surface humidity is used over land and ~10 m over the oceans. For the reanalyses 2 m humidity is used over the whole globe. For ERA-Interim only points over open sea are evaluated. HadCRUH and HadCRUHext use the 1974–2003 base period. Dai uses the 1976–2003 base period. All reanalyses products use the 1981–2010 base period. NOCS 2.0 used a 1979–2003 base period. All data have been adjusted to have a mean of zero over the common period 1979–2003 to allow direct comparison.

(e.g., Kent et al. 2007). HadCRUH and Dai updates are underway—the original data are included here for completeness.

In terms of absolute moisture content at the surface, following a fairly moist and very warm 2010, 2011 was drier on average although moist relative to the last 39 years. This can be seen in both the land and marine averages (Fig. 2.15) and is consistent with 2011 being cooler than 2010 (section 2b1). While limited in coverage, the in situ data tell a concurrent story of surface moistening over the oceans. Globally, MERRA and 20CR show a similar moistening over the oceans but the other reanalyses do not reproduce the observed trends. The uncertainties in the marine datasets, both in situ and reanalyses, are likely to be as large as the trends themselves.

Over land, the relative drying of the atmosphere since 2000 (Simmons et al. 2010), in terms of relative humidity, continued to abate slightly, as in 2010. Over oceans, no such drying was observed in either

the reanalyses or in situ data and 2011 showed little change. The issues noted above for reanalyses specific humidity are likely also to affect the relative humidity and so further investigation is necessary.

The global pattern of specific humidity (Plate 2.1g) shows clear La Niña characteristics over the Pacific Ocean consistent with the continuing La Niña conditions throughout 2011. There are notable dry regions, such as the southern US and Mexico, eastern China, and east central Africa. Australia is particularly moist.

The global pattern

of relative humidity (Plate 2.1h) shows similar or reduced spatial coherence. There is agreement among different data sources on the large features mentioned

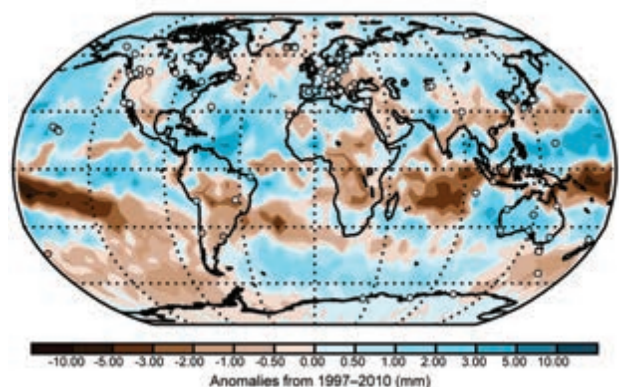


FIG. 2.16. COSMIC and ground based GPS radio occultation measurements (circles) 2011 anomalies (mm; 2007–2010 base period for COSMIC; 1997–2010 base period for GPS) of total column water vapor.

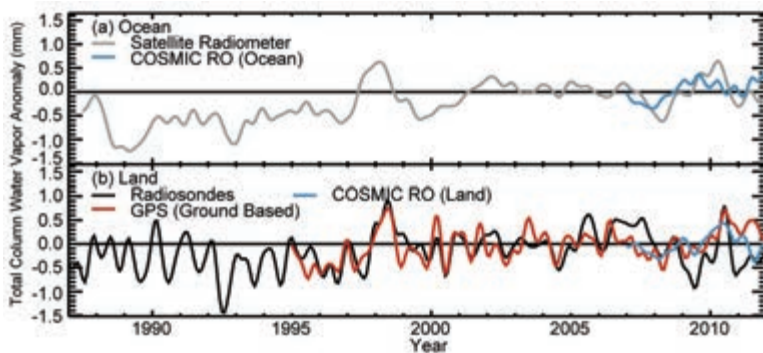


FIG. 2.17. Global average total column water vapor anomalies (mm; 1977–2010 base period, COSMIC uses 2007–10) from satellite-borne microwave radiometers (SSM/I, SSMIS, AMSR-E and WindSat) over ocean, COSMIC over land and ocean, radiosondes, and radio occultation measurements from ground based GPS over land. The time series were smoothed to remove variability on time scales shorter than six months.

above, but care should be taken in interpretation over typically data sparse regions, such as central Africa.

2) TOTAL COLUMN WATER VAPOR—C. Mears, J. Wang, S. Ho, L. Zhang, and X. Zhou

The map of total column water vapor (TCWV) anomalies for 2011 (Plate 2.1f) includes data from satellite-borne microwave radiometers, homogenized radiosonde, and ground-based GPS measurements (Wentz 1997; Wentz et al. 2007; J. Wang et al. 2007; Dai et al. 2011). In the tropical Pacific Ocean there is a C-shaped dry anomaly that is most pronounced south of the equator. This is similar to 2010 although smaller in spatial extent. In the western tropical Pacific, there is a strong wet anomaly that extends with diminished intensity to the northeast and south. Many of these features are associated with the La Niña event. Over land, radiosondes indicate dry anomalies over eastern China and southern North America.

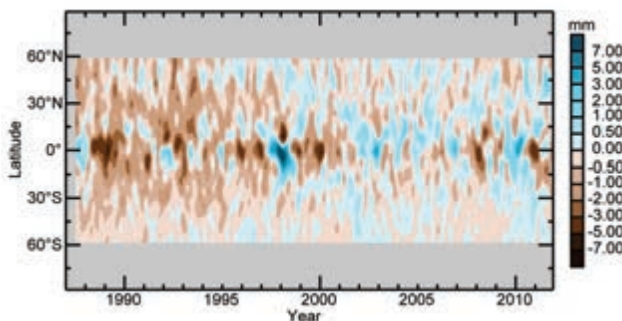


FIG. 2.18. Satellite radiometer (SSM/I, SSMIS, AMSR-E and WindSat measurements) monthly mean anomalies (mm; 1977–2010 base period) for total column water vapor (ocean only) by latitude. Data were smoothed in the time direction to remove variability on time scales shorter than four months.

Many of the same features are present in the 2011 surface specific humidity and precipitation anomalies (Plates 2.1g and 2.1i, respectively). The pattern in TCWV anomalies is confirmed by COSMIC measurements (Fig. 2.16; Ho et al. 2010), which have the advantage of extending over land regions. GPS sites generally concur with COSMIC and the radiosondes, except over central Europe. Potential biases in European GPS sites due to a change in processing in April 2011 are being investigated.

Over the ocean, the TCWV global anomaly time series (Fig. 2.17a) from the microwave radiometers shows maxima in 1987/88, 1997/98, and 2009/10, associated with El Niño events, as well as a more subtle increasing trend corresponding with increasing global temperatures. Relative minima are apparent in Northern Hemisphere winters during the La Niña events of 1988/89, 1992/93, 1999/00, 2007/08, and from late 2010 onwards. The ocean-only COSMIC data also show the strong maximum in 2009/10. This feature is apparent in the land-only COSMIC data (Fig. 2.17b) in 2010/11 but is larger in the GPS and radiosonde data. A time vs. latitude Hovmuller plot derived from the satellite radiometers (Fig. 2.18) shows that, over the

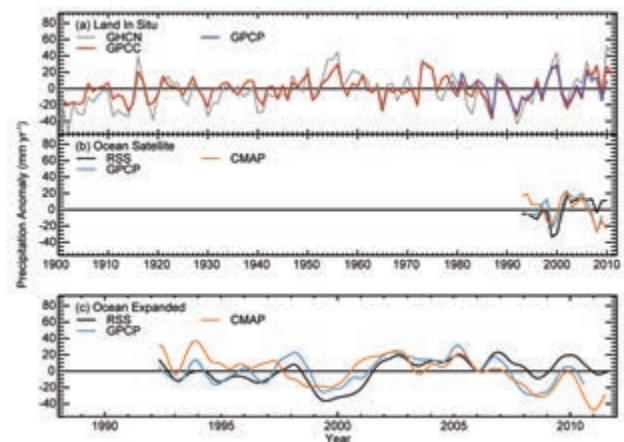


FIG. 2.19. Globally averaged precipitation anomalies (mm yr^{-1} ; 1961–90 base period over land, 1992–2011 base period over oceans) for (a) three in situ datasets over land, and (b) and (c) three satellite-based datasets over ocean. Global ocean averages cover 60°S to 60°N using a common definition of “ocean”. Panel (c) shows low-pass filtered time series by convolution with a Gaussian distribution with four-month width at half-peak power whereas panel (b) shows annual averages of this for comparison with land data.

ocean domain, the changes associated with El Niño/La Niña are largest in the tropics.

3) PRECIPITATION—D. E. Parker, K. Hilburn, P. Hennon, and A. Becker

Globally, precipitation over land remained above the 1961–90 average in 2011 in records from both the Global Historical Climatology Network Monthly Version 2 (GHCN; Peterson and Vose 1997) and the Global Precipitation Climatology Centre (GPCC) Monitoring Product (Schneider et al. 2011; Fig. 2.19a). 2011 was the 2nd wettest year in the GHCN record, behind 2010, but only the 12th wettest year in the GPCC record where 2010 was the 6th. The Global Precipitation Climatology Project Version 2.1 (GPCP; Adler et al. 2003) is not yet updated to include 2011 but is shown in Fig. 2.19a for completeness. The positive anomalies of 2011 rainfall over land from GHCN and GPCC were about 20 mm – 40 mm, slightly lower than in 2010. The GPCC record, which indicates the smaller anomaly, is based on more observing stations.

Figure 2.20, from the GHCN data, suggests that zonal average precipitation was above the 1961–90 normal around 15°S–25°S, 0°–25°N, and 35°N–50°N. The world map of land and ocean precipitation in Plate 2.1i uses GHCN precipitation over land; coverage is sparse, especially over Africa and Amazonia. Seasonal and annual precipitation anomalies from GPCC are shown in online supplemental Figs. S2.8, S2.9, and S2.10. There are some differences between the GPCC and GHCN annual anomalies, especially over Australia, likely due to both sampling and methodological differences. Note that GPCC data contain statistically infilled estimates over regions with few or no stations. Droughts are apparent in Europe and the southern US / northern Mexico region. The latter, a La Niña-related drought, likely contributed to the slightly-below-average precipitation at 25°N–35°N in Fig. 2.20. The year 2011 was the second successive wet year in Australia, contributing to the above-average

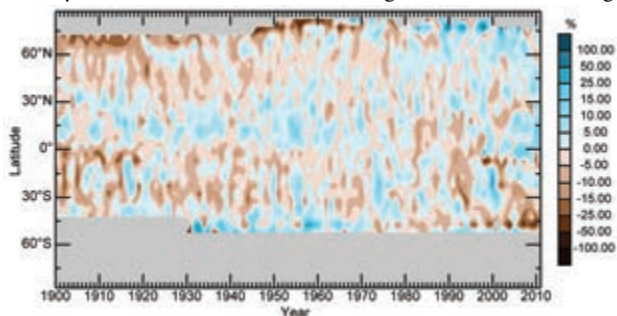


FIG. 2.20. GHCN land precipitation anomalies (% , 1961–90 base period) by latitude. Gray areas indicate regions where data are unavailable.

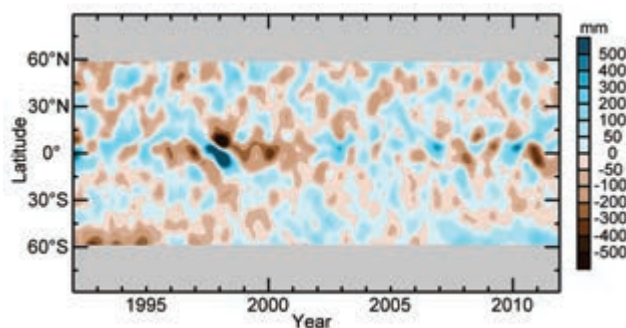


FIG. 2.21. RSS ocean precipitation anomalies (mm; 1992–2011 base period) by latitude. Gray areas indicate regions where data are unavailable.

zonal mean at 15°S–25°S in Fig. 2.20. This reflects the influence of La Niña and the warm eastern Indian Ocean, which also contributed to the strongest ever monsoon season across Thailand (see section 7g). Plentiful rains over parts of the Horn of Africa during September–November 2011 (see online supplemental Figs. S2.9 and S2.10) somewhat relieved the drought arising from the failure of the previous two rainy seasons (see Sidebar 7.2).

The global ocean precipitation climatology uses Remote Sensing Systems (RSS) Version-7 intercalibrated passive microwave rain retrievals (Hilburn and Wentz 2008). Version-7 data available at the time of writing include: F11, F13, F14, and F15 SSM/I, F17 SSMIS, AMSR-E, and WindSat. For Version-7, a change made to the beamfilling correction in the RSS rain algorithm has increased light rain rates in the extratropics, which led to an overall increase in the global mean rain rate. The 1992–2011 global average rain rates over the ocean from 60°S to 60°N are: 1113 mm yr⁻¹, 1109 mm yr⁻¹, and 1147 mm yr⁻¹ from RSS, GPCP (through 2010), and CMAP, respectively. Figure 2.19b,c shows global ocean time series for RSS, Version 2.2 GPCP through 2010 (Adler et al. 2003), and V1201 CMAP (Xie and Arkin 1997). All three datasets trended downward over 2010, but this has reversed in RSS and CMAP and they trended upward slightly in 2011. On a longer time scale, GPCP and CMAP have trended downward since 2006, while RSS has not.

A time-latitude section of precipitation over the oceans (Fig. 2.21) shows that the equatorial wet anomaly in early 2010 was replaced by a very strong dry anomaly in mid-2010, which persisted throughout 2011. The anomaly map for 2011 (Plate 2.1i) shows a La Niña pattern with an expansive and intense dry anomaly over the central Pacific. The dry anomaly extends deep into the Southern Hemisphere along the South Pacific convergence zone. In the Northern

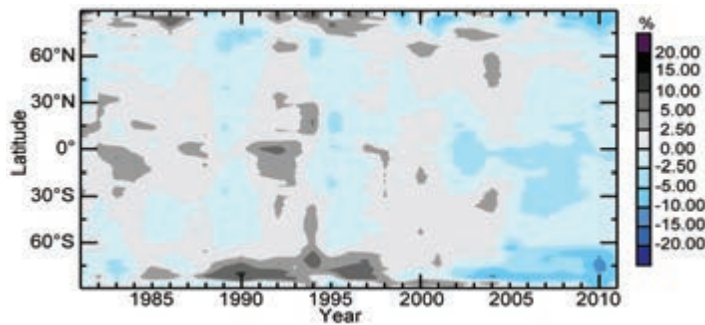


FIG. 2.22. Annual global cloudiness anomalies (%; 1981–2010 base period) from the PATMOS-x record calculated zonally for each degree latitude.

Hemisphere, the anomaly extends north across the Pacific towards Mexico. A moist anomaly is present in the far western Pacific, just east of the Philippines. Relative to 2010, the precipitation anomaly pattern for 2011 shifted to the east about 30° and greatly intensified, especially the dry anomaly in the central Pacific.

4) CLOUDINESS—M. J. Foster, S. A. Ackerman, A. K. Heidinger, and B. C. Maddux

Observed global cloudiness in 2011 reflected La Niña. Several continental anomalies corresponded to severe drought or flooding, again consistent with La Niña, coupled with positive phases of the Arctic Oscillation in the boreal spring and fall, and a pronounced Siberian High (section 2e1). The primary dataset used for this analysis, Pathfinder Atmospheres Extended (PATMOS-x), is a 30-year record of cloud retrievals taken from the Advanced Very High Resolution Radiometers (AVHRR). Global cloudiness in 2011 was 1.5% lower than the climatological annual mean relative to 1981–2010; this marks the seventh least-cloudy year on record.

The La Niña resulted in enhancement of convective cloudiness in the western equatorial Pacific and over Indonesia, with a corresponding reduction in the central equatorial and southeastern Pacific (Plate 2.1e). This was driven by SST anomaly patterns (Plate 2.1c) and positive low-level easterly wind anomalies. Large portions of the negative annual anomalies in the central equatorial and southeastern Pacific are significant at the 5% (greater than two standard deviations) level. Some of the year-to-year variability in the global cloudiness record, especially over oceans, corresponds with phases of ENSO (Fig. 2.22).

Noteworthy continental cloudiness events included positive anomalies over Australia and negative anomalies over the southern United States, eastern Africa, south-central Siberia, and much of Europe. Of these, the southern United States (extending into the Gulf of Mexico) and the south-central Siberian events experienced annual anomalies with the highest confidence of statistical significance, while areas over Europe, eastern Africa, and Australia were still significant at the 5% level. The negative annual anomalies over Europe are consistent with the positive

phases of the Arctic Oscillation in the boreal spring and fall. The negative anomalies in Siberia are consistent with a strong Siberian High.

Figure 2.23 shows global mean annual cloudiness anomalies from six data records. The surface weather observations are shown separately from the five satellite records, highlighting the difference between observing clouds from below (including observations from weather stations and ship observations by both human and automated methods) versus top-down from satellites. Surface-based observations differ in the spatial extent of the field-of-view as well as the configuration of the cloud field itself. In addition, there are fundamental differences in resolution (both spatial and temporal), units of measurement, viewing

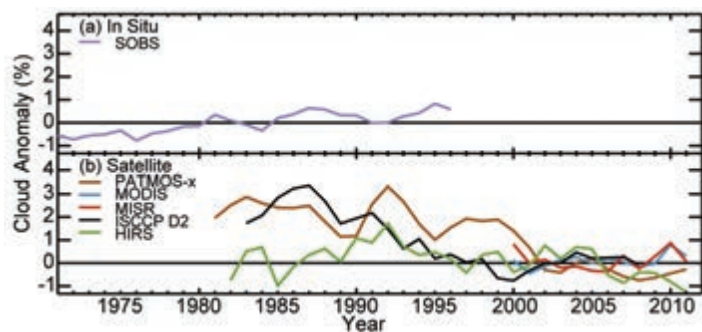


FIG. 2.23. Annual global cloudiness anomalies (%; 1971–1996 base period for in situ and 2000–08 base period for satellites). (a) Surface weather observations (SOBS; Hahn and Warren 2007), (b) Satellite observations: Moderate Resolution Imaging Spectroradiometer (MODIS; Ackerman et al. 2008) and Multiangle Imaging Spectroradiometer (MISR; Di Girolamo et al. 2010) instruments, which are located on NASA's Terra satellite and are ongoing (a MODIS instrument is also located on NASA's Aqua satellite and is included in the MODIS cloud product from 2003); International Satellite Cloud Climatology Project (ISCCP D2) data derived from the imaging radiometers on the operational weather satellites of several nations; High Resolution Infrared Sounder (HIRS; Wylie et al. 2005); and PATMOS-x AVHRR (Heidinger and Pavolonis 2009), which are instruments located on the NOAA polar-orbiting satellite series.

angle, and spectral range, among satellite and surface methods. So, while it is useful and often enlightening to track clouds both from above and below, when these measurements are condensed to single points in a time series, the conclusions that can be drawn from their direct comparison are ambiguous at best (Hughes 1984; Mokhov and Schlesinger 1994). Since 2000, the various satellite cloud records are much more stable than previously, though not in complete harmony. This difference is likely due in part to referencing to a 2000–08 average base period; also, the advent of additional satellites, with more advanced sensors and more stable orbits, allowed for development of intercalibration techniques that consequently reduced the range among cloud detection algorithms. Extreme events, such as the eruption of Mount Pinatubo and strong phases of ENSO, may also contribute to the large differences between the earlier records.

5) RIVER DISCHARGE—B. M. Fekete, R. B. Lammers, and G. R. Brakenridge

The Dartmouth Flood Observatory, operated from University of Colorado, maintains an operational system to monitor floods worldwide from satellite systems. The observatory also compiles a comprehensive database of floods reported by news media outlets since 1985. The limited consistency of this database (particularly prior to the Internet era) does not allow for straightforward assessment of trends in the frequency of flood events, but it is still informative (Fig. 2.24).

The apparent increase in both modest and major flood events from 1985 to 2007 may reflect, in part, better reporting. The year-to-year variation describes the global interannual patterns of flood events. According to this database, 2011 was not extraordinary in terms of number of flood events.

The water balance model (WBM) analysis (Fekete and MacDonald 2011; Fekete et al. 2010), with the

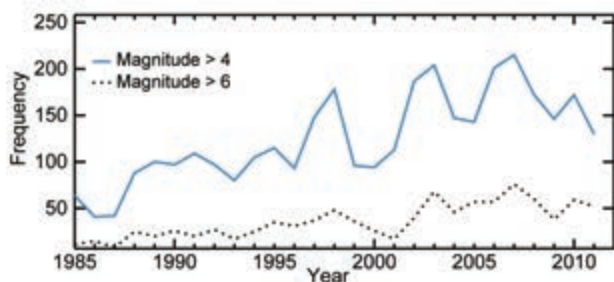


FIG. 2.24. Major floods worldwide from 1985 to 2011 according to the Dartmouth Flood Observatory database. Magnitude is defined as a product of the severity of the flood event (expressed as an index ranging between 1 and 2), the duration of the flood, and the affected area.

same configuration (Vörösmarty et al. 1998; Wisser et al. 2010a,b) as used in the 2009 and 2010 *State of the Climate* discharge assessments, shows more detail. It was driven by daily air temperature from the NCEP/NCAR reanalysis (Kalnay et al. 1996; Kistler et al. 2001) and monthly precipitation forcing from the latest version (V4.0) of the Global Precipitation Climate Center's (GPCC) monitoring product, which was downscaled to daily time steps by daily partitioning of the monthly precipitation based on the NCEP reanalysis. The runoff variations of the last three years (2009–11) are compared to the 1901–2000 average from Wisser et al. (2010a) for continents and receiving ocean basins in Fig. 2.25, and 2011 anomalies are highlighted in Plate 2.1j.

2011 was wetter than the 1901–2000 long-term mean on three continents (Asia, Australia, and South America) and remaining islands. Australia stands out with 42% more runoff than the long-term mean, which is consistent with the numerous major flood events reported during the year (see Sidebar 7.4). The high runoff in Australia can be seen in the elevated runoff discharging into the Indian and Pacific Oceans. Africa experienced continued hydrological drought although less severe than the previous two

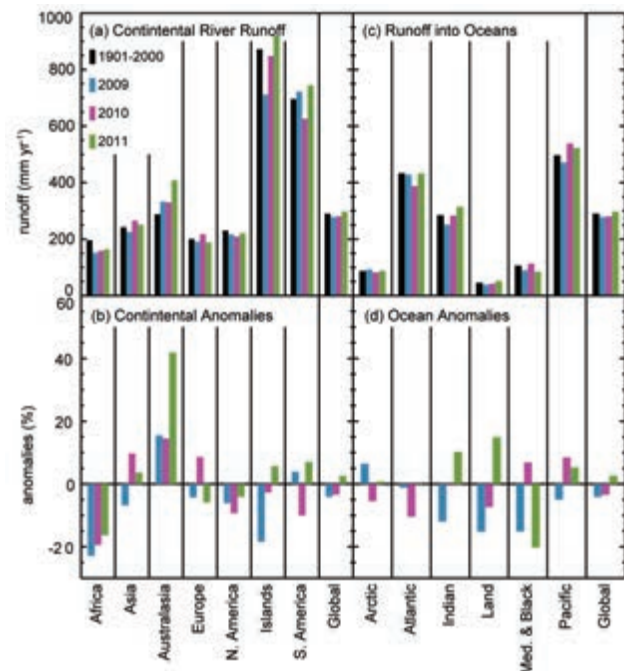


FIG. 2.25. Water balance model runoff estimates (a) and (b) over continents, and (c) and (d) by receiving oceans. (a) and (c) Long-term mean runoff (mm yr^{-1} ; for the 1901–2000 period) and annual runoff for each of the last three years (2009, 2010, 2011). (b) and (d) Annual anomalies (%; 1901–2011 base period) for 2009, 2010, and 2011.

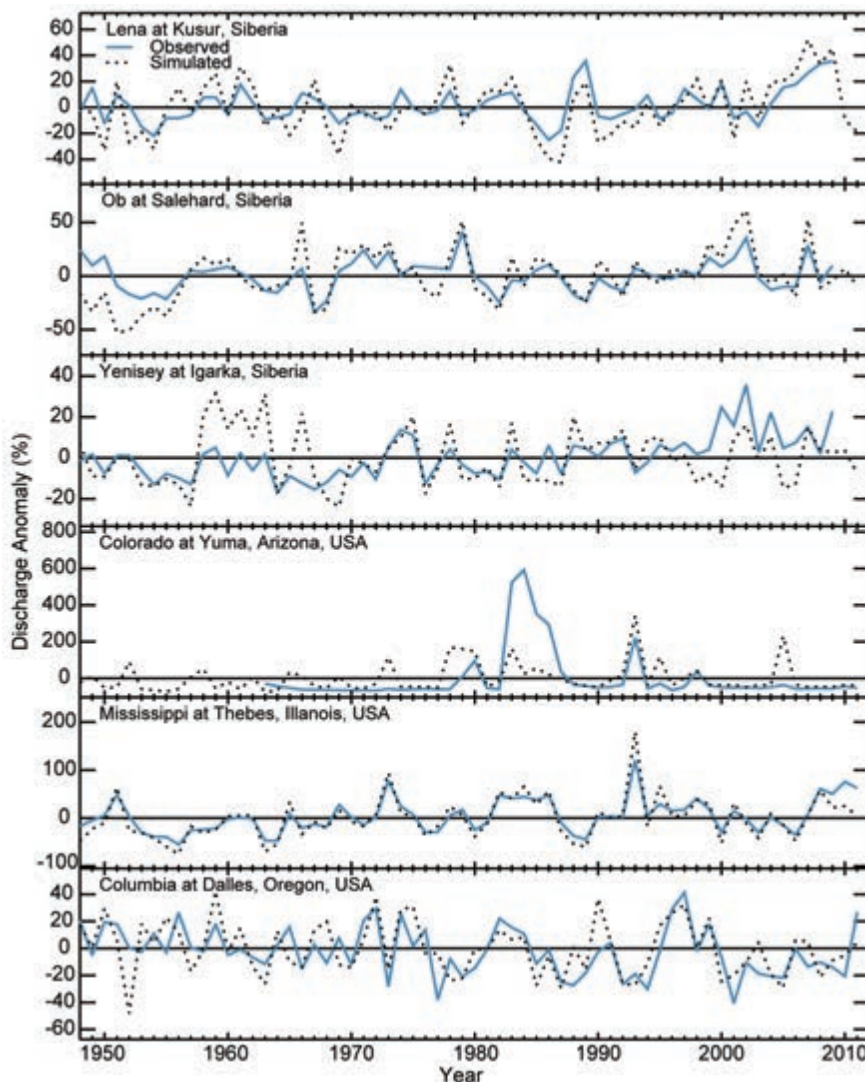


Fig. 2.26. Mean annual river discharge anomalies (%) for observed and simulated time series for the three largest Siberian rivers (observed near the river mouth) and three major river basins in the conterminous United States from the Arctic-RIMS archive. Data for the Siberian rivers are only available up to 2008. Simulations are based on the WBM analysis.

years (see Sidebar 7.2). Runoff into Arctic and Atlantic Oceans stayed near normal, while the Mediterranean and Black Seas experienced severe drought.

To assess these results, mean annual discharge anomalies with respect to their long-term means from six large river basins (three in Siberia from Arctic-RIMS1 archive and three in North America from USGS2) are compared with the WBM simulations in Fig. 2.26. With the exception of the Colorado River at Yuma (which is heavily regulated and significantly altered by extensive consumptive water use and interbasin transfers that are not currently adequately accounted for), the simulated river discharge anomalies follow the same patterns as the

observations, but often with different magnitude. These results suggest that the overall global runoff assessments are realistic for macroscale assessments of the hydrological cycle.

6) GROUNDWATER AND TERRESTRIAL WATER STORAGE—M. Rodell, D. P. Chambers, and J. S. Famiglietti

Groundwater is a vital resource and a dynamic component of the water cycle. Unconfined aquifer storage is less responsive to short-term weather conditions than the near-surface terrestrial water storage (TWS) components (soil moisture, surface water, and snow). However, with the exception of permanently frozen regions, it typically exhibits a larger range of variability over multiannual periods than the other components (Rodell and Famiglietti 2001; Alley et al. 2002). Groundwater is poorly monitored at the global scale, but TWS change data from the Gravity Recovery and Climate Experiment (GRACE; Tapley et al. 2004) satellite mission are a reasonable proxy for unconfined groundwater at climatic scales.

Plate 2.1k maps changes in mean annual TWS from 2010 to 2011, based on GRACE, reflecting hydroclimatic conditions in 2011 (see Plates 2.1e–i). Widespread drying occurred between 20°N and 60°N, contrasting with wetting between 10°S and 30°S. Severe drought impacted the southern United States and northern Mexico. Southern Europe, the north Atlantic coast of Africa, and parts of western and eastern China, experienced net losses of water in 2011 after having surpluses in 2010. Northern Sudan, which was already in drought, did not get any relief. South of the equator, the lower Amazon basin and some other parts of northern South America recovered from drought, while southern Africa had a relatively wet

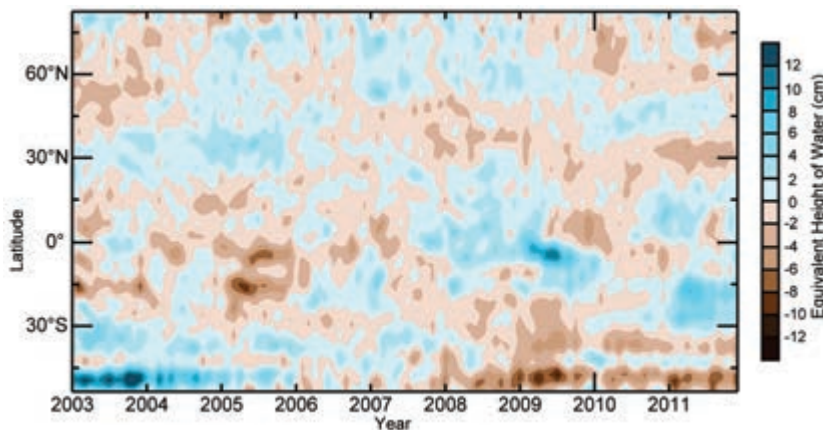


FIG. 2.27. GRACE satellite observations of annual mean terrestrial water storage (the sum of groundwater, soil water, surface water, snow, and ice, as an equivalent height of water in cm) anomalies (2003–07 base period) by latitude.

year. Other than continued replenishment of aquifers in the southeast, Australia reversed course from 2010, becoming wetter in the west and dryer in the north-east. Drought in equatorial Africa and recovery from drought in the Indochinese peninsula also stand out. Aquifers in central California (Famiglietti et al. 2011) and northern India (Rodell et al. 2009; Tiwari et al. 2009), which are stressed by groundwater pumping at

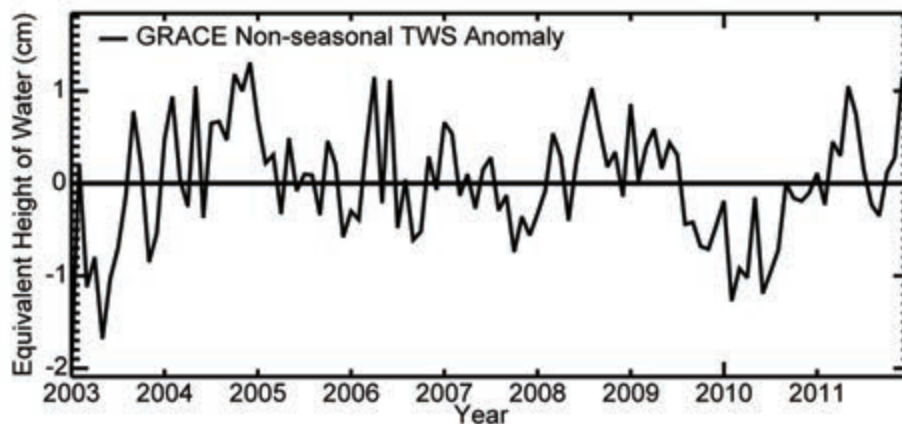


FIG. 2.28. As for Fig. 2.27 but for near-global average terrestrial water storage monthly mean anomalies (2003–07 base period) in cm equivalent height of water.

unsustainable rates, both raised their water levels in 2011. Significant reductions in TWS along the coast of Alaska, in the Patagonian Andes (also seen in Fig. 2.27), and in Greenland (see section 5f) and Antarctica (see section 6e) represent ongoing glacier and ice sheet ablation, not groundwater depletion.

Figures 2.27 and 2.28 show time series of zonal mean and global GRACE-derived non-seasonal, monthly mean TWS anomalies, excluding Greenland and Antarctica. Drying in the northern latitude band and wetting in the southern band in 2011 are clear

(Fig. 2.27). On average, Earth's land was relatively wet in 2011 (Fig. 2.28). From June 2010 to May 2011, global TWS increased by about 2.2 cm, which is equivalent to an 8 mm decline in mean sea level during that period (see Fig. 3.27), and TWS peaked again in December.

7) SOIL MOISTURE—R. A. M. De Jeu, W. A. Dorigo, R. M. Parinussa, W. W. Wagner, and D. Chung

Soil moisture retrievals from satellite observations are excellent indicators for climate variability because they integrate precipitation and evaporation. However, at

large spatial scales the variation of soil moisture, in turn, affects evaporation and precipitation, via the water availability for evaporation and the subsequent partitioning of the Earth surface energy fluxes (Senviratne et al. 2010).

Soil moisture has been globally observed from space since 1978 using microwave satellites (both passive and active), with a typical spatial resolution of about 0.25°.

Satellite soil moisture represents the water content of the top few centimeters. Recently, a consistent multidecadal record of global soil moisture was developed by harmonizing and merging different satellite soil moisture datasets (Y. Y. Liu et al. 2012; see Sidebar 2.2). This homogenized dataset was used to calculate surface soil moisture anomalies for 2011 by subtracting the

1979–2010 climatology. Annual 2011 anomalies (Plate 2.11) are predominantly positive in the Southern Hemisphere and negative in the Northern Hemisphere. Figure 2.29 reflects the major monthly hydroclimatic variations for 2011.

In early 2011, Australia suffered from several flooding events, especially in Queensland and Victoria, associated with La Niña conditions. From January to May the Okavango delta in southern Africa was completely flooded, resulting in a strong positive anomaly in the soil moisture data. This exceeded a

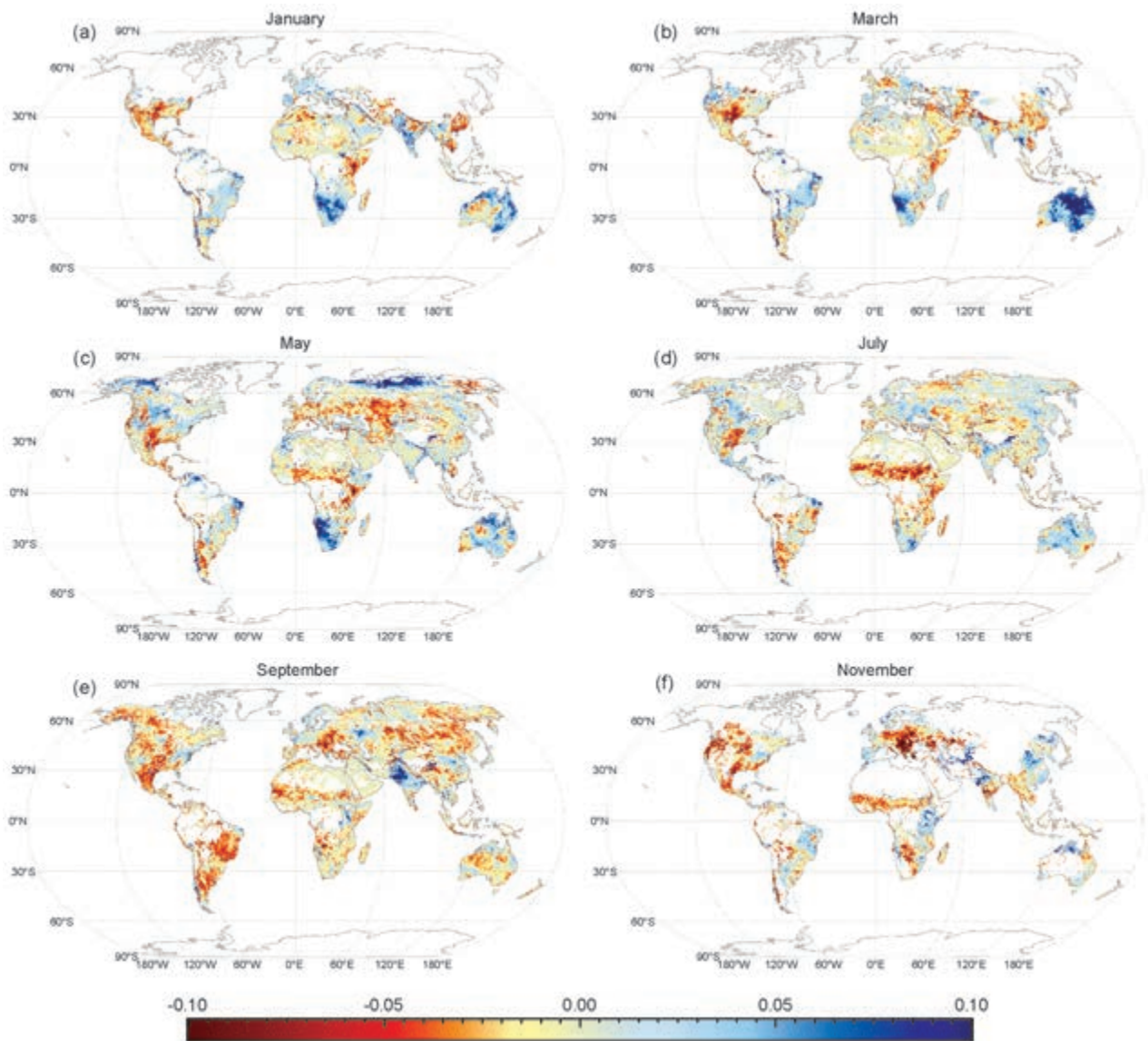


FIG. 2.29. Monthly soil moisture anomaly images for 2011 as derived from the multidecadal satellite soil moisture dataset. The anomalies are relative to a base period of 1979–2010. Note: The November anomaly image should carefully be interpreted; this image is solely based on ASCAT observations, because AMSR-E was switched off in October 2011.

similar flooding event in 2010 (De Jeu et al. 2011; Ives 2011). The delta is a large, flood-pulsed wetland and the flood was primarily caused by the seasonal flood wave of the Okavango River. Local rainfall variations played a smaller role. The flooding was asynchronous with the local rainy season and a result of interannual differences in local and upstream rainfall, as well as longer-term effects of surface-groundwater interactions within the delta (Wolski and Hudson 2008). The area of inundation displays a strong interannual variability, varying between 3500 km² and 14 000 km² (McCarthy et al. 2004; Gumbricht et al. 2004)

Following major flood events in 2010, Pakistan again experienced a series of flood events between July and September due to strong monsoonal rains. These are clearly visible in the September anomaly image of Fig. 2.29. However, the flood events of 2011 covered a smaller area than the events in 2010 (De Jeu et al. 2011).

In 2011, three regions experienced severe droughts: the Horn of Africa, the southern US, and eastern Europe (see sections 7e, 7b, and 7f, respectively). The Horn of Africa drought became visible in soil moisture in March 2011 and persisted for the rest of the year. The southern US drought region showed a

SIDEBAR 2.2: BUILDING A CLIMATE RECORD OF SOIL MOISTURE FROM HISTORICAL SATELLITE OBSERVATIONS—R. A. M. DE JEU, W. A. DORIGO, R. M. PARINUSSA, W. W. WAGNER, Y. Y. LIU, D. CHUNG, AND D. FERNÁNDEZ-PRIETO

Since the launch of the Nimbus-7 satellite in October 1978, there is a long legacy of satellite observations suitable for global soil moisture monitoring (Fig. SB2.4), but it took more than 20 years to develop the first satellite global soil moisture dataset. In 2002, a dataset was developed from scatterometer observations on-board the European Remote Sensing Satellites ERS-1 and ERS-2 (Wagner et al. 2003). Other research groups soon followed. De Jeu and Owe (2003) made a global soil moisture product from the historical Nimbus-7 SMMR data and Njoku et al. (2003) presented the first dataset based on AMSR-E observations.

Today, numerous global soil moisture products from various satellites and research groups are freely available. These datasets vary in quality but all provide global soil moisture estimates of the top few centimeters at a rather coarse spatial resolution of 25 km–50 km (GCOS 2011). Global datasets are increasingly important in environmental research. For example, Liu et al. (2007) demonstrated the impact of El Niño on water resources in eastern Australia using TRMM soil moisture. Brocca et al. (2010) showed that runoff prediction for the Tiber River in Italy can be improved by incorporating ASCAT soil moisture, and Jung et al. (2010) used TRMM soil moisture to investigate a recent decline in global evaporation.

These different datasets are even more valuable if combined into one consistent multidecadal climate data record. This was addressed as part of the Water Cycle Multimission Observation Strategy (WACMOS) project from the Support To Science Element (STSE) program of the European Space Agency (ESA). Within this project, two extensively validated soil moisture products were selected to create a harmonized dataset; one from the Vienna University of Technology (TU Wien) based on active microwave observations (Wagner et al. 2003; Bartalis et al. 2007) and one from the VU University Amsterdam in collaboration with NASA, based on passive microwave observations (Owe et al. 2008). The harmonization of these datasets incorporates the strengths of both microwave techniques and spans continuously from 1978 onwards (Fig. SB2.4). However,

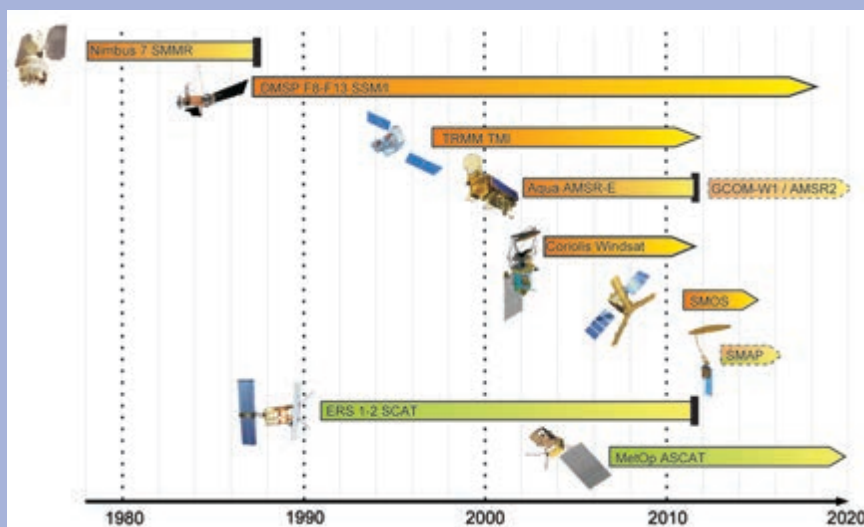


FIG. SB2.4. Timeline of past, current, and future space-borne coarse resolution radiometers (orange) and scatterometers (green) suited for soil moisture retrieval on a global scale. (Source: updated version of Dorigo et al. 2010)

there were several challenges to developing such a dataset, e.g., differences in instrument specifications result in different absolute soil moisture values, the global passive and active microwave retrieval methods produce conceptually different quantities, and products vary in their relative performances depending on vegetation cover (Y. Y. Liu et al. 2012, manuscript submitted to *Remote Sens. Environ.*). This is clearly visible in Fig. SB2.5, where the original soil moisture retrievals from various satellites are plotted for a region in the Sahel. Here, both the active and passive soil moisture retrievals show similar seasonality but they have different magnitudes. TU Wien soil moisture retrievals are expressed as a degree of saturation (with a value between 0 and 1) while VUA retrievals are given in volumetric values ($\text{m}^3 \text{m}^{-3}$). Besides this, the SSM/I-based estimates are less accurate than for the other sensors, owing to its limited soil moisture retrieval capabilities. It carries a Ku band (19 GHz) radiometer, which is less suitable for soil moisture retrieval than L (1.4 GHz), C (6.9 GHz), and X (10.7 GHz) band radiometers (Owe et al. 2008). A statistical methodology based on scaling, error characterization, ranking, and blending was developed to address these issues to create one consistent dataset (Liu et al. 2011, 2012). A third soil moisture dataset, provided by a land surface model (GLDAS-1-Noah), was used to scale the different satellite-based products to the same range. The blending of the active and passive datasets was based on their respective sensitivity to vegetation cover. While this approach imposes

the absolute values of the land surface model dataset to the final product, it preserves the relative dynamics (e.g., seasonality, interannual variations) and trends of the original satellite-derived retrievals (Y. Y. Liu et al. 2012). The ranking and blending strategy used does not increase the accuracy of the final product with respect to the merged ones, but allows a selective use of the most accurate measurements and increases the temporal density of the observations available. Finally, this method allows the long-term product to be extended with data from other current (e.g., SMOS) and future operational satellites and will be further improved as part of ESA Climate Change Initiative program (<http://www.esa-cci.org/>).

A simple trend analysis of this harmonized dataset is presented in Fig. SB2.6. Subtle soil moisture trends can be seen over the entire globe varying from $-0.06 \text{ m}^3 \text{ m}^{-3}$ to $0.06 \text{ m}^3 \text{ m}^{-3}$ over the last 31 years. The strongest negative trends can be found in Russia, Kazakhstan, and the Sahel region. Strong positive trends are observed in northeastern Brazil and southern Africa. Most of these trends can directly be linked to the behavior of ocean oscillation systems. For example, the trends over Australia could be related to the polar movement of the Subtropical Ridge (STR), the Indian dipole, and the severe El Niño conditions within this period (Liu et al. 2007; Murphy and Timbal 2008; Y. Y. Liu et al. 2009).

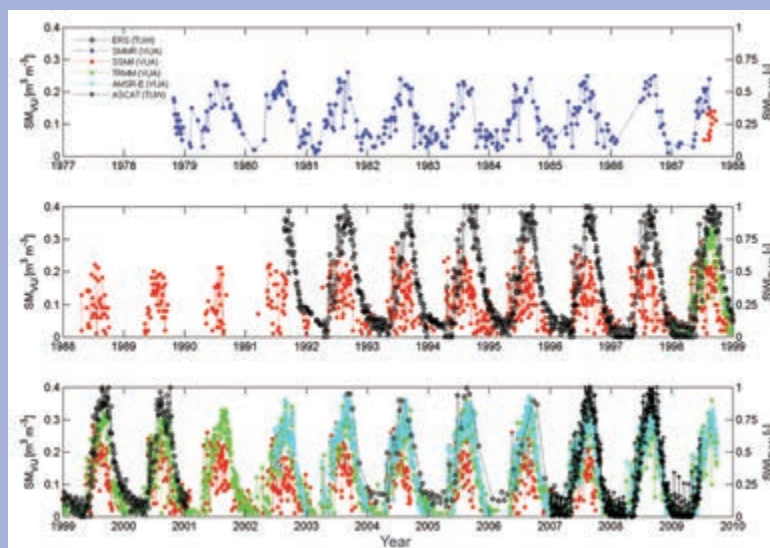


FIG. SB2.5. Soil moisture over an area in the Sahel region (7°N, 12°E) according to different satellite observations. Note that soil moisture derivations from scatterometer sensors (indicated in black) are expressed as an index (right axis) and the VU soil moisture retrievals are expressed in $\text{m}^3 \text{ m}^{-3}$ (left axis). (Source: De Jeu et al. 2009)

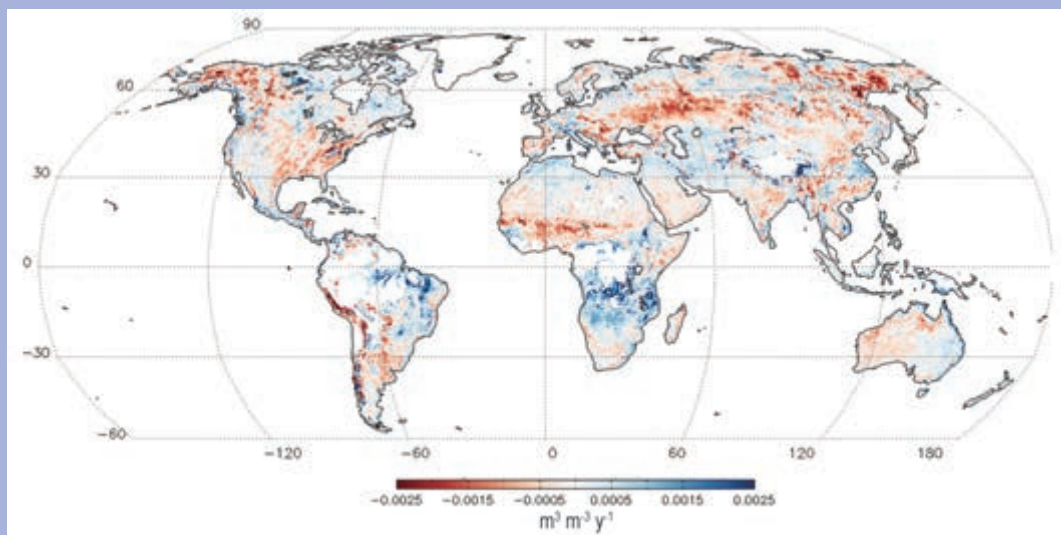


FIG. SB2.6. Trends in annual average satellite soil moisture (in $\text{m}^3 \text{ m}^{-3} \text{ yr}^{-1}$), 1979–2010 base period. These values were derived from the harmonized soil moisture dataset, a 30+ year harmonized satellite soil moisture data record based on (historical) passive and active microwave observations.

negative anomaly throughout the year, and the Central and Eastern European drought was observable in the soil moisture data in November 2011.

8) LAKE LEVELS—C. Birkett and J.-F. Cretaux

Lake volumes are indirect indicators of climatic change because they respond to changes in precipitation integrated over their catchment basins. The response can be seen in open lakes and reservoirs but is particularly marked for closed lakes, i.e., those having no significant surface or subsurface outflow. Closed lakes can act as low-pass filters to variations in aridity, with a characteristic time constant of between 1 and 1000 years, depending largely on lake geomorphology. Deep lakes with steep shore topography are good proxies for high amplitude-low frequency changes, while shallow water basins are better indicators for rapid low-amplitude changes (Hostetler 1995). Lake variations can correlate with several modes of variability, e.g., ENSO, Indian Ocean, Pacific decadal, or North Atlantic Oscillations.

Research studies in 2011 continued to be regional or local in scope (Lee et al. 2011; Sarmiento and Palanisami 2011; Zhang et al. 2011), but global analyses require the systematic monitoring of all global lake volumes. Satellite imagery could provide changing lake surface area but currently no operational products exist. Satellite-based radar altimetry continues to provide surface water elevation products with datasets spanning 20 years (1992–2012). These lake level datasets can stand alone or be combined with ground-based measurements. They have varying temporal/spatial resolutions and varying accuracies, ranging from a few centimeters to tens of centimeters. Several web sites offer altimetric lake level products (e.g., NASA/USDA, ESA, LEGOS). The NASA/USDA website currently provides a first-order water-level status guide to drought or high water conditions in both lakes and reservoirs (Fig. 2.30). This is based on a mean nine-year lake level datum derived from a subset of the Topex/Poseidon dataset (1993–2002). Of the ~75 lakes, in February 2012, a third had below-average levels, another third above-average water levels. True climatic interpretation of the reservoir results are hampered by the magnitude of unknown anthropogenic effects. This status map at the NASA/USDA web site will be discontinued during 2012 as the operational program changes its policy to employ a datum based on a single date to enable an improvement in product accuracy. An ideal global lakes database would continue with such a level or volume

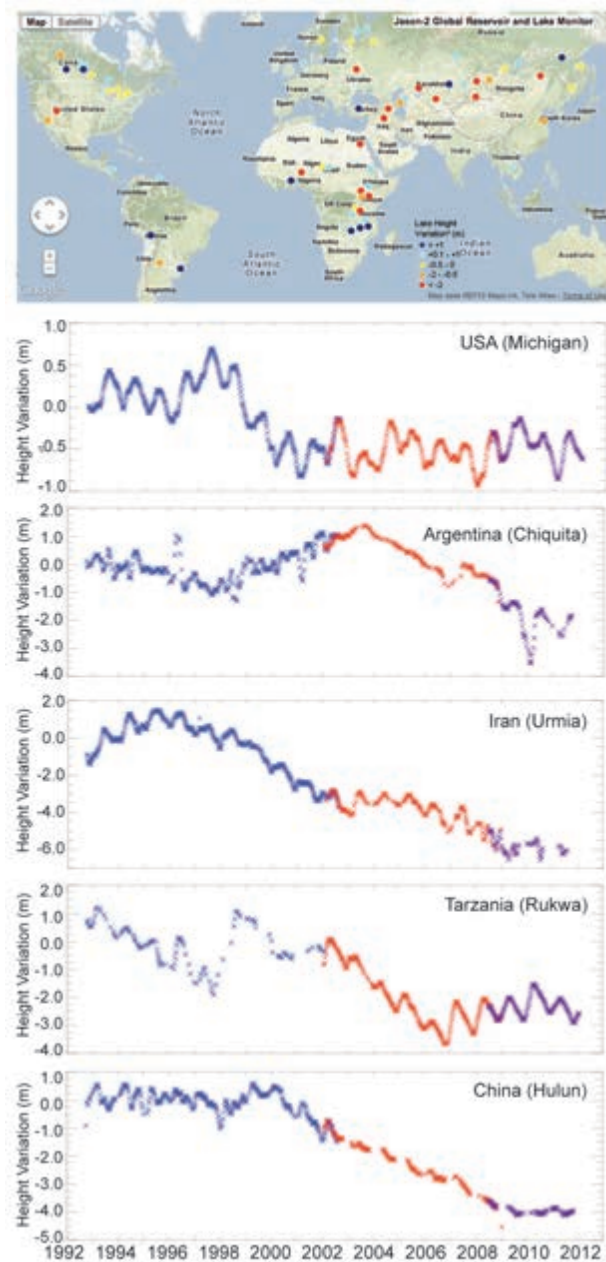


FIG. 2.30. (Top) Map showing the near-real-time (as of end of 2011) lake-level status of ~70 lakes with respect to a short-term mean (1993–2002). Red depicts low water drought and navy depicts high water. (Bottom) Examples of lake level time series (m) for five countries. (Source: USDA/FAS CropExplorer)

status indicator, as well as provide other parameters such as lake areal extent, surface water temperature and salinity, ice cover duration and thickness and basin-scale water storage anomalies. The type of lake included should also expand to include ephemeral lakes in both water-challenged and high latitude regions.

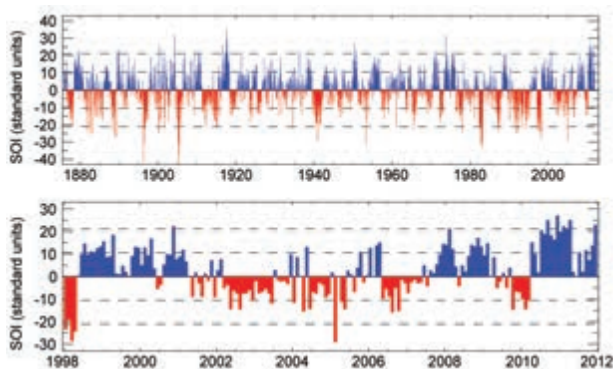


FIG. 2.31. The Southern Oscillation index (SOI) time series (top) from 1876–2012 and (bottom) for the 1998–2011 period. Data are from HadSLP2r (Allan and Ansell 2006).

e. *Atmospheric circulation*

1) *MEAN SEA LEVEL PRESSURE*—R. Allan and C. K. Folland

The La Niña that developed in mid-2010 (apparent in Plate 2.1m) became one of the strongest, in terms of the Southern Oscillation index (SOI) in the historical instrumental record (Fig. 2.31, top). By mid-2011 it had declined but then later resurged to a more moderate La Niña (Fig. 2.31, bottom). It resulted in major precipitation and temperature impacts across the entire Indo-Pacific region, and at higher latitudes in both hemispheres (Plate 2.1).

El Niño and La Niña can be measured by the SOI, the normalized mean sea level pressure (MSLP) difference between Tahiti and Darwin (Allan et al. 1996). Other indices using SST are also commonly utilized (see Kaplan 2011), and these can differ in year-to-year magnitude relative to the atmospheric indicators shown here. El Niño (negative SOI) and La Niña (positive SOI) events vary in magnitude, duration, and evolution, with no two events or episodes exactly the same. There is also the propensity in the climate system for the occasional development of protracted El Niño and La Niña episodes (Allan et al. 2003), when a La Niña (El Niño) event appears to be ending and/or moving into an El Niño (La Niña) only to be revitalized and continue as an La Niña (El Niño). Figure 2.31 (top) shows the presence of these protracted El Niño and La Niña episodes in the SOI record since 1876, and that they can last for up to six years (e.g., 1990–95 protracted El Niño). El Niño and La Niña events can be near-global in their influence on world weather patterns, owing to ocean-atmosphere interactions across the

Indo-Pacific region with teleconnections to higher latitudes in both hemispheres.

The Antarctic Oscillation (AAO), otherwise known as the southern annular mode (SAM; Kaplan 2011), was notably positive from December 2011 through January 2012. This is clearly identified by the low pressure anomalies over southern high latitudes in Fig. 2.32b (see also section 6b).

The Northern Hemisphere winters of 2010/11 and 2011/12 experienced contrasting North Atlantic Oscillation (NAO)/Arctic Oscillation (AO) conditions (Figs. 2.32a,c compared with 2.32b,d). In 2010/11, the NAO/AO indices were dominated, especially initially, by long periods of extremely negative values, with positive pressure anomalies over higher latitudes and negative anomalies over the midlatitudes, and an associated reduction in the westerlies over the North Atlantic–European sector. This contrasted with the early 2011/12 boreal winter, when a major phase of the opposite conditions prevailed.

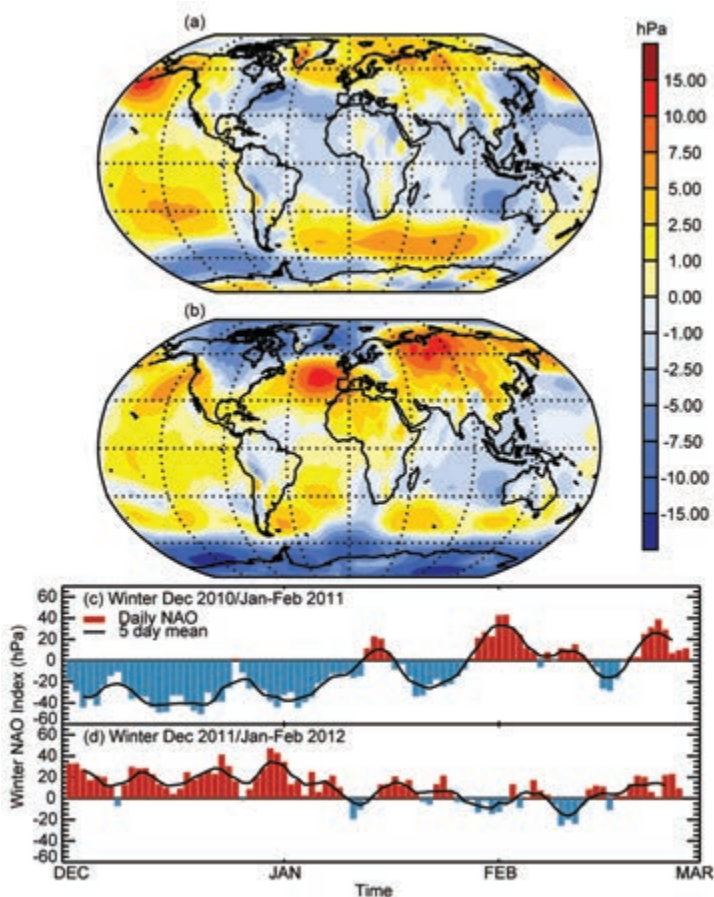


FIG. 2.32. Winter NAO patterns for December 2010–February 2011 and December 2011–February 2012. (a) and (b) HadSLP2r sea level pressure anomalies (hPa; 1961–1990 base period). (c) and (d) Daily NAO Index (hPa) where red bars show the positive phase and blue bars show the negative phase.

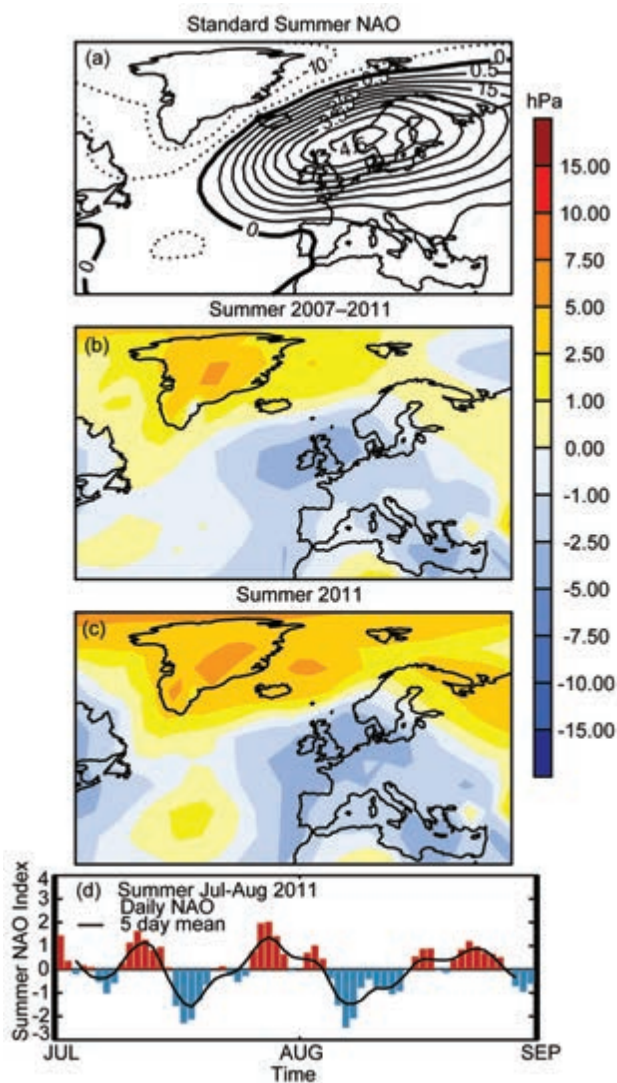


FIG. 2.33. Summer NAO patterns for July to August. (a) Standard pattern in hPa anomalies, (b) and (c) HadSLP2r sea level pressure anomalies (hPa; 1961–90 base period), and (d) daily summer NAO index (Folland et al. 2009) where red bars show the positive phase and blue bars show the negative phase.

In boreal summer, especially July and August, there is a comparable atmospheric circulation pattern to the winter NAO known as the summer NAO (SNAO; Folland et al. 2009). This is more restricted in latitude (Fig. 2.33a) and explains a somewhat smaller fraction of sea level pressure variance. Its southern node stretches from the northeast Atlantic to Scandinavia, such that when the SNAO is positive, this area has an anticyclonic anomaly, bringing generally warm and dry conditions to northwest Europe. There is a corresponding northward shift of the jet stream. Figure 2.33d shows the standardized daily time series of the SNAO index for summer 2011, indicating a neutral mean state. However, this reflected a southward

shifted negative southern node (Fig. 2.33c) that gave a rather cool, wet, summer over many parts of the UK, though Scandinavia, while rather wet overall was generally warm (see section 7f for more details). The SNAO shows pronounced multiannual to multidecadal variations like the winter NAO, but uncorrelated with winter NAO variability over the last 150 years. Figure 2.33b shows sea level pressure anomalies in July and August averaged over 2007–11 near Europe. A strong impact of the negative SNAO pattern (-0.66 standard deviations) was wetter than normal conditions over the southern node (not shown). The previous five-year mean (2002–06), including the two very warm UK summers of 2003 and 2006, was by contrast $+0.64$ standard deviations.

2) SURFACE WINDS

(i) Land surface winds and atmospheric evaporative demand—R. Vautard, T. R. McVicar, J.-N. Thépaut, and M. L. Roderick

Land surface winds have a major influence on society and the economy, impacting infrastructure, forests, wind energy production, hydrology, and ecosystems through land-surface exchanges. Long-term wind changes are difficult to characterize because measurements have undergone changes in location, observation protocols, and techniques in many places. Nevertheless, many regional studies concur in declining surface wind speeds in the mid-

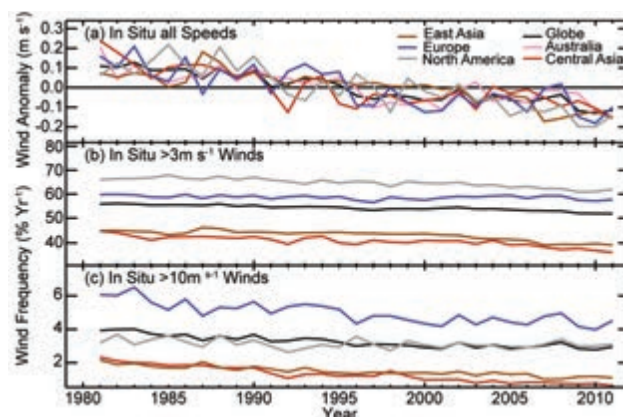


FIG. 2.34. Global and regional average annual mean land wind speed (a) anomalies (1981–2011 base period), (b) frequency of wind speeds $> 3 \text{ m s}^{-1}$ and (c) frequency of wind speeds $> 10 \text{ m s}^{-1}$. Region definitions, means, and trends are shown in Table 2.2. In all panels global data do not include Australian data since the two datasets have undergone different processing procedures, and while the mean Australian anomaly is shown in (a), occurrence frequencies were not calculated for Australia in (b) and (c).

TABLE 2.2. Global and regional average wind speeds and trends over the 1981–2011 period. Number of stations varies year to year. Global data do not include Australian data since the two datasets have undergone different processing procedures.

Region	Area definition	Mean Wind Speed (m s^{-1})	Trend ($\text{m s}^{-1} \text{ yr}^{-1}$)	Number of Stations
Globe	NA	3.5	-0.0078	1100
Europe	20°W, 40°E; 30°N, 75°N	3.9	-0.0086	410
Central Asia	40°W, 100°E; 30°N, 75°N	2.5	-0.0085	50
East Asia	100°W, 160°E; 30°N, 75°N	2.7	-0.0077	230
North America	17°W, 50°W; 30°N, 75°N	4.1	-0.0105	250
Australia	NA	2.1	-0.0069	44

latitudes and the tropics and increasing winds in the high latitudes (see McVicar et al. 2012 for a global review). A major part of this trend in the Northern Hemisphere appears attributable to land cover changes, including forest growth, reforestation programs, cropland abandonment, and urbanization (Vautard et al. 2010), and also increased aerosol levels (Jacobson and Kaufman 2006).

In 2010, mean land surface wind speeds, as averaged over a site ensemble selected by Vautard et al. (2010), were shown to reach record-low values (Peterson et al. 2011a). Here, the NOAA ISD-LITE database was utilized, quality controlled similarly to Vautard et al. (2010), and augmented with Australian data (McVicar et al. 2008). The quality control leads to an objective selection retaining more than 1000 stations with observations over 1981 to 2011. With this dataset, 2011 constitutes the third weakest land surface winds year (Fig. 2.34a). In each large region of the Northern Hemisphere, mean surface wind speed was also very low, especially over Asia (record low over central Asia, second lowest value over East Asia). Over North America, the mean wind was third lowest and over Europe, sixth lowest. In the Southern Hemisphere, 2011 mean wind over Australia was also record low.

Changes in the mean frequency of surface wind speeds larger than 3 m s^{-1} are shown in Fig. 2.34b. Globally, this frequency for 2011 (51.8%) was a new record low, just below the 2010 value (51.9%). For stronger wind speeds ($> 10 \text{ m s}^{-1}$), the 2011 frequency was 25% below the frequencies found ~30 years ago; note the record low in central Asia (Fig. 2.34c). Exactly how these changes relate to wind speeds aloft remains an interesting research question, with potential implications for renewable wind energy (McVicar et al. 2012; Mostafaeipour 2010; Cheng et al. 2012).

The wind anomaly pattern resembled that of 2010 (see Peterson et al. 2011a and Plate 2.1n), with strong negative anomalies over China, eastern North America, Asia, Australia, and western Europe contrasting with positive anomalies found at several high-latitude regions (McVicar et al. 2012, table 2). Over northwest North America and Scandinavia, ERA-Interim (Dee et al. 2011a), reproduced the observed positive anomalies reasonably well, although with smaller magnitude (compare Fig. 2.35 with Plate 2.1n). Negative anomalies are found over central Europe, Asia, and, to a lesser extent, eastern North America. The dissimilarity between reanalysis and observed land wind speed trends has been previously

documented in both the Northern (Pryor et al. 2009) and Southern Hemispheres (McVicar et al. 2008). Many global climate models also do not concur with observed land winds (Johnson and Sharma 2010, table 5). On the other hand, reanalyses over oceans are in broad agreement with observations (section 2e2ii).

These anomalies and trends in wind speed bear significance for water resources. The kinetic energy in the wind is small by comparison with the turbulent (latent and sensible) heat fluxes at the surface (Peterson et al. 2011b). Despite this, the worldwide declines in pan evaporation, known as the “pan evaporation paradox” (i.e., declining pan evaporation rates in a warming globe), have been partly attributed to declining wind speeds (Roderick et al. 2007; McVicar et al. 2012, table 7). Reported declines in pan evaporation vary substantially between sites, but in the most intensively studied regions to date (US, China, and Australia), large-scale spatial averages decline at a rate of $\sim 2 \text{ mm yr}^{-1} \text{ yr}^{-1}$ over the last 30–50 years (Fig. 2.36;

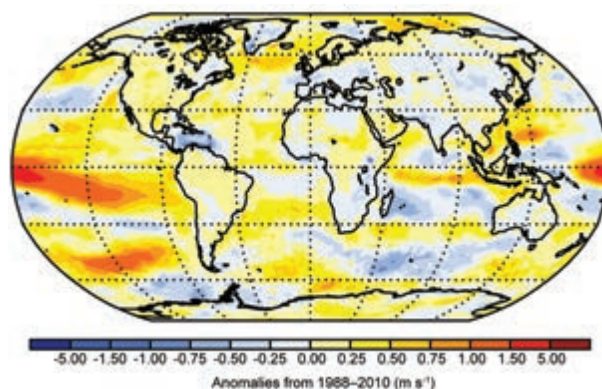


FIG. 2.35. ERA-Interim 2011 anomalies (m s^{-1} ; 1988–2010 base period for comparison with Plate 2.1n) for surface wind speed.

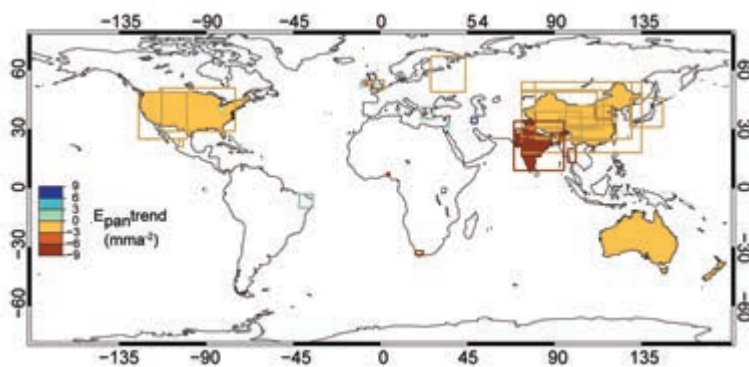


FIG. 2.36. Recent observed rates of pan evaporation trends (mm yr^{-1}) from 55 regional studies. There is incomplete geographic coverage (as shown) and the studies have different start and end dates. (Source: McVicar et al. 2012, Table 5)

McVicar et al. 2012). The hydrological implications of changing atmospheric evaporative demand are geographically variant (see Donohue et al. 2007). In extremely water-limited locations this change will have negligible implications for water resources as evaporation is already limited by water. However, in energy-limited locations and those straddling the energy-limit / water-limit divide (Viviroli et al. 2007), observed trends in atmospheric evaporative demand will have important impacts for water resource availability (Roderick et al. 2009; McVicar et al. 2012).

(ii) *Ocean surface winds*—C. Mears

Surface wind speed over the oceans has been monitored continuously by satellite-borne microwave radiometers since the launch of the first Special Sensor Microwave/Imager (SSM/I) satellite in late 1987. These instruments make measurements of upwelling microwave radiation to infer the surface roughness of the world's oceans, and thus the surface wind speed (Wentz 1997). Since the first SSM/I instrument, a

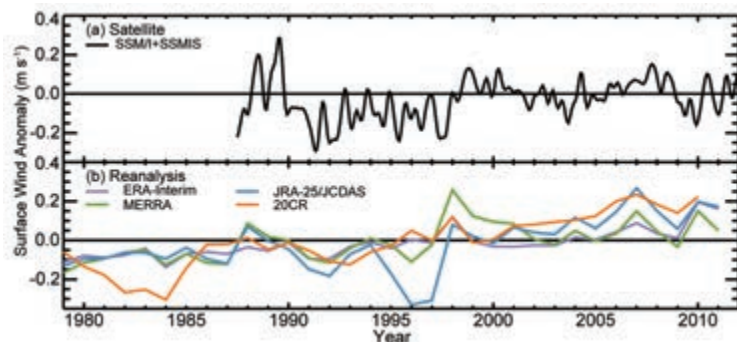


FIG. 2.37. Surface wind speed anomalies (m s^{-1} ; 1988–2010 base period) over the global ice-free oceans as measured by Remote Sensing Systems from satellite-borne microwave radiometers (available online at <http://www.remss.com>) and reanalyses products as described in Fig. 2.1. The satellite time series has been smoothed to remove variability on time scales shorter than four months.

number of additional microwave imaging sensors have been launched and intercalibrated to the accuracy necessary for climate studies (Wentz et al. 2007). Globally-averaged ocean surface winds (Fig. 2.37) exhibited a maximum in 1988–89, followed by a minimum in 1991, and an increasing trend from 1990 to 2007. In 2008–09, global ocean wind speed fell slightly, followed by recovery in 2010–11. Reanalyses show a steady increase over time, with some variability between the products. The earlier record (up to early 1990s) is less certain than later times due to fewer simultaneous

satellite observations and calibration uncertainty for the first two SSM/I instruments.

Global anomalies for 2011, relative to the 1988–2010 base period, showed large positive anomalies in the central tropical Pacific, the South Pacific east of 180°W , and in the North Atlantic near 55°N . The

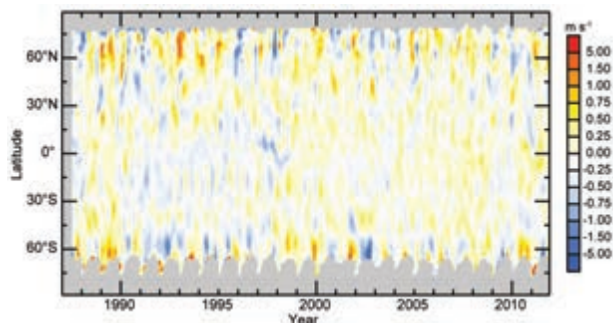


FIG. 2.38. Satellite radiometer monthly mean anomaly (m s^{-1} ; 1988–2010 base period) surface wind speed over the ice-free oceans averaged by latitude. Data have been smoothed in time to remove variability on time scales shorter than four months. Gray areas indicate regions where data are unavailable.

latter coincided with the positive phase of the NAO (Hurrell et al. 2003; section 2e1) during the cool season months in 2011. Strong negative anomalies occurred east of Madagascar, in the Caribbean Sea, and in the mid-latitude North Pacific (Fig. 2.38; Plate 2.1n).

f. *Earth radiation budget at the top-of-atmosphere*—T. Wong, P. W. Stackhouse Jr., D. P. Kratz, P. Sawaengphokhai, A. C. Wilber, and N. G. Loeb
Analyses of the Clouds and the Earth's Radiant Energy System (CERES; Wielicki et al. 1998) instrument data taken from the combined NASA Terra and Aqua

TABLE 2.3. Global annual mean TOA radiative flux changes between 2010 and 2011, the 2011 global-annual mean radiative flux anomalies relative to the 2001–11 base period, and the 2-sigma interannual variabilities of 2001–11 global-annual mean fluxes (units in W m^{-2}) for the outgoing longwave radiation (OLR), total solar irradiance (TSI), reflected shortwave (RSW), and total net fluxes. All flux values have been rounded to the nearest 0.05 W m^{-2} .

	One Year Change (2011 minus 2010)	2011 Anomaly (relative to climatology)	Interannual Variability (2001 to 2011)
OLR	-0.45	-0.30	± 0.55
TSI	+0.05	+0.05	± 0.20
RSW	-0.20	+0.15	± 0.40
Net	+0.70	+0.20	± 0.65

spacecraft revealed that between 2010 and 2011, the global-annual mean outgoing longwave radiation (OLR) decreased by $\sim 0.45 \text{ W m}^{-2}$ and the reflected shortwave radiation (RSW) also decreased by $\sim 0.20 \text{ W m}^{-2}$ (Table 2.3). Data from the Solar Radiation and Climate Experiment (SORCE; Kopp et al. 2005; Kopp and Lean 2011) indicated that the global annual average total solar irradiance (TSI) increased by $\sim 0.05 \text{ W m}^{-2}$ from 2010 to 2011. Thus, the changes in the combined global-annual averaged OLR and absorbed shortwave (TSI – RSW) fluxes resulted in an enhancement of $\sim 0.70 \text{ W m}^{-2}$ in total net radiation into the Earth climate system for 2011 as compared with 2010. The data between July 2011 and December 2011, however, may include modest instrument drift artifacts (below $\pm 0.1\%$), since the final instrument calibration coefficients for those months are not yet available. Relative to the multiyear dataset average for 2001–11, the 2011 global-annual mean anomaly (Table 2.3) is -0.30 W m^{-2} , $+0.05 \text{ W m}^{-2}$, $+0.15 \text{ W m}^{-2}$, and $+0.20 \text{ W m}^{-2}$ for OLR, TSI, RSW, and total net radiation, respectively. These results are within the corresponding 2-sigma interannual variability for this period.

Global monthly mean deseasonalized anomalies since March 2000 have been produced by merging Earth Radiation Budget (ERB) datasets from two sources: (1) the CERES EBAF (Energy Balanced And Filled) Top-of-Atmosphere (TOA) Ed2.6r $1^\circ \times 1^\circ$ product using the Edition 3 instrument calibration; and (2) the CERES Fast Longwave and Shortwave Radiative Fluxes (FLASHFlux) product (Stackhouse et al. 2006; L’Ecuyer et al. 2008). The results are presented in Fig. 2.39, where the FLASHFlux data have been normalized to the EBAF 1Deg data using TOA fluxes from both datasets for the four-year period from March

2007 through February 2011. The 2-sigma monthly uncertainty of the merge procedure is $\pm 0.20 \text{ W m}^{-2}$, $\pm 0.10 \text{ W m}^{-2}$, and $\pm 0.15 \text{ W m}^{-2}$ for the OLR, RSW, and total net radiation, respectively. The OLR oscillated irregularly in 2010 and 2011, in accord with anomalies from the Atmospheric Infrared Sounder (AIRS) OLR data (monthly AIRX3STM.005 product) for the same period (not shown). Besides ENSO variations, large changes in the North Atlantic Oscillation (NAO) during 2011 may have contributed to the observed large fluctuations in OLR anomaly

at the end of the record, which require further study. Changes in the absorbed shortwave (TSI – RSW) showed similar features with a smoother curve. The total net anomaly, which contains the combined OLR and absorbed shortwave anomaly, oscillated between positive and negative during 2011. This oscillation is an intrinsic feature of the climate system. Since

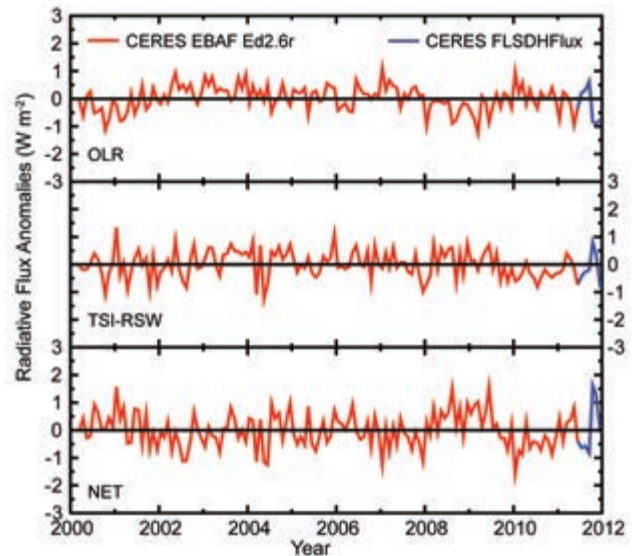


FIG. 2.39. Global monthly-mean deseasonalized anomalies (Mar 2000–Dec 2011 base period) of TOA Earth Radiation Budget for (upper panel) OLR, (middle panel) absorbed shortwave (TSI – RSW), and (lower panel) total net (TSI – RSW – OLR). Anomalies are computed relative to the calendar month climatology. The time series show the CERES EBAF Ed2.6r 1° data (Mar 2000–Jun 2011) by a red line and the CERES FLASHFlux data (Jul–Dec 2011) by a blue line. Mean differences between datasets were removed using available data from the overlap period (Mar 2007–Feb 2011) and the combined time series was anchored to the absolute value of the CERES EBAF Ed2.6r 1° results before deseasonalization.

changes in the ENSO intensity strongly influence the global averaged monthly TOA radiation budget variability during much of CERES period (Loeb et al. 2012), further fluctuations in TOA radiation budget are anticipated as the ENSO cycle evolves. Long-term trend analyses from this combined CERES EBAF and FLASHFlux record are discouraged due to the natural fluctuation in ERB relating to ENSO activity in the short record, the uncertainty from the data merging process, and instrument drift potential in the FLASHFlux data. A long-term homogeneous data source with in-depth instrument stability analysis (e.g., extended CERES EBAF-only dataset) is required to reduce uncertainties in the future.

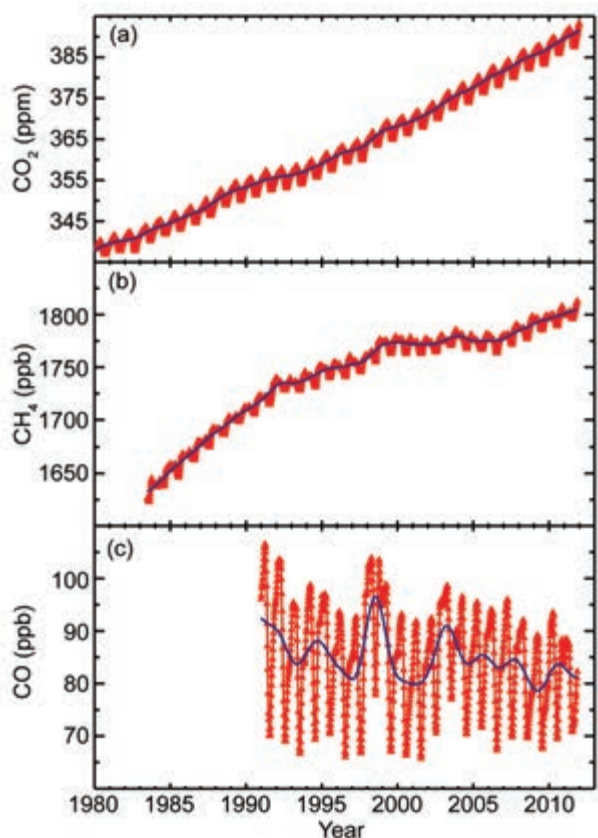


FIG. 2.40. Globally averaged trace gas dry air mole fractions of (a) CO_2 (ppm), (b) CH_4 (ppb), and (c) CO (ppb) from discrete air samples collected approximately weekly from sites in NOAA's global cooperative air sampling network and analyzed at ESRL in Boulder, Colorado. Symbols are weekly zonal means, red lines are smooth curves fitted to the data, and blue lines are deseasonalized trend curves.

g. Atmospheric composition

1) ATMOSPHERIC CHEMICAL COMPOSITION

(i) Carbon dioxide, methane, and carbon monoxide—

E. J. Dlugokencky

Anthropogenic carbon dioxide (CO_2) emissions from fossil fuel combustion are the main source of anthropogenic greenhouse gases. Despite concerns about the radiative impacts of increasing atmospheric CO_2 (Forster et al. 2007), global fossil fuel emissions have increased in recent decades (Peters et al. 2012). Based on preliminary emissions estimates in Peters et al., the recent global financial crisis resulted in only a small (1.4%) decrease in CO_2 emissions from fossil fuel combustion and cement production. In 2010, emissions are estimated to have increased globally by 5.9% over 2009 to $9.1 \pm 0.5 \text{ Pg C}$ ($1 \text{ Pg} = 10^{15} \text{ g}$). Most of this increase resulted from a 10% increase in emissions by the world's largest fossil fuel CO_2 emitter, China.

The terrestrial biosphere is both a source and sink for atmospheric CO_2 . Estimated average emissions of CO_2 from land-use change (e.g., deforestation) were $1.1 \pm 0.7 \text{ Pg C yr}^{-1}$ for the period 2000–09 (Friedlingstein et al. 2010; see also section 2h1). The net effect of vegetation is a sink for CO_2 , with estimated uptake during 2010 of $2.6 \pm 1.0 \text{ Pg C}$, mostly by the world's forests (Pan et al. 2011). The other major sink for anthropogenic CO_2 is ocean uptake, which was estimated to be $2.4 \pm 0.5 \text{ Pg C}$ (Peters et al. 2012), but in some ocean regions this sink may be decreasing (McKinley et al. 2011).

In 2011, globally averaged atmospheric CO_2 at Earth's surface reached 390.4 ppm ($\text{ppm} = \mu\text{mol mol}^{-1}$, dry air), surpassing 390 ppm for the first time (Fig. 2.40a). Globally averaged CO_2 increased by $2.10 \pm 0.09 \text{ ppm}$ (where uncertainty is 68% confidence limit) over 2011. This was slightly larger than the average increase from 2000 to 2011 of $1.96 \pm 0.36 \text{ ppm yr}^{-1}$.

After carbon dioxide, methane (CH_4) is the most important long-lived greenhouse gas, contributing $\sim 0.5 \text{ W m}^{-2}$ direct radiative forcing (see section 2g1v). Indirect effects, from production of tropospheric ozone (O_3) and stratospheric water (H_2O), add another $\sim 0.2 \text{ W m}^{-2}$. Methane has a global warming potential (GWP) of 25; this means that, integrated over a 100-year time scale, the radiative forcing from a given pulse of CH_4 emissions is estimated to be 25 times greater than a pulse of the same mass of CO_2 . Its GWP includes the indirect effects of tropospheric O_3 and stratospheric H_2O , and the impact of increasing CH_4 on atmospheric chemistry, which increases its lifetime.

After about a decade of steady mixing ratios (mole fraction), atmospheric CH_4 began increasing again in 2007 (Fig. 2.40b). That increase continued in 2011, although the causes remain uncertain (Dlugokencky et al. 2009; Rigby et al. 2008). Bousquet et al. (2011) used observations from multiple independent measurement programs within a model framework to assess the changes in emissions and sinks responsible for renewed growth in atmospheric CH_4 . They found that changes in tropical wetland emissions were the dominant driver in 2007, with a minor contribution from Arctic wetlands. For 2008, two independent model approaches were not consistent. Neither a strong increase in emissions from wetlands in the tropics nor the Arctic was implied. They found that changes in the concentration of hydroxyl radical (OH), which would affect the CH_4 sink, were less than 1%, and they had only a small impact on observed CH_4 changes. During 2011 globally averaged atmospheric CH_4 at Earth's surface increased by $\sim 5 \pm 2$ ppb (ppb = nmol mol^{-1} , dry air) to an annual mean of 1803 ppb (preliminary values; Fig. 2.40b). The causes are likely related, in part, to increasing emissions from rapidly developing economies in Asia and to larger-than-average emissions from tropical wetlands (Dlugokencky et al. 2009; Bousquet et al. 2011; EDGAR 2009).

Carbon monoxide (CO) does not absorb strongly in the thermal infrared region, so it does not contribute directly to radiative forcing. However, it is a key species in atmospheric chemistry, particularly in cycling of reactive species like the OH and hydroperoxyl radical (HO_2). Changes in the atmospheric CO burden affect the lifetimes of other long-lived greenhouse gases, such as methane, hydrochlorofluorocarbons (HCFCs), and hydrofluorocarbons (HFCs), so it has an indirect effect on climate. No significant long-term trend has been detected in globally averaged CO determined from NOAA/ESRL measurements, which began in 1990 (Novelli et al. 2003), but CO anomalies occurred during 1997–98, and again in 2002–03 (Fig. 2.40c). These anomalies are likely the result of interannual variability in emissions from tropical and boreal biomass burning. Since the lifetime of CO is relatively short (few months), the CO enhancements quickly disappeared. The preliminary globally averaged CO mole fraction in 2011 is ~ 80.5 ppb, slightly less than in 2010.

(iii) *Nitrous oxide and sulfur hexafluoride*—B. Hall, J. W. Elkins, and G. Dutton

Atmospheric nitrous oxide (N_2O) and sulfur hexafluoride (SF_6) have significant manmade sources

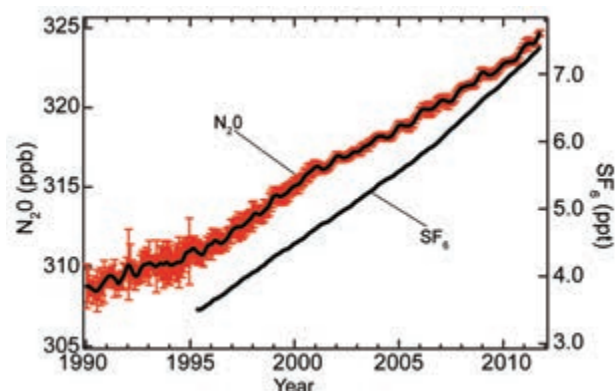


FIG. 2.41. Global average nitrous oxide (N_2O , ppb) and sulfur hexafluoride (SF_6 , ppt) mole fractions determined from NOAA discrete and in situ samples. Error bars for N_2O are based on monthly averages (1 std. dev.). Error bars for SF_6 are omitted for clarity, and are approx. 0.04 ppt in the 1990s and 0.02 ppt thereafter.

and are two of six gases selected for emission reduction under the Kyoto Protocol of the United Nations Framework Convention for Climate Change (UNFCCC). Atmospheric N_2O currently has the third strongest climate forcing of the long-lived greenhouse gases after carbon dioxide and methane. Current emissions of N_2O are expected to contribute more to future ozone depletion than current emissions of halogenated ozone-depleting substances (ODS) (Ravishankara et al. 2009). Nitrous oxide is produced naturally by both the oxidation of ammonium and the denitrification of nitrate. Significant emissions of N_2O can occur following the application of nitrogen fertilizers (including manure) on agricultural crops (Davidson 2009). Recent work suggests strong sources from tropical land areas with high temporal variability (Kort et al. 2011), although the cause of the variability has not been determined. The mean global atmospheric N_2O mixing ratio for 2011 was 324.3 ppb, an increase of 1.1 ppb over 2010 (Fig. 2.41). This year-on-year increase is higher than the average growth rate of 0.75 ± 0.01 ppb yr^{-1} observed from 1977 to 2010 (Elkins and Dutton 2011).

Sulfur hexafluoride (SF_6) is an important greenhouse gas because it has a large global warming potential (GWP; 23 900 times greater than CO_2 for a 100-year time horizon). This large 100-year GWP is primarily the result of its very long atmospheric lifetime of 3200 years (Solomon et al. 2007). Sulfur hexafluoride is primarily used as a dielectric insulator for transmission of electricity and emissions are entirely anthropogenic. Its global average mixing ratio in 2011 was 7.31 ppt (ppt = pmol mol^{-1} , dry air), an increase of 0.28 ppt over 2010 (Fig. 2.41). The average

linear growth rate was 0.22 ± 0.01 ppt yr⁻¹ from 1995 to 2007. Since 2007, the growth rate has averaged 0.28 ppt yr⁻¹.

(iii) Ozone-depleting gases and their replacements

—S. A. Montzka and G. Dutton

Long-lived halocarbons are important greenhouse gases and contribute significantly to present-day radiative forcing. Those halocarbons that contain bromine (Br) and chlorine (Cl) also influence radiative forcing indirectly through destruction of stratospheric ozone. Because of concern over stratospheric ozone depletion, production of many halocarbons has been restricted in recent years through amendments and adjustments to the 1987 Montreal Protocol on Substances that Deplete the Ozone Layer. As a result, mixing ratios of most of the potent ozone-depleting gases have been declining at Earth's surface; this decline continued in 2011 (Fig. 2.42).

While mixing ratios of many ODSs are declining, those of some halogenated gases continue to increase globally (Fig. 2.42c,d). The most rapid increases are observed for HCFCs and HFCs, which are common replacements for CFCs, halons, and other ODSs. HCFCs contain chlorine and deplete ozone with a reduced efficiency compared to CFCs. HFCs do not participate in ozone-destroying reactions.

Future levels of ozone-depleting halogen in the stratosphere (and, therefore, the threat to strato-

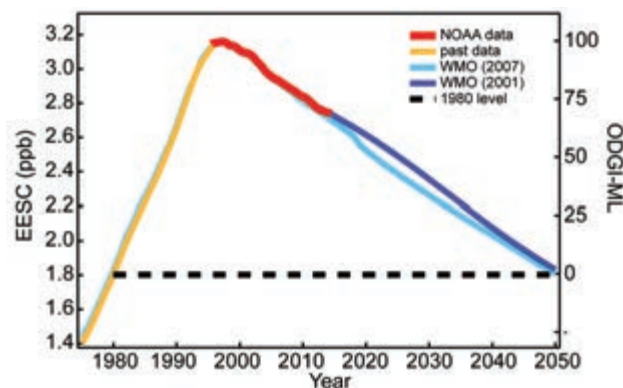


FIG. 2.43. Equivalent Effective Stratospheric Chlorine (EESC, left axis) and the Ozone Depleting Gas Index (ODGI) for midlatitudes (right axis) derived from NOAA/GMD data (red) and for various scenarios (blue) (Daniel et al. 2011). EESC is derived from EECl by adding three years to the time axis to represent the lag associated with mixing air from the troposphere to the middle stratosphere where the ozone layer resides.

spheric ozone) can be estimated from weighted sums of tropospheric halocarbon abundances. Since the efficiency for Br to destroy ozone is higher than that of Cl, Br atoms are assigned a higher weighting factor (a factor of 60 is used here, after Montzka et al. 2011). These sums are derived from surface-based measurements and are expressed as Equivalent Effective Chlorine (EECl; Fig. 2.42e).

The EECl content of the lower atmosphere declined fairly steadily through 2011 at a mean rate of 27 ppt yr⁻¹ since the peak in 1994 (Fig. 2.42e). Despite these substantial changes, full recovery of stratospheric ozone is not expected until the middle to latter part of the 21st century, owing to the long lifetimes of many of these chemicals (Table 2.4; Montzka et al. 2011). A similar conclusion can also be drawn from measurements of trace gases obtained by the AGAGE group (Prinn et al. 2000). Both NOAA and AGAGE measurements show similar trends in EECl in recent years (Montzka et al. 2011). Progress towards EECl declining back to the 1980 level can be readily assessed with the NOAA Ozone-Depleting Gas Index (ODGI) in Table 2.4 (Hofmann and Montzka 2009). This index (Fig. 2.43) is derived from EECl (Fig. 2.42e), scaled so that a value

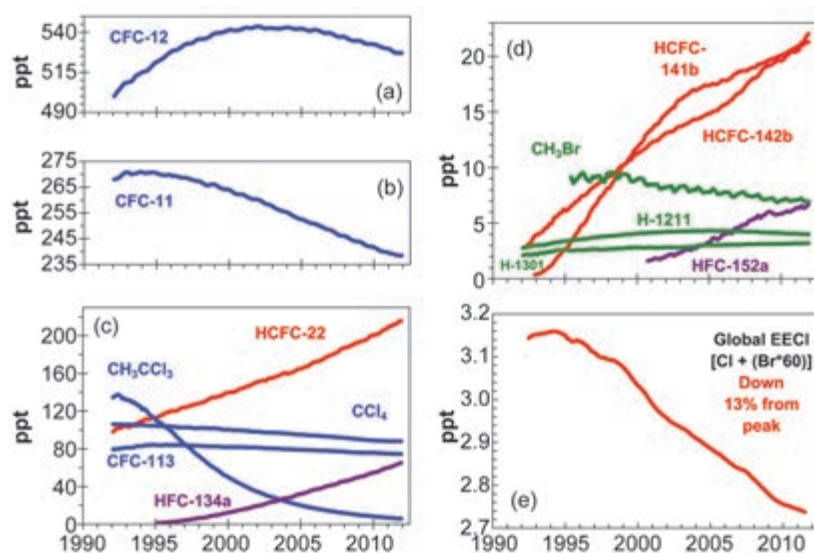


FIG. 2.42. (a)–(d) Atmospheric abundances (global mean tropospheric mixing ratios, dry air mole fraction) of the most abundant CFCs, HCFCs, HFCs, chlorinated solvents, and brominated gases, and (e) changes in atmospheric Equivalent Effective Chlorine (EECl) where EECl is derived as the sum of [Cl + (Br • 60)] from observed mixing ratios of ODS appearing in the other four panels.

TABLE 2.4. Mixing ratios, radiative efficiencies, and lifetimes of chemicals considered in the AGGI and ODGI (CO₂ mixing ratios in ppm, N₂O and CH₄ in ppb, all others in ppt).

Industrial Designation or Common Name	Chemical Formula	AGGI	ODGI	Radiative Efficiency (W m ⁻² ppb ⁻¹) ^a	Mean Surface Mixing Ratio 2011 [change from prior year] ^b	Lifetime (year) ^a
Carbon Dioxide	CO ₂	Y	N	1.41 × 10 ⁻⁵	390.4[1.9] ^c	
Methane	CH ₄	Y	N	3.7 × 10 ⁻⁴	1803.0[3.8] ^c	~9
Nitrous oxide	N ₂ O	Y	N	3.03 × 10 ⁻³	324.2[1.1]	114
Chlorofluorocarbons						
CFC-11	CCl ₃ F	Y	Y	0.25	238.5[-2.1]	45
CFC-12	CCl ₂ F ₂	Y	Y	0.32	527.4[-2.6]	100
CFC-113	CCl ₂ FCFClF ₂	Y	Y	0.30	74.7[-0.7]	85
Hydrochlorofluorocarbons						
HCFC-22	CHClF ₂	Y	Y	0.20	212.6[6.8]	11.9
HCFC-141b	CH ₃ CCl ₂ F	Y	Y	0.14	21.3[0.9]	9.2
HCFC-142b	CH ₃ CClF ₂	Y	Y	0.20	21.0[0.8]	17.2
Hydrofluorocarbons						
HFC-134a	CH ₂ FCF ₃	Y	N	0.16	62.6[5.4]	13.4
HFC-152a	CH ₃ CHF ₂	Y	N	0.09	6.5[0.4]	1.5
HFC-143a	CH ₃ CF ₃	Y	N	0.13	11.1[1.0]	47.1
HFC-125	CHF ₂ CF ₃	Y	N	0.23	9.7[1.4]	28.2
HFC-23	CHF ₃	Y	N	0.19	24.0[0.8]	222
Chlorocarbons						
Methyl Chloroform	CH ₃ CCl ₃	Y	Y	0.06	6.3[-1.3]	5.0
Carbon Tetrachloride	CCl ₄	Y	Y	0.13	87.1[-1.3]	26
Methyl Chloride	CH ₃ Cl	N	Y	0.01	538[-1.9]	1.0
Bromocarbons						
Methyl Bromide	CH ₃ Br	N	Y	0.01	7.05[-0.03]	0.8
Halon 1211	CBrClF ₂	Y	Y	0.30	4.0[-0.1]	16.0
Halon 1301	CBrF ₃	Y	Y	0.32	3.2[0.02]	65
Halon 2402	CBrF ₂ CBBrF ₂	Y	Y	0.33	0.45[-0.01]	20
Fully fluorinated species						
Sulfur Hexafluoride	SF ₆	Y	N	0.52	7.31[0.28]	3,200
PFC-14	CF ₄	N	N	0.10	79.0[0.7] ^c	> 50 000
PFC-116	C ₂ F ₆	N	N	0.26	4.2[0.11] ^c	> 10 000

^a Radiative efficiencies and lifetimes are taken from Daniel et al. (2011), Montzka et al. (2011), and Prinn et al. (2005). For CO₂, numerous removal processes complicate the derivation of a lifetime.

^b Mixing ratios are global surface means determined from the NOAA global cooperative sampling network (Hofmann et al. 2006), except for PFC-14 and PFC-116, and HFC-23 which were measured by the AGAGE group (Mühle et al. 2010; Miller et al. 2010).

^c Preliminary estimate for 2011.

of 100 represents the EECl [or Effective Equivalent Stratospheric Chlorine (EESC)] abundance at its peak, and 0 represents the 1980 level (a reference point during which ozone depletion was thought to have been small). In 2011, the ODGI-Mid-Latitudes

was 66.6. Less progress is evident for the index when the tropospheric data are weighted to be relevant for considering Antarctic changes; the ODGI-Antarctica was 82.4 in 2011.

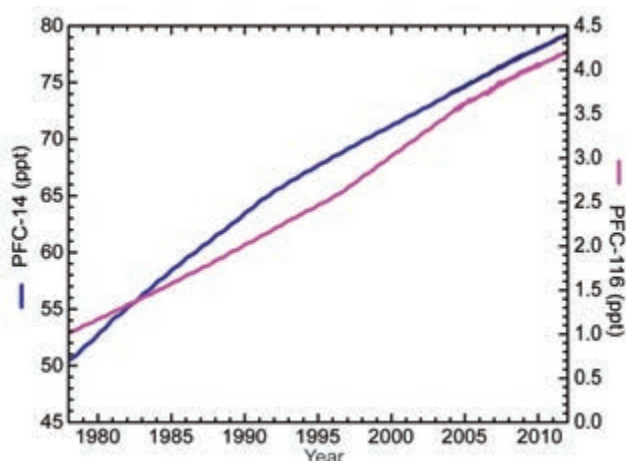


FIG. 2.44. Global average surface concentrations of PFC-14 (blue) and PFC-116 (magenta) (ppt) from the AGAGE network (Möhle et al. 2010).

(iv) Perfluorocarbons—J. Möhle

Perfluorocarbons (PFCs) are extremely long-lived, potent greenhouse gases. PFC-14 (CF_4) and PFC-116 (C_2F_6) have lower limits for atmospheric lifetimes of 50 000 and 10 000 years, respectively, and global warming potentials (100-year time horizon) of 7390 and 12 200, respectively (Montzka et al. 2011). Anthropogenic PFC-14 and PFC-116 were historically emitted as by-products of aluminum production (IAI 2011) and are also emitted from the electronics industry. However, the onset and extent of PFC emissions from the electronics industry is poorly known due to limited reporting (Worton et al. 2007; Möhle et al. 2010). A small natural source of CF_4 from degassing of Earth's crust has been identified (Harnisch and Eisenhauer 1998; Harnisch et al. 2000), which, because of its extraordinarily long atmospheric lifetime, accounts for its significant preindustrial abundance (Harnisch et al. 1996a,b) of 34.7 ± 0.2 ppt (Möhle et al. 2010), or $\sim 44\%$ of its 2011 abundance.

Based on preliminary data, global average surface mixing ratios of PFC-14 and PFC-116 were ~ 79 ppt and ~ 4.2 ppt in 2011, respectively (Fig. 2.44). Mixing ratios of PFC-14 rose at ~ 1.1 ppt yr^{-1} from the late 1970s to the early 1990s and by ~ 0.7 ppt yr^{-1} afterwards. Mixing ratios of PFC-116 rose at ~ 0.09 ppt yr^{-1} from the late 1970s to the mid-1990s, at ~ 0.12 ppt yr^{-1} until the mid-2000s, and at ~ 0.08 ppt yr^{-1} in recent years (Möhle et al. 2010 and preliminary data).

(v) The combined influence of long-lived trace gases on the radiative balance of the atmosphere—B. Hall and S. A. Montzka

Greenhouse gases affect the radiative balance of the atmosphere because they efficiently absorb

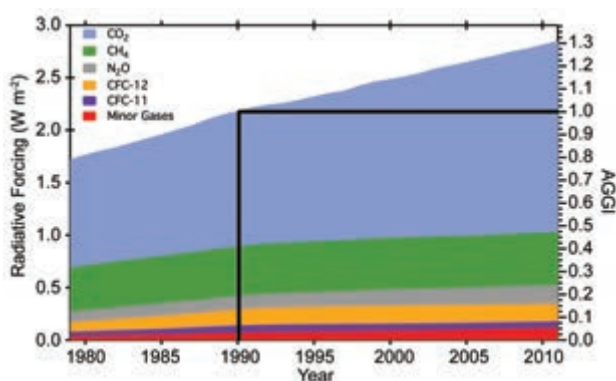


FIG. 2.45. Direct radiative forcing (W m^{-2}) due to long-lived trace gases (left axis), and the radiative forcing from long-lived trace gases, relative to 1990, defined as the Annual Greenhouse Gas Index (right axis). The value of the AGGI was 1.30 in 2011, an increase of 30% since 1990.

terrestrial infrared (IR) radiation. Recent trends in the radiative forcing (RF) of radiatively important gases are shown in Fig. 2.45. The NOAA Annual Greenhouse Gas Index (AGGI) was developed based upon the direct radiative influence from long-lived greenhouse gases, also known as radiative forcing, relative to the preindustrial era (1750; Hofmann et al. 2006). It represents the additional influence (over preindustrial values) due to long-lived trace gases in a given year relative to 1990, the Kyoto Protocol baseline year. Indirect effects (e.g., arising from ozone depletion or water-vapor feedbacks) are not considered in this index. The index is derived from global surface measurements of CO_2 , CH_4 , N_2O , CFC-12, and CFC-11 (the major long-lived greenhouse gases) and 15 minor greenhouse gases (e.g., HCFCs, HFCs; see Table 2.4).

Based on preliminary global mean data through 2011, the increases in the abundances of these gases over their preindustrial values amounted to an additional direct RF to the atmosphere totaling approximately 2.84 W m^{-2} . This compares with 2.18 W m^{-2} in 1990. Thus, the accumulation of long-lived trace gases in the atmosphere since 1990 has resulted in a 30% increase in RF due to long-lived gases.

2) AEROSOLS—A. Benedetti, J.-J. Morcrette, J. W. Kaiser, and L. T. Jones

Atmospheric aerosols have been recognized as a major source of uncertainty in future climate prediction (Forster et al. 2007; Denman et al. 2007). Most have a general cooling effect, reflecting incoming solar radiation back to space. However, black carbon has the potential to enhance warming through absorption of solar radiation (Ramanathan and

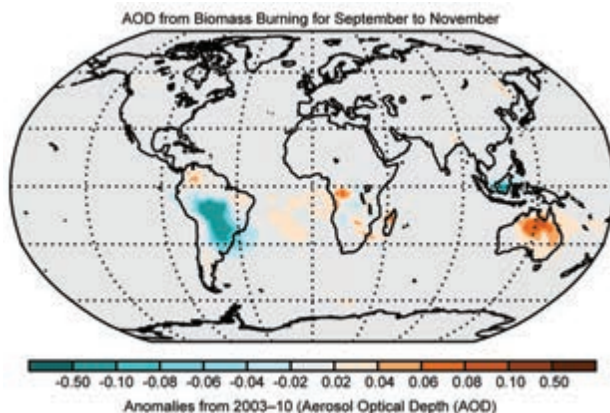


FIG. 2.46. MACC aerosol reanalysis aerosol optical depth anomaly in carbonaceous aerosols (dominated by biomass burning) for the 2011 Sep–Nov season.

Carmichael 2008). Quantifying the relative impact of the different aerosol types, including volcanic aerosols and those associated with biomass burning, along with aerosol-induced feedbacks in clouds and

precipitation, is crucial for understanding current climate (Lohmann and Feichter 2005).

Reanalyses have been heavily used by the scientific community since their introduction in the 1980s (Dee et al. 2011a). Atmospheric composition from reanalyses poses greater problems due to unknown biases in emissions, limited availability of constraining observations, shorter periods covered, and the complexity associated with accounting for all atmospheric constituents and modeling their interactions.

ECMWF has recently completed an eight-year reanalysis of atmospheric composition from 2003 to 2010, including aerosols, reactive gases, and greenhouse gases, under the EU-funded project Monitoring Atmospheric Composition and Climate (MACC; Simmons 2010). The aerosol analysis is based on assimilation of aerosol optical depth (AOD) observations (MODIS sensor) and the latest inventories and parameterizations for sea salt, desert dust, black carbon, organic matter, and sulfate aerosol. Preliminary assessments show that the MACC aerosol

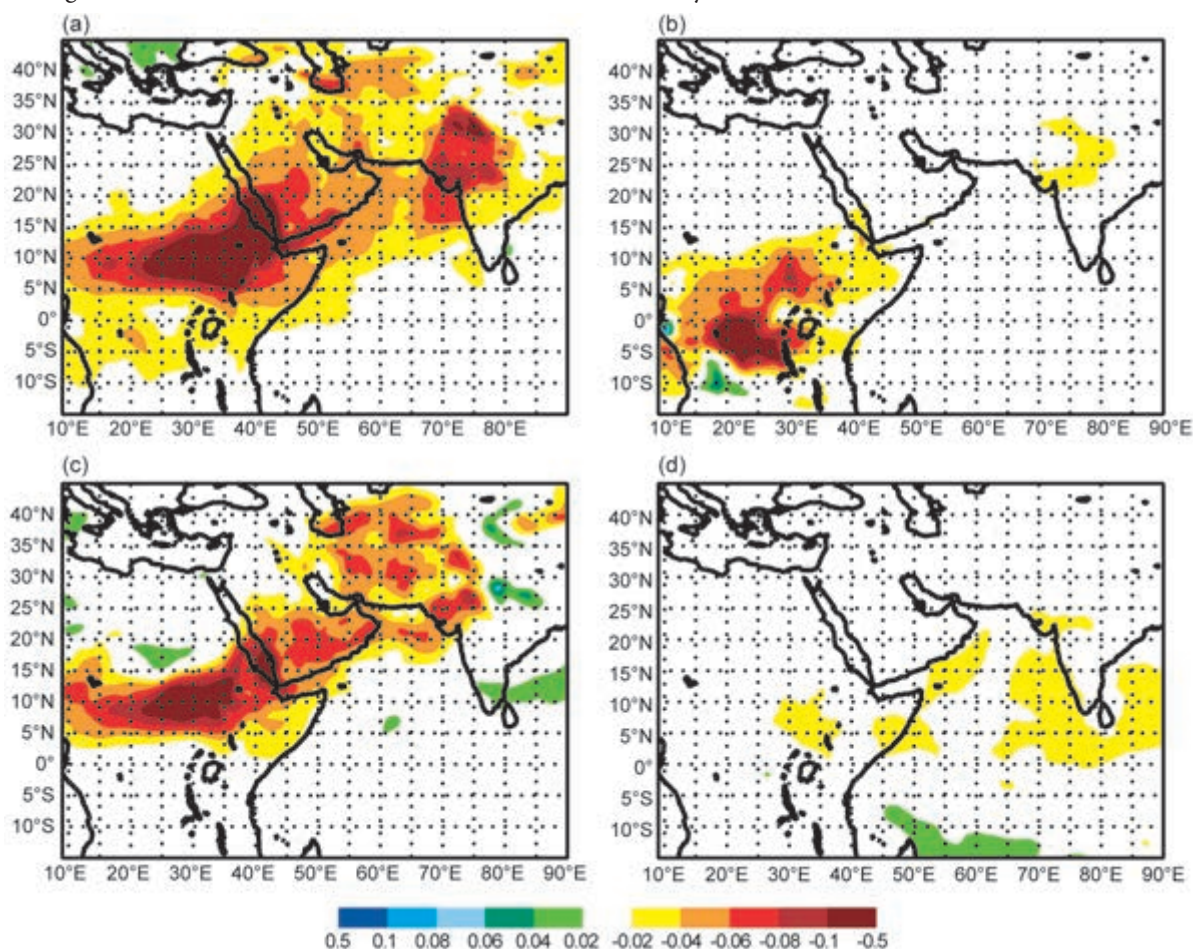


FIG. 2.47. Aerosol optical depth anomalies for the East Africa/Middle East/Indian Ocean area over Jun–Aug in 2011: (a) sulfate, (b) biomass burning, (c) desert dust, and (d) sea salt. The location of the Nabro volcano (13.36°N, 41.69°E) is marked with a star in (a).

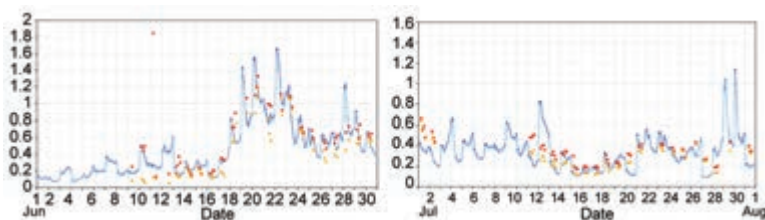


FIG. 2.48. Time series of aerosol optical depth (AOD) at the station of ICIPE_Mbita (0.42°S, 34.2°E) during June (left) and July (right) 2011. Red dots are the AERONET total AOD, yellow dots are the AERONET fine-mode AOD. The dark blue line represents the MACC reanalysis total AOD, while the light blue line represents the MACC reanalysis fine-mode AOD.

reanalysis tends to underestimate Saharan dust and overestimate sea salt. These are constant biases and do not necessarily affect estimates of anomalies. Anthropogenic aerosols, particularly biomass burning, appear to have realistic amplitude and distribution, and benefit from estimates of fire emissions from fire radiative power [Global Fire Assimilation System (GFAS); Kaiser et al. 2012; Plate 2.1t]. Recently, the MACC reanalysis was extended through 2011 to provide consistent data for this *State of Climate* report.

A map of time-averaged total AOD anomaly for 2011 is shown in Plate 2.1o, relative to a 2003–10 base period. This shows enhanced total AOD in parts of East Africa and the Middle East, mainly due to an anomalous amount of sulfate and dust, related to the eruption of the volcano Nabro (13.4°N, 41.7°E). A positive anomaly in AOD is also visible over Australia as a result of the intense fire activity during the months of September and October. The biomass burning activity over South America in 2011 appeared to be less intense than climatological expectations. This is shown clearly by September–November anomalies of carbonaceous aerosols, which are dominated by biomass burning (Fig. 2.46; section 2h4).

The boreal summer (JJA) of 2011 (Fig. 2.47) exhibited a large anomaly in AOD across the whole of north-equatorial Africa, especially west of the Horn of Africa. This was due to the volcano Nabro, situated in Eritrea, near the Ethiopian border, which erupted from 12 June through 7 July. The combination of volcanic emissions and seasonally dry conditions, i.e., lack of wet removal of soluble aerosol particles (Plate 2.1; Sidebar 7.2), helps to explain the lasting presence of aerosol particles. Large positive anomalies in AOD are evident over the entire Middle East and the Indian Ocean, the latter consistent with an increase in sea salt (Fig. 2.47d).

The MACC reanalysis is constrained by observations of total AOD, hence the redistribution into different species is entirely dependent on the model. At

present, the MACC model does not represent volcanic aerosol sources explicitly. Instead, the observed AOD signal from volcanic ash is attributed to other species. In the region shown in Fig. 2.47, the volcanic ash signal has been attributed mainly to dust and sulfate. Independent data from the AERONET station close to Lake Victoria (Fig. 2.48) show high values of fine-mode AOD starting in the second half of June and persisting through July, which is indicative of the presence of fine aerosols being advected southward from the volcanic source.

3) STRATOSPHERIC OZONE—M. Weber, W. Steinbrecht, C. Long, V. E. Fioletov, S. H. Frith, R. Stolarski, and P. A. Newman

The 2011 annual mean total ozone was above the 1980–2008 mean in the tropics and below at higher latitudes and, in particular, both polar regions (Plate 2.1p). This pattern is related to the westerly phase of the quasi-biennial oscillation (QBO), as discussed in section 2b3.

Figure 2.49 shows time series of total ozone in polar regions (60°–90°) from different ground and

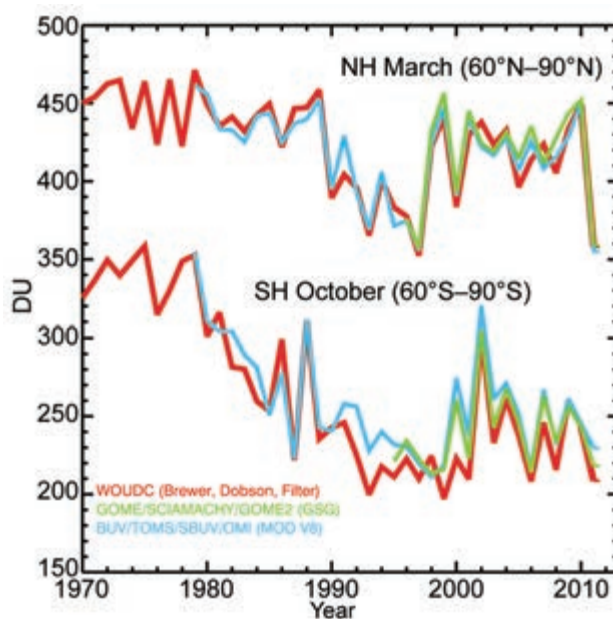


FIG. 2.49. March and October polar total ozone (in Dobson Units, DU) in the Northern and Southern Hemisphere, respectively. WouDC ground-based measurements combining Brewer, Dobson, and filter spectrometer data (red: Fioletov et al. 2002, 2008), the merged BUV/SBUV/TOMS/OMI MOD V8 (blue: Stolarski and Frith 2006), and GOME/SCIAMACHY/GOME-2 “GSG” (green: Weber et al. 2007).

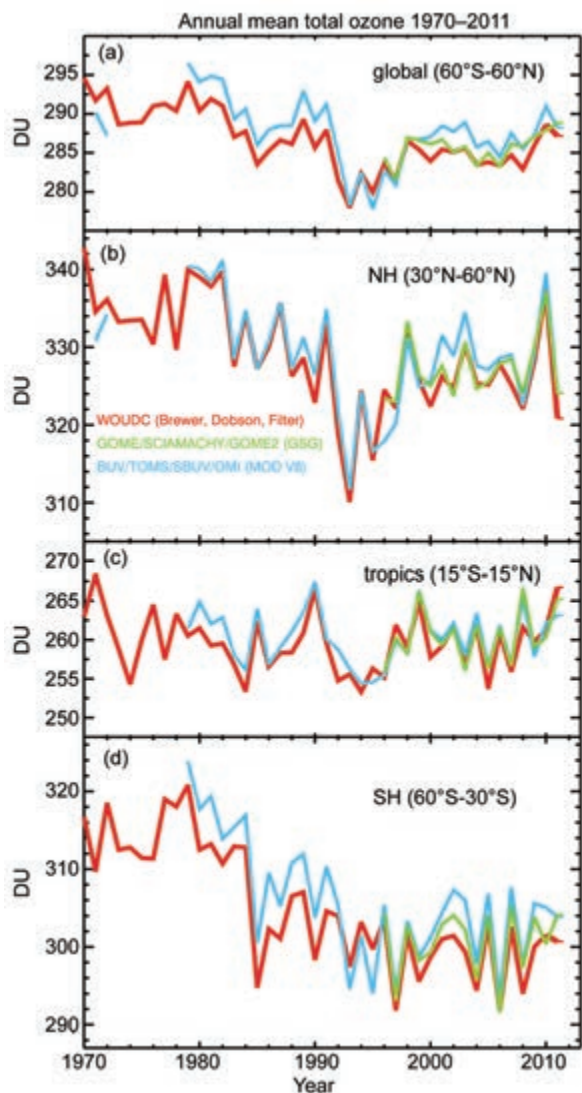


FIG. 2.50. Annual mean total ozone (DU) time series of ground-based measurements as described in Fig. 2.49 for the (a) 60°S–60°N (globe), (b) 30°N–60°N (Northern Hemisphere), (c) 15°S–15°N (tropics), and (d) 30°S–60°S (Southern Hemisphere) zonal bands.

satellite data in March (Arctic) and October (Antarctica). The March Arctic mean was extremely low and comparable to the lowest values of the 1990s, owing to low temperatures (section 2b3). These low temperatures allowed polar stratospheric clouds to form, leading to record-high chemical ozone losses. These were close to typical Antarctic ozone hole conditions (see section 6g; Manney et al. 2011; Sinnhuber et al. 2011). The Antarctic ozone hole in austral spring was among the largest on record (see section 6g). The seasonal persistence of extratropical ozone anomalies from winter/spring into the summer months (Fioletov and Shepherd 2003; Weber et al. 2011) resulted in marked negative anomalies in the annual mean (Plate 2.1p).

Long-term trends in total ozone (Figs. 2.49, 2.50) are statistically significant only in the extratropics. The midlatitude losses between 1980 and the early 1990s were followed by stable but variable values in the Southern Hemisphere and a significant increase and subsequent leveling off in the 2000s in the Northern Hemisphere. The substantial minimum in the Northern Hemisphere in the early 1990s arose from additional ozone loss associated with the Mount Pinatubo volcanic eruption and a series of unusually cold Arctic stratospheric winters (e.g., Dhomse et al. 2006). Despite the low extratropical ozone observed in 2011, there is evidence that ozone has started recovering as ozone depleting substances are phased out in accordance with the Montreal Protocol and amendments (see section 2g1iii; Mäder et al. 2010; Salby et al. 2011; Weber et al. 2011).

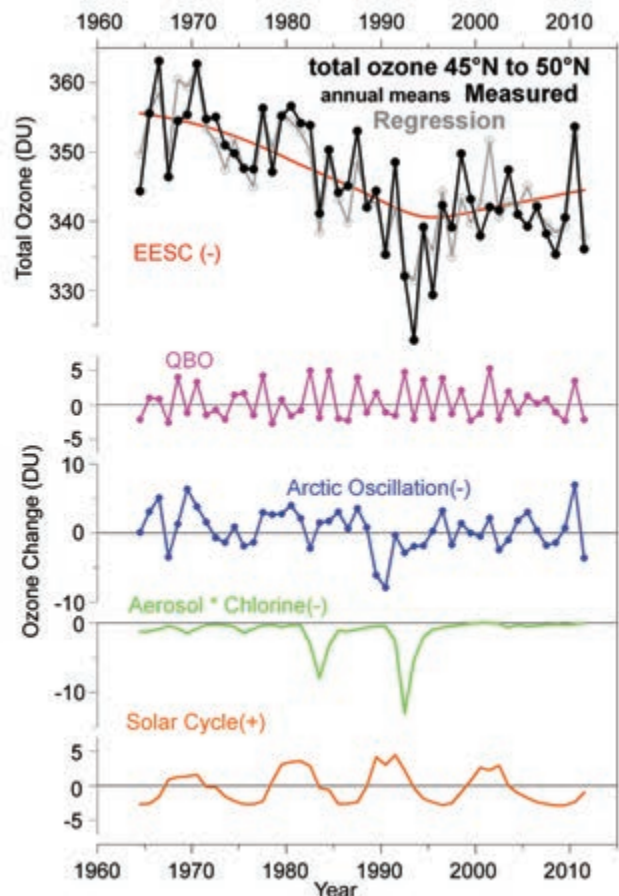


FIG. 2.51. Observed total ozone and magnitude of contributing factors obtained by multiple linear regression. Annual and zonal mean total ozone (DU) at 45°N–50°N from WUODC ground-based data (black) and multiple linear regression results (gray) partitioned into ozone variation attributed to EESC (red), QBO (magenta), AO (blue), enhanced stratospheric aerosol multiplied by EESC (green), and the 11-year solar cycle (orange).

Figure 2.51 shows a multivariate linear regression with different explanatory variables considered to be major factors in ozone changes (Steinbrecht et al. 2011) applied to the 45°N–50°N zonal annual mean total ozone from the World Ozone and Ultraviolet Radiation Data Centre (WOUDC) ground data (Fioletov et al. 2002, 2008). Major factors include the QBO, AO (Arctic Oscillation), solar activity, major volcanic eruptions, and changes in stratospheric halogen or EESC (Equivalent Effective Stratospheric Chlorine; Newman et al. 2007). The large downward swing in ozone from 2010 to 2011 follows the large changes in AO (-12 DU) and QBO (-5 DU). The anthropogenic ozone recovery as expressed by the EESC curve is a modest increase of 3 DU since 1997.

Following an upper stratospheric decline of 10% to 15% from the early 1980s to the mid-1990s, mainly attributed to the anthropogenic release of ozone depleting substances (ODS), upper stratospheric ozone has leveled off. In the last 10 years, the various records even show signs of an increase (Steinbrecht et al. 2009; Jones et al. 2009; WMO 2011).

Ozone trends in the tropical lowermost stratosphere are mainly driven by tropical upwelling (SPARC 2010; Lamarque and Solomon 2010). Randel and Thompson (2011) observed a negative trend of

-2% to -4% decade⁻¹ in the 17-km – 21-km altitude range from a combination of satellite (SAGE I+II) and ozonesondes. This indicates a long-term increase in the tropical upwelling and associated strengthening of the meridional circulation.

4) STRATOSPHERIC WATER VAPOR—D. Hurst and K. Rosenlof

Stratospheric water vapor continued to increase during 2011 over most of the globe, but the anomalies varied significantly with latitude and altitude. Based on data from the Aura Microwave Limb Sounder (MLS), lower stratospheric tropical anomalies at 82 hPa were strongly positive during January, and high southern latitude anomalies were strongly negative during July (Fig. 2.52). Negative anomalies that encircled Antarctica during July were likely associated with polar vortex dehydration. In the tropics, the coldest temperatures that determine stratospheric entry values of water vapor occur near 82 hPa. Entry values are normally lowest in January and highest in July, so the positive tropical anomalies in January imply that 2011 annual minimum cold point temperatures were warmer than the 2005–10 January average. Lower stratospheric water vapor anomalies

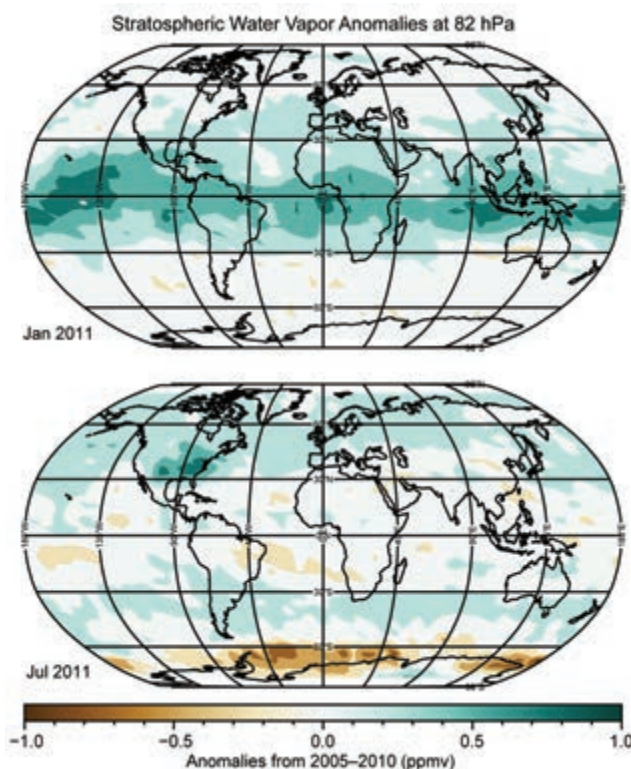


FIG. 2.52. Global stratospheric water vapor anomalies (ppmv) at 82 hPa for January (upper) and July (lower) 2011 from the Aura Microwave Limb Sounder (MLS).

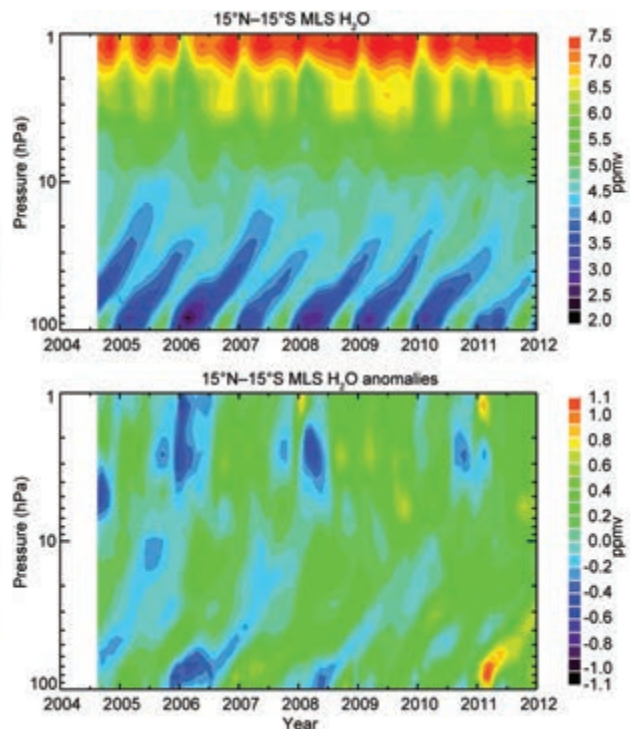


FIG. 2.53. Time series of MLS vertical profiles of monthly water vapor mixing ratios (upper) and anomalies (lower; 2005–10 base period) in the tropics (15°N–15°S). The prominent and reoccurring lower stratospheric QBO signals observed from 2004–08 are not apparent during 2009–11 (lower figure).

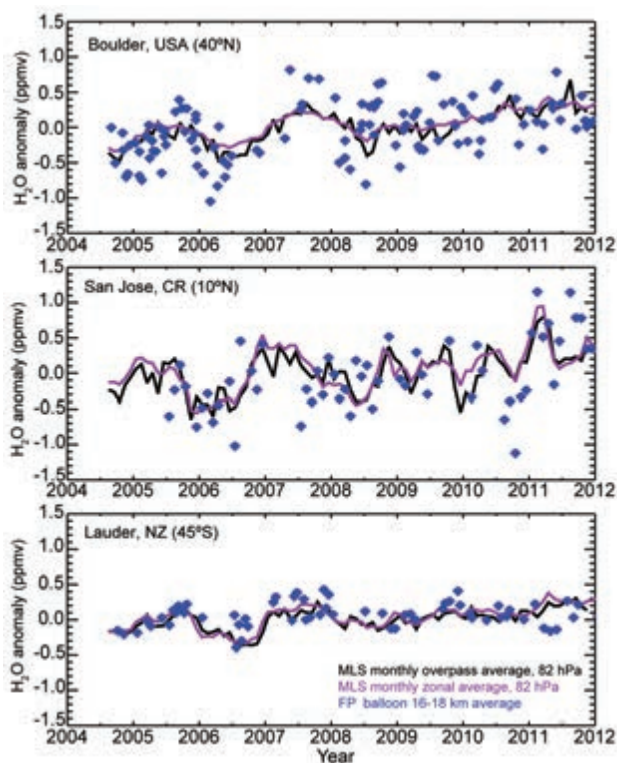


FIG. 2.54. Lower stratospheric water vapor anomalies (ppmv; differences from 2005–10 monthly averages) from three frost point sonde locations: Boulder, Colorado, USA; San Jose, Costa Rica; and Lauder, New Zealand. Blue symbols depict mean anomalies between 16 km and 18 km for individual soundings with balloon-borne frost point hygrometers; black lines are monthly mean anomalies at 82 hPa from MLS retrievals within $\pm 2^\circ$ latitude and $\pm 15^\circ$ longitude of the sonde sites; purple lines are MLS zonal monthly mean anomalies at 82 hPa within the $\pm 2^\circ$ latitude band surrounding each sonde site.

during January were strongest over the central Pacific region. The underlying dynamical mechanisms (see below) are unclear.

Time series of water vapor vertical profiles and their anomalies from August 2004 through 2011 also show the strong positive anomaly in the tropical lower stratosphere during January–February 2011 (Fig. 2.53). Unlike the previous dry anomalies that originated in the lower tropical stratosphere and propagated to the upper stratosphere, the strong January 2011 wet anomaly was almost completely eroded before reaching the middle stratosphere. The weak vertical propagation of this strong anomaly suggests a slowing of the tropical upwelling.

Time series of lower stratospheric water vapor anomalies at three locations where routine frost point hygrometer soundings are made (Fig. 2.54) depict increasing trends since late 2004. These are from MLS

and balloon-borne frost point hygrometer measurements. The current water vapor increase started after a rapid drop of ~ 0.5 ppmv (10%) in 2000–01 and several subsequent years of low mixing ratios. Over the longer term, the frost point hygrometer record over Boulder, Colorado (40°N), depicts a net increase of 1.0 ± 0.2 ppmv ($27 \pm 6\%$) from 1980 to 2010 (Hurst et al. 2011). Only about 30% of this long-term growth is attributable to increased stratospheric water vapor production associated with increasing atmospheric methane (section 2g1i). Complete global satellite-based water vapor records are too short to corroborate or refute the magnitude of the 30-year Boulder trend. High spatial and temporal coverage began with operational MLS in August 2004. Before then, satellite-borne solar occultation instruments did not offer complete global measurement coverage, while balloon-borne frost point hygrometers provided data with sparse spatial and temporal density.

The MLS record reveals strong tropical water vapor signals related to the QBO from 2004 through 2008 (Figs. 2.53, 2.54; Zhou et al. 2001). The QBO influence results in a quasi-two-year cycle of low and high water vapor values originating at ~ 100 hPa and propagating upward with time. Damped QBO signals are also apparent at higher latitudes prior to 2009 (e.g., Lauder and Boulder). Since 2009, these QBO signals are no longer evident in the tropical and midlatitude water vapor records.

In summary, the increasing trend in stratospheric water vapor since ~ 2006 continued through 2011. Large positive anomalies in tropical entry values (82 hPa) during January–February 2011 point to abnormally warm tropical cold point temperatures. Anomalies in tropical entry values related to the QBO during 2004–08 have not been observed since 2009. The exact mechanisms behind the 2011 stratospheric water vapor anomalies are currently unknown and require additional study.

h. Land surface properties

1) FOREST BIOMASS AND BIOMASS CHANGE—S. Quegan, P. Ciais, and A. Baccini

The focus of recent forest biomass estimates has been on: (1) reducing the large uncertainties in the tropical land use change flux and the associated tropical sink due to regrowth of secondary forest; (2) quantification of the tropical sink in intact forest; and (3) identification of the location, cause, and strength of the land carbon sink at temperate and boreal latitudes consistently seen in atmospheric inversion studies (e.g., <http://transcom.lsce.ipsl.fr>). A major motiva-

SIDEBAR 2.3: LONG-TERM CHANGES OF ATMOSPHERIC SOLAR TRANSMISSION—E. DUTTON

Both the solar and thermal infrared transmission of the atmosphere play important roles in Earth's energy balance. For example, the anticipated long-term worldwide decrease in infrared atmospheric transmission, due to increasing greenhouse gas abundance, gives rise to the issues and concerns of global warming. Similarly, long-term increases in the solar transmission would contribute to warming, while a decrease would have the opposite effect. While considerable attention and effort has gone into observations necessary to track and understand the long-term global background of the atmospheric infrared transmission, relatively few similar records of the solar transmission exist.

One of the longest, continuous observational records of solar transmission through the free troposphere and above is maintained by NOAA at the Mauna Loa observatory in Hawaii (Dutton and Bodhaine 2001). This consists of qualified daily and monthly averages of clear-sky morning “apparent” solar transmission obtained from pyrheliometer observations by the methodology first described by Ellis and Pueschel (1971). The “apparent” is an optical term applied to the solar transmission values used here because they are determined from ratios of direct beam solar irradiances observed at different solar zenith angles (atmospheric paths) such that the computed transmission is relative to the irradiance already transmitted along the shorter path. The irradiance is measured with a calibrated pyrheliometer. The linear calibration factor cancels out in the apparent transmission ratio, yielding a more accurate and stable result.

This measure of solar transmission is particularly sensitive to aerosols. The computational procedure diminishes the effect of water vapor, which is the other major contributor to variable clear-sky solar transmission, due to saturation effects. There is also a minor ozone contribution, although this is not significant on the scale of the variations seen. Spectral aerosol optical depth is also observed (sun photometer) at the site and confirms the primary aerosol role in current observed solar transmission variability. Although only a single site, Mauna Loa can be considered representative of a much larger portion of the Earth because of its remote central Pacific location and high elevation, above most local effects, especially in the early morning during downslope-wind conditions when daily transmission measurements are made.

The complete apparent transmission (AT) record (Fig. SB2.7a) shows the extended impact of three major explosive volcanic eruptions (Agung, 1964; El Chichón, 1982; and Pinatubo, 1991). These injected large quantities of sulfur dioxide (SO_2) into the stratosphere, where it was converted to sulfate aerosol and remained for many months while spreading around the world. A certain amount of month-to-month variability and a small amplitude (~ 0.007 AT) annual cycle (spring minimum, winter maximum) persisting throughout much of the record are also seen. This annual cycle has been attributed to the seasonally enhanced transport of Asian tropospheric aerosol over the

site (Bodhaine et al. 1981). Not so apparent in the record are potential variations in the overall background transmission, which have the most enduring effects. Examination of the last decade (Fig. SB2.7b) and other information by Solomon et al. (2011) has shown a small net downward tendency, possibly due to multiple periods of injection of stratospheric aerosols. Figure S2.7b suggests a general decrease of about 0.003 AT occurring between 1998 and 2010. This trend is also seen in collocated spectral aerosol optical depth measurements. However, the downturn appears to have ended in the last 2–3 years. Currently, it is not possible to discern a continuing coherent long-term behavior in the record, but the 55-year AT record permits putting the current variability into historical context.

Using these and other data, Solomon et al. (2011) computed that the decline in transmission (or equivalently, an increase in AOD) from the late 1990s to 2010 was sufficient to reduce tropospheric warming by about 0.07°C compared to a scenario with a relatively “clean” stratosphere, as was previously widely used in global climate models for that decade. The source of the general decrease in solar transmission is suspected to be several small, largely unnoticed, volcanic eruptions that together have increased the stratospheric component of the total column aerosol over a large portion of the globe (Vernier et al. 2011).

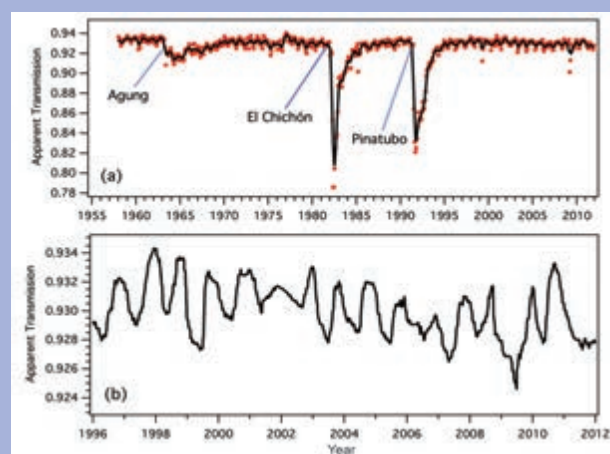


FIG. SB2.7. Mauna Loa, Hawaii, apparent transmission in (a) monthly means (points), with 5-month running smoother (line) and (b) 100-point running means (converging to 49 points at the end of 2011) of available clear-sky morning daily averages from the NOAA MLO observatory at 3.4 km ASL using a tracking solar pyrheliometer converted following Ellis and Pueschel (1971). Major explosive volcanoes are indicated. Smoothing in (b) gives anomalous periods with fewer observed days less weight than in the presentation of monthly averages (a).

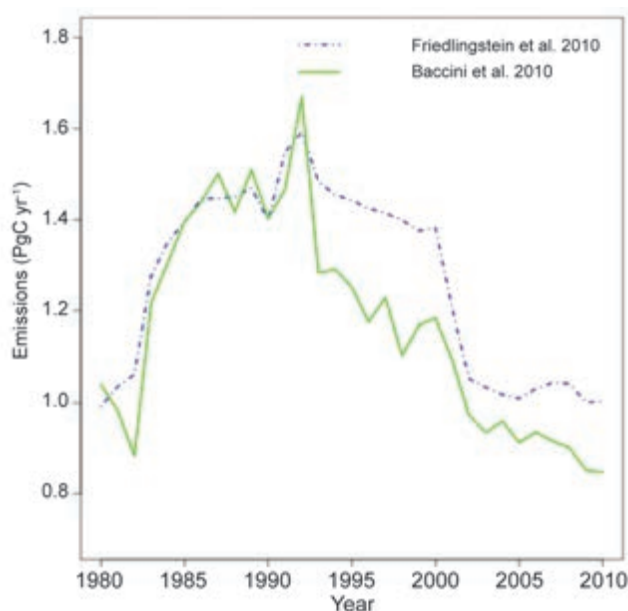


FIG. 2.55. Annual net emissions (Pg C yr^{-1}) from land-use change in the tropics calculated by Friedlingstein et al. (2010) and Baccini et al. (2012).

tion for improved information on biomass has also been the UNFCCC Decision 1.1 (2010 Conference of the Parties, Cancun; <http://www.unfccc.int/resource/docs/2010/cop16/eng/07a01.pdf>) which encourages developing country Parties to contribute to mitigation actions in the forest sector.

Although the periodic reports of the Food and Agricultural Organization (FAO 2006, 2010) remain a key source for information on biomass, they are based on national forest inventories/statistics and suffer from lack of systematic inventory data in many forest biomes, particularly in developing countries, leading to data gaps, sampling biases, inconsistency of methods, lack of spatial information, and unrepresentative samples (Grainger 2008). The search for more consistent global approaches, particularly for the tropics, has prompted use of satellite data calibrated against

in situ biomass, with special emphasis on using the archive of forest height estimates derived from the Geoscience Laser Altimeter System onboard the Ice, Cloud and land Elevation Satellite (ICESat) before its failure in 2009 (Lefsky 2010). This approach has given rise to two recent pan-tropical biomass maps (Saatchi et al. 2011; Baccini et al. 2012) at grid scales of 1 km and 0.5 km, respectively. The continental scale aggregates of above-ground biomass from the two maps are 94.6 Pg C, 50.2 Pg C, and 48.3 Pg C (Saatchi et al. 2011) and 117.7 Pg C, 46.5 Pg C, and 64.5 Pg C (Baccini et al. 2012) for South America, Asia, and Africa, respectively. Baccini et al. (2012) exploit these new biomass estimates to recalculate the tropical land use change flux as $0.96 \text{ Pg C yr}^{-1}$ for the period 2000–10, which is 11–12% lower than the recent global assessment of Friedlingstein et al. (2010; Fig. 2.55); both studies use the same rates of deforestation, taken from FAO (2010).

In contrast, Pan et al. (2011) took a bottom-up approach to estimating forest sinks and sources, based on estimates from inventory data and field observations coupled to statistical models. This builds on national inventory datasets, enhanced by data from research networks [e.g., the tropical RAINFOR project (Malhi et al. 2002)] and new tropical deforestation and tropical forest regrowth estimates, and includes all carbon pools, not just biomass. The world's forests were estimated to yield a net global sink of $1.2 \pm 0.9 \text{ Pg C yr}^{-1}$ over the period 2000–07, made up of a net sink of $2.3 \pm 0.5 \text{ Pg C yr}^{-1}$ in established forests, regrowth in tropical forests of $1.7 \pm 0.5 \text{ Pg C yr}^{-1}$, and tropical deforestation “gross” emissions of $2.8 \pm 0.5 \text{ Pg C yr}^{-1}$. Around 73% of the global sink comes from increased biomass, and of this, 80% occurs in the tropics, both from biomass increment in intact forest and regrowth (Table 2.5). Deforestation and Amazon drought caused the biomass increment in tropical intact forest to decrease by 25% in the last decade compared to the 1990s.

As well as these global estimates, there have been important developments at the regional scale. Ma et al. (2012) and Peng et al. (2011) used long-term permanent forest sampling plots to show that recent climate change, especially reduced precipitation, has caused a decline of around 7.3 million tons of carbon per year in the biomass carbon sink in western Canada; this is equal to approximately 4% of Canada's total annual carbon emissions. Bellassen et al. (2011) demonstrated that good estimates of the forest carbon sink in the intensively managed

TABLE 2.5. Biomass increments for 1990–99 and 2000–07 by latitude zone; the global values are also shown (values taken from Pan et al. 2011).

Biomass increment (Tg C yr^{-1})	1990–99	2000–07
Boreal	117	120
Temperate	345	454
Tropical intact	1167	870
Tropical regrowth	1361	1497
All tropics	2529	2367
Global	2991	2941

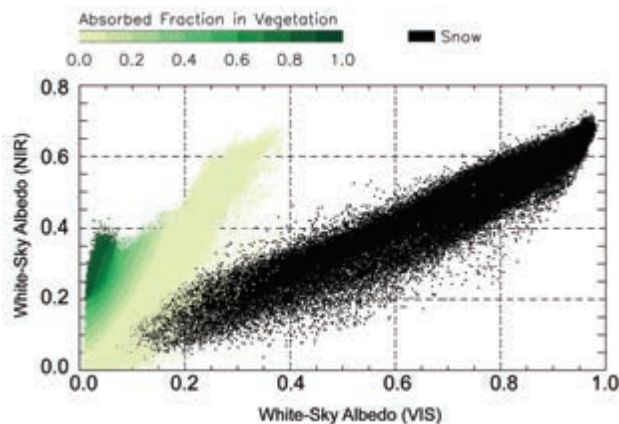


FIG. 2.56. MODIS broadband visible and near-infrared white-sky surface albedo (NASA) collection 5 (after re-sampling). Snow-covered pixels (according to the MODIS snow flag) are identified in black. Snow-free pixels are associated with an estimate of the Fraction of Absorbed Photosynthetically Active Radiation (derived from the JRC-TIP) represented by the green color scale.

European forests can be derived by using a process model (ORCHIDEE) to combine the reconstructed forest age structure (a proxy for biomass stocks) with the effects of carbon dioxide (CO_2) increase and climate. They found that the aging of forest stands accounts for most of the inventory-observed forest sink across European countries. However, the sink trend is explained predominantly by CO_2 fertilization and by the effects of climate trends (87%), with a smaller contribution (13%) from trends in forest age structure. In the United States, Williams et al. (2012) also used a process model (CASA) driven by satellite observation of disturbance history at very high spatial resolution (Landsat time series data) to separate the effect of forest age structure (disturbance recovery) from those of climate and CO_2 . They found carbon sinks to be mainly explained by age structure in the South Central, Pacific Northwest, and Pacific Southwest regions. In other regions, the effect of age was smaller. At country scale, the age structure contribution to forest NEP (the sink before harvest and disturbance) was modeled to be $0.16 \text{ Pg C yr}^{-1}$, which is smaller than former estimates based on inventory data ($0.27 \text{ Pg C yr}^{-1}$ to $0.41 \text{ Pg C yr}^{-1}$). The difference was attributed either to the effects of CO_2 and climate, or to undersampling of disturbed areas by the forest inventory sampling scheme, due to the smaller scale of disturbance compared to the mesh of the US inventory.

2) LAND SURFACE ALBEDO—B. Pinty

The land surface albedo, i.e., the fraction of solar radiation scattered backward by land surfaces, results from complex nonlinear radiation transfer processes determining the amount of radiation that is scattered by the vegetation and its background, transmitted through the vegetation layer, or absorbed by the vegetation layer and its background.

Figure 2.56 illustrates the range of variations of surface albedo quantities observed for a full year over the globe in the two-dimensional visible (VIS) and near-infrared (NIR) broadband spectral domains. These data result from a resampling of the MODIS white-sky albedo (equivalent to a bihemispherical reflectance under perfect isotropic illumination, i.e., independent from ambient atmospheric conditions) product collection 5 at 0.01° spatial resolution (Schaaf et al. 2002). Partial or full snow cover conditions are associated with a large dynamical range of albedo values particularly in the visible domain. By contrast, the spectral signature of snow-free conditions is restricted to a much smaller domain (Fig. 2.56 bottom left). In the latter instances, the variability in albedo is largely controlled by the amount of vegetation covering the background featured by the Fraction of Absorbed Photosynthetically Active Radiation derived from the JRC-Two-stream Inversion Package (TIP; Pinty et al. 2011a,b). Note that very small changes in visible surface albedo can be associated with significant variations in vegetation dynamics.

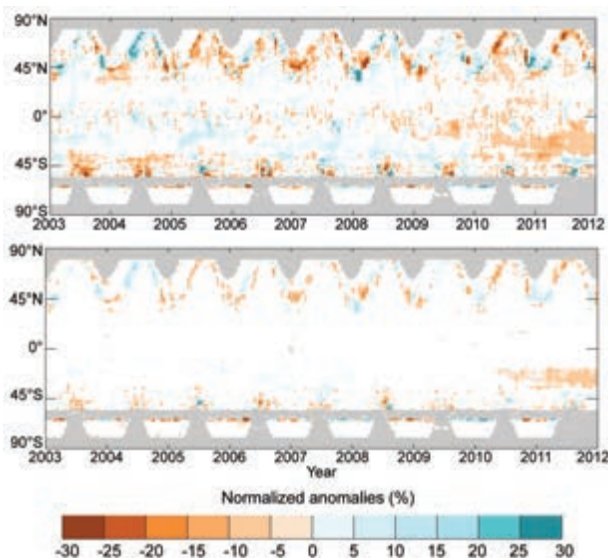


FIG. 2.57. Zonal means of the MODIS white-sky broadband surface albedo (NASA) normalized anomalies in the (a) visible and (b) near-infrared domain relative to a 2003–11 base period.

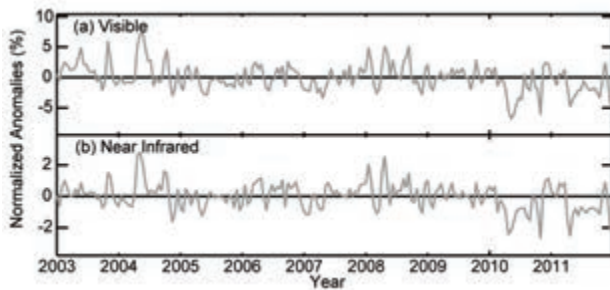


FIG. 2.58. Globally averaged MODIS White Sky broadband surface albedo (NASA) normalized anomalies in the (a) visible and (b) near-infrared domain relative to a 2003–11 base period.

The geographical distribution of normalized anomalies in visible and near-infrared surface albedo for 2011 relative to a 2003–11 base period (for which two MODIS sensors are available) are shown in Plates 2.1q and r, respectively. Mid- and high-latitude regions of the Northern Hemisphere are characterized mainly as a consequence of interannual variations in snow cover amount and duration in winter and spring seasons (section 2c2). The amplitude of these changes can reach $\pm 30\%$ in relative units, and are slightly larger in the visible than in the near-infrared domain. Snow-free regions experienced dramatic variations with noticeable positive anomalies over the southwestern United States as a consequence of the exceptionally persistent summer heat and drought (see section 7b2 for more details). The situation in Australia and southern Africa contrasts notably with strong negative anomalies in both spectral domains. These changes are associated with more favorable vegetation growing conditions by comparison to previous years (see sections 2d3, 2h3). More subtle variations in albedo occur in a number of other regions, in particular over Central and South America, as well as the intertropical zone of Africa (especially the eastern part), India, and China. These variations are attributed to vegetation dynamics over these regions sensitive to stress from ambient conditions, such as water availability and temperature.

Analysis of the zonally-averaged albedo anomalies in the visible (Fig. 2.57a) and near-infrared (Fig. 2.57b) spectral domain indicates considerable interannual variations related to the occurrence of snow events in winter and spring at mid- and high-latitudes but also in vegetation conditions during the summer periods. Persistent negative

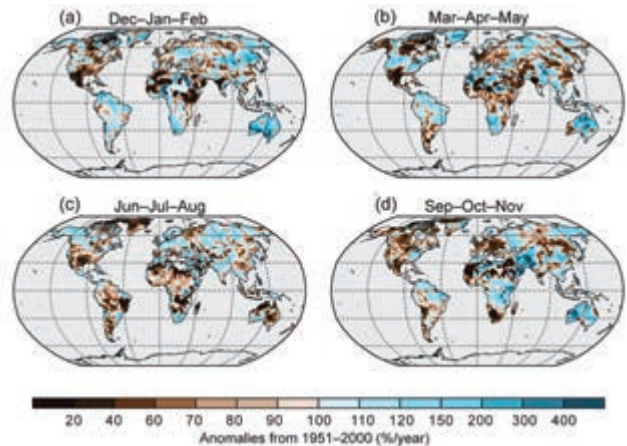


FIG. 2.59. SeaWiFS and MERIS 2011 seasonal anomalies (1998–2011 base period) for FAPAR. Positive anomalies indicate favorable vegetation growing conditions (blue) while negative values are markers of vegetation under stress (orange).

anomalies are noticeable for 2010 and 2011 between 20°S and 40°S.

The amplitude of the globally averaged normalized anomalies (Fig. 2.58) are within $\pm 7\%$ (3%) in the visible (near-infrared) domain. Limited positive anomalies dominate the start and end of 2011 while the remaining seasons exhibit well-marked negative anomalies. Figure 2.58 also suggests the presence of spectrally correlated multi-annual variations during 2003–11, with positively biased values at the beginning of the record.

3) TERRESTRIAL VEGETATION DYNAMICS - FRACTION OF ABSORBED PHOTOSYNTHETICALLY ACTIVE RADIATION—N. Gobron

Significant spatiotemporal variations in vegetation dynamics occurred on regional and continental scales during 2011. The state of vegetation is examined using estimates of the Fraction of Absorbed Photosyntheti-

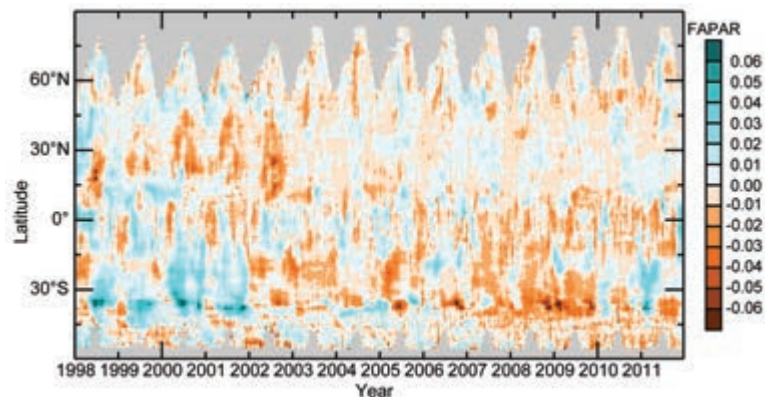


FIG. 2.60. SeaWiFS and MERIS 10-day anomalies (1998–2011 base period) of FAPAR by latitude. Gray areas indicate regions where data are unavailable.

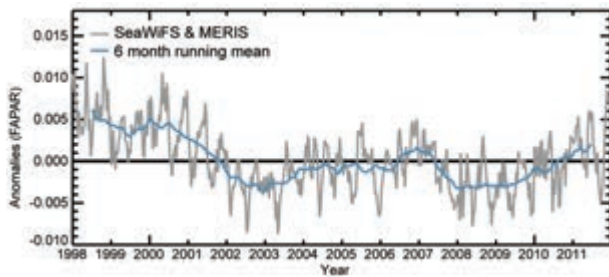


FIG. 2.61. Global average ten-day anomalies with a 6-month running mean (1998–2011 base period) for FAPAR.

cally Active Radiation (FAPAR) from 1998 to 2011 (Gobron et. al. 2010). Global anomalies highlight geographical regions subject to changes in 2011 with respect to previous years (Plate 2.1s).

The largest positive (favorable for vegetation) annual anomalies are observed over Australia and southern Africa, northeastern Brazil, central United States, Asia, and central Europe. The strongest negative anomalies occurred over the southern United States and northern Russia, eastern Africa, and Amazonia to a lesser extent. Over central Russia, the extreme negative FAPAR anomalies that occurred in 2010 have recovered towards a more normal state. Australia and southern Africa had plentiful precipitation and soil moisture in 2011 (sections 2d3, 2d7, 7e4).

The southern United States, in particular Texas, suffered precipitation deficit in spring and a summer heat record, which translated into strong negative seasonal (Fig. 2.59c) and annual anomalies. Amazonia did not fully recover from the droughts of 2010, as the signature of this event is still noticeable. The drought that occurred over the eastern regions of Africa is well depicted, especially at the seasonal level during the first half of the year.

Zonally averaged anomalies (Fig. 2.60) illustrate hemispheric differences, with persistent negative anomalies occurring over the Southern Hemisphere during all seasons from approximately 2002 to 2009. In contrast, since 2010, rather strong positive anomalies are observed over regions located between 20°S–40°S. This figure highlights strong summer negative anomalies above 20°S and below 40°S for 2011.

When globally averaged, FAPAR anomalies (Fig. 2.61) indicate that 2011 marked the return of vegetation to a positive state following a more than three-year period of negative departures.

4) BIOMASS BURNING—J. W. KAISER AND G. R. VAN DER WERF

The burning of vegetation releases large amounts of trace gases and aerosols to the atmosphere. While fires occur naturally, humans have modified background fire regimes both by lighting more fires and by modification of land and land cover types. In addition, fire fighting and prescribed burning present a departure from background fire conditions.

Fire emissions for contemporary times are calculated either by multiplying burned area, biomass, and the fraction of biomass that is actually consumed in a fire (Seiler and Crutzen 1980), or by using measurements of emitted energy from fires (Wooster et al. 2005). Both approaches rely heavily on satellite data, and the calculated dry matter consumed is subsequently multiplied by emission factors derived from field measurements to estimate trace gas and aerosol emissions (Andreae and Merlet 2001). The MACC Global Fire Assimilation System (GFAS; Kaiser et al. 2012) developed in the Monitoring Atmospheric Composition and Climate (MACC) project for the European Union's (EU) GMES (Global Monitoring

TABLE 2.6. Annual continental-scale biomass burning budgets in terms of carbon emission (Tg C yr^{-1}) reported in GFASv1.0. Definition of regions as in Kaiser et al. 2011, 2012.

Time Period	2003–10		2011	2011 w.r.t. 2003–10	
Quantity	Mean	Range	Value	Absolute Anomaly	Relative Anomaly
Global	2043	1774–2312	1987	-57	-3%
N America	99	71–138	111	+11	+12%
C America	65	53–91	72	+7	+11%
SH America	357	177–456	199	-159	-44%
Europe and Mediterranean	37	30–62	26	-11	-30%
NH Africa	413	331–458	409	-5	-1%
SH Africa	521	488–591	564	+42	+8%
N Asia	202	105–470	159	-43	-21%
SE Asia	135	111–162	95	-40	-29%
Tropical Asia	93	22–218	80	-12	-13%
Australia	120	52–176	273	+153	+127%

for Environment and Security) atmospheric services merges both approaches and is capable of estimating emissions in near-real time.

Over 2003–10, GFASv1.0 estimates carbon emissions of approximately 2.0 Pg C yr^{-1} . This is in close agreement with estimates from the Global Fire Emissions Database (GFED3; Giglio et al. 2010; van der Werf et al. 2010), which has a longer record starting in 1997, but cannot be updated as frequently as GFAS. The 1997–2002 years not included in GFASv1.0 did not deviate much from the 2003–10 period, with the notable exception of 1997–98. At that time, record-high emissions from Indonesia, in combination with higher-than-average emissions from the boreal region and Central America, yielded emissions that were, on a global scale, over 30% above average.

The global fire emissions of 2.0 Pg C in 2011 were close to the 2003–10 climatological mean (Table 2.6). On a regional scale, Australia experienced an exceptionally active fire season; its emission was 127% higher than the 2003–10 average and 47% higher than the largest value reported (for 2001) in the longer time series of GFED3. Plate 2.1t shows that the fires

in 2011 burned mostly in the interior of Australia, while in other years most fires were detected farther north (Fig. 2.62).

In most regions, fire activity increases during fire seasons with drought conditions. This happened in 2011 in Texas and northern Mexico, where hot and dry anomalies are exhibited (Plate 2.1). The larger land surface albedo and lower FAPAR (Plates 2.1q–s) are manifestations of associated vegetation mortality.

In arid regions such as the interior of Australia, however, fire activity is, in large part, a function of available biomass, which depends on rainfall during the wet season preceding the fire season. In Australia, there was enough rainfall (Plate 2.1i) for the grasses in this arid region to form a continuous fuel bed (Plates 2.1q–s), which subsequently burned in austral spring of 2011. The smoke from these fires were recorded as a strong positive smoke aerosol anomaly (Fig. 2.46). A similar mechanism appears to lie behind the increased fire activity in southern Africa.

Fire activity in South America was the second lowest since 2003, in line with decreasing deforestation rates reported by the Brazilian Space Agency (INPE 2012). Fires are used in the deforestation process to remove biomass and usually the amount of deforestation and fire activity are related, although 2007 and 2010 saw elevated emissions, possibly related to fires in cerrados (savanna) and degraded forests (Kaiser et al. 2011). The low fire activity is also reflected in a negative aerosol anomaly over South America (Plate 2.1o; Fig. 2.46). In most other regions including the boreal and deforestation regions, fire activity in 2011 was within the 2003–10 range.

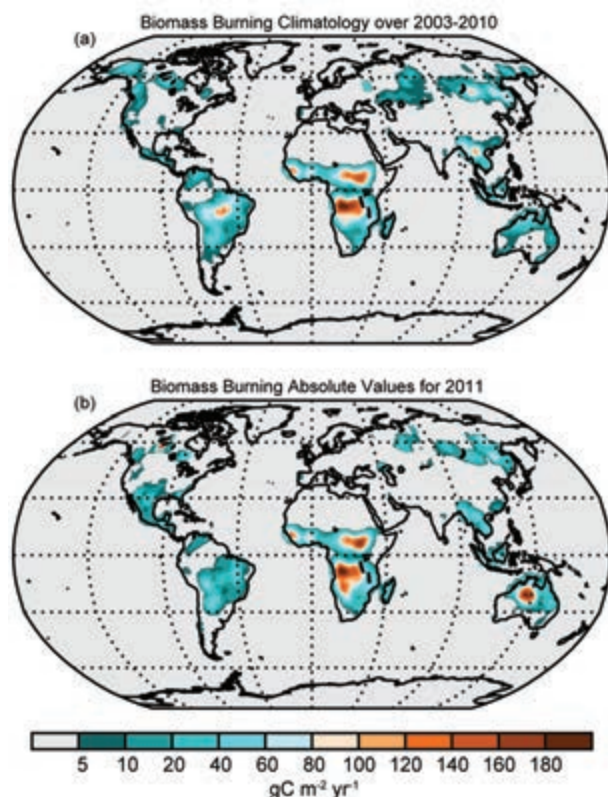


FIG. 2.62. Biomass burning in terms of annual carbon emission per unit area at 0.5° resolution: (a) climatology, and (b) values for 2011. Derived from MODIS observations processed in the MACC GFAS (Kaiser et al. 2012).

Libraries: Please file with the *Bulletin of the American Meteorological Society*, Vol. 93, Issue 7

